LANCASTER UNIVERSITY

The Great Space Weather Washing Machine: Examining the Dynamics of High-Latitude Ionosphere-Thermosphere Coupling

by

Daniel D. Billett

This thesis is submitted in partial fulfilment of the requirements
for the degree of Doctor of Philosophy

in the
Faculty of Science and Technology
Department of Physics

1st October 2019

Declaration of Authorship

I, Daniel D. Billett, declare that this thesis titled 'The Great Space Weather Washing Machine:
Examining the Dynamics of High-Latitude Ionosphere-Thermosphere Coupling' and the work presented in it are my own. I confirm that:

- This work was done wholly or mainly while in candidature for a research degree at this University.
- Where any part of this thesis has previously been submitted for a degree or any other qualification at this University or any other institution, this has been clearly stated.
- Where I have consulted the published work of others, this is always clearly attributed.
- Where I have quoted from the work of others, the source is always given. With the exception of such quotations, this thesis is entirely my own work.
- I have acknowledged all main sources of help.
- Where the thesis is based on work done by myself jointly with others, I have made clear exactly what was done by others and what I have contributed myself.

Signed:

Date:

Abstract

The Earth's upper atmosphere at high latitudes is a complicated region that is under the influence of many competing forces. For one, it is where the atmosphere becomes partially ionised, and thus subjected to the electromagnetic influences of the coupled solar wind-magnetosphere system. In contrast, neutral particles strongly feel the effects of non-magnetic forces, such as those due to temperature gradients and the Coriolis effect. Once ion-neutral collisions are then taken into account, the result is a global scale "washing machine" of charged and neutral particles, moving through various different spin cycles of coupling strength.

Firstly, it is the inherent differences between neutral and plasma flows that result in one of the largest atmospheric sinks of magnetospheric energy: Joule heating. It has sometimes been assumed in previous studies that the neutral wind is slow enough to be treated as if it was stationary. However, we show in Chapter 3 that this is not the case statistically using plasma velocity data from the Super Dual Auroral Radar Network (SuperDARN) and an empirical neutral wind model (HWM14). Overall, the inclusion of neutral winds can lead to global Joule heating estimates that differ by as much as 18% from calculations assuming they are stationary. We also present common scenarios by which the neutral wind can provide both a net increase or decrease to heating rates, depending on season and geomagnetic activity level.

In Chapter 4, neutral wind velocity measurements from an all-sky Fabry-Perot Interferometer known as SCANDI are presented for a period where the plasma velocity varied greatly in magnitude. We show that over the relatively small region observed (about 1000 km in diameter) for the event in question, the time it took for the neutrals to be fully accelerated or decelerated by a change in the plasma varied by as much as 30 minutes. Compared to the average neutral wind response time of around 75 minutes, this is quite a large amount of variability for regions at mesoscale separations. This has implications for how closely coupled the ionosphere and thermosphere are on a global scale, and shows the importance of carefully taking into account the current states of both.

Finally, an aurorally active period that occurred towards the end of the event presented in Chapter 4 is examined more closely in Chapter 5. We saw that coinciding

with the onset of poleward moving auroral forms, the neutrals rapidly accelerated in the direction of the plasma - much faster than prior to the aurora. We propose that due to the increased ionisation from particle precipitation, combined with the rapid transient plasma bursts in the poleward direction, the strength of ion-neutral coupling was enhanced significantly. This also happened during a transition of the IMF B_y component, showing for the first time a pseudo coupling of the thermosphere directly to the solar wind.

Acknowledgements

There are loads of people I want to thank for their help, patience and friendship over the years I've been at Lancaster. The SPP office, for not hanging underwear on the radiator and helping to cultivate the local chilli garden. My brothers, for their mispronunciations of actually quite easy words. Mum and dad, for their constant backing, encouragement and miles driven along the M5 and M6.

Thank you to Professor Jim Wild and Dr Adrian Grocott, who have both given me many hours of their time and helped me gain what I think is a decent understanding of ionospheric physics. Most importantly though, an understanding of how to be a scientist - from writing papers that actually make sense, all the way to putting half a space before the unit in a LaTeX file.

Even though it was late on, thank you to professor Hosokawa. I was really made to feel welcome at your lab at UEC Tokyo, academically, as well as alcoholically. I learned a lot whilst I was in Japan, and won't forget the experience I had.

Thank you to the members of the SuperDARN and UK MIST communities. I've been very lucky to be a part of both, as they are filled with some of the smartest, funniest and friendliest people I know. As far as I'm concerned, with my extremely limited knowledge of the communities in other fields, I can safely say that ours is the best.

Thank you to the doctors, nurses, surgeons and other NHS staff at the Royal Lancaster Infirmary who took care of me during my surgery recovery and helped me overcome a really tough part of my life. Because of you all, I will hopefully have this PhD thing in the bag.

Finally, I want to thank Dr Carley Martin for being here every step of the way. By lifting me up and supporting me when I needed it the most, being the reason I found Lancaster, and also believing in me enough to move literally across the world. I can say with 100% certainty, that I wouldn't be where I am without you.

Contents

List of Figures

List of Tables

Abbreviations

AACGM - Altitude-Adjusted Corrected Geomagnetic

ACF - Autocorrelation Function AE-C - Atmospherics Explorer C

AU - Astronomical Unit

DE1/2 - Dynamics Explorer 1 and 2

DMSP - Defense Meteorological Satellite Program

EISCAT - European Incoherent Scatter Scientific Association

EMCCD - Electron Multiplying Charged Coupling Device ESR - EISCAT Svalbard Radar

EUV - Extreme Ultra-Violet Radiation

FPI - Fabry-Perot Interferometer

FWHM - Full-width-half-maximum

GCM - General Circulation Model

GSM - Geocentric Solar Magnetospheric

GUVI - Global Ultraviolet Imager

HF - High Frequency

IRI - International Reference Ionosphere

VHF - Very High Frequency

UHF - Ultra High Frequency

HMB - Heppner-Maynard Boundary

HWM - Horizontal Wind Model

IDM - Ion Drift Meter

IGRF - International Geomagnetic Reference Field

IRI - International Reference Ionosphere

IMF - Interplanetary Magnetic Field

KHO - Kjell Henriksen Observatory

LOS - Line-of-sight MLAT - Magnetic Latitude

MLT - Magnetic Local Time

PMAF - Poleward Moving Auroral Forms

RPA - Retarding Potential Analyser

RST- Radar Software Toolkit

SuperDARN - Super Dual Auroral Radar Network

SCANDI - Scanning Doppler Imager, located on Svalbard

SDI - Scanning Doppler Imager

SRP - Spectral Resolving Power

TIEGCM - Thermosphere-Ionosphere-Electrodynamics General Circulation Model

UT - Universal Time

WATS - Wind and Temperature Spectrometer

Chapter 1

Introduction

In this chapter, we will discuss the dynamic systems of Earth's upper polar atmosphere. This region contains many processes, each highly coupled to others via different mechanisms. We will begin by discussing the fundamental physics that dictates the motion of plasma in a magnetic field, followed by the interaction of the magnetosphere with the solar wind, which links the atmosphere directly to the Sun. We will also describe the high latitude (>50° geomagnetic latitude) neutral thermosphere, its behaviour and complex interaction with the ionosphere. Finally, this chapter will discuss the resultant energy that is transferred from the solar wind into the atmosphere due to ionosphere-thermosphere friction, known as Joule heating, which forms the basis of the research presented in this thesis.

1.1 Plasma and Neutral Particle Dynamics

Plasmas, such as the solar wind, are a collection of electrically charged particles. Unlike neutral fluids, plasmas experience the effect of electromagnetic forces. In the upper atmosphere of Earth where ionisation of the thermosphere takes place, a low density plasma is formed (known as the ionosphere) which is coupled to the terrestrial magnetic field. Fluid theory of the ionosphere-thermosphere system involves treating each particle species (electrons, ions and neutrals) separately as a collection of particles on the macroscale that experience collisions. However, due to the low plasma density over most of the altitude range of the ionosphere (discussed later on in section 1.3.1), we may treat microscale plasma motion as if they are single particles that do not directly interact with one another. This section will therefore be split into two parts; one describing single particle motion of the plasma, the other describing the collisional dynamics of plasma and neutral collections.

1.1.1 Single Particle Motion of Plasmas

A particle of charge q at rest generates an electric field ($\mathbf{E}$), which represents the Coulomb force ($\mathbf{F_c}$) another charged particle would feel when near it:

$$\mathbf{F_C} = q\mathbf{E} \tag{1.1}$$

This is the force that causes like charges to repel and opposite to attract. When there is differential motion of opposite charges, a current is formed, even though charger carriers still feel the Coulomb force due to others. In the reference frame of a non-moving observer, those charges will technically be length contracted according to the principles of special relativity, meaning when $\mathbf{F_C}$ is calculated for a particle moving with a velocity $\mathbf{v}$, we will get an underestimation of the total force it actually experiences. The extra force to account for this discrepancy is known as the Lorentz force ($\mathbf{F_L}$), which is due to a new vector field referred to as the magnetic field ($\mathbf{B}$):

$$\mathbf{F_L} = q\left(\mathbf{v} \times \mathbf{B}\right) \tag{1.2}$$

$\mathbf{v} \times \mathbf{B}$ in this context is actually just an additional electric field in the reference frame of the moving particle. So, the total force on a charged particle in motion is:

$$\mathbf{F} = q\left(\mathbf{E} + \mathbf{v} \times \mathbf{B}\right) \tag{1.3}$$

Electric and magnetic fields are strongly linked together through several relations known as Maxwell's equations. First, Gauss's law states that the amount of electric flux passing through a surface due to any given charge is given by q/ϵ_0, which is also equal to the electric field integral over the enclosed area. In differential form, the Maxwell-Gauss law for electricity is:

$$\nabla \cdot \mathbf{E} = \frac{\rho}{\epsilon_0} \tag{1.4}$$

where ρ is the charge density and ϵ_0 is the permittivity of free space. Accounting for the magnetic field, the Maxwell-Gauss law for magnetism states that the net magnetic flux through a surface is zero due to various observations and mathematical proofs that a magnetic monopole cannot exist, so:

$$\nabla \cdot \mathbf{B} = 0 \tag{1.5}$$

The Maxwell-Faraday equation shows that a change in magnetic flux induces an electric field (and in turn, a current) in a closed conductor:

$$\nabla \times \mathbf{E} = -\frac{d\mathbf{B}}{dt} \tag{1.6}$$

Symmetrically, a spatially varying electric field produces a magnetic field; Maxwell-Ampere's law shows this relationship as the magnetic field induced through a closed loop being proportional to displacement of a current I, $\oint \mathbf{B} = \mu_0 I$, or in its differential form:

$$\nabla \times \mathbf{B} = \mu_0 \left(\mathbf{j} + \epsilon_0 \frac{d\mathbf{E}}{dt} \right) \tag{1.7}$$

where $\mathbf{j}$ is the current density.

In the absence of an electric field and a constant magnetic field, a charged particle will move in the direction of $\mathbf{B}$ (defined here as directed in the z direction) at a constant drift velocity, $v_d = v_z$. The Lorentz force in this direction ($m\frac{dv_z}{dt}$) is zero, but along the x and y direction we get (from Eq. 1.2):

$$m\frac{dv_x}{dt} = qBv_y, \quad m\frac{dv_y}{dt} = -qBv_x \tag{1.8}$$

where m is the mass of the particle. These equations define circular motion of a charged particle perpendicular to a magnetic field, or "gyromotion". The frequency of gyration,

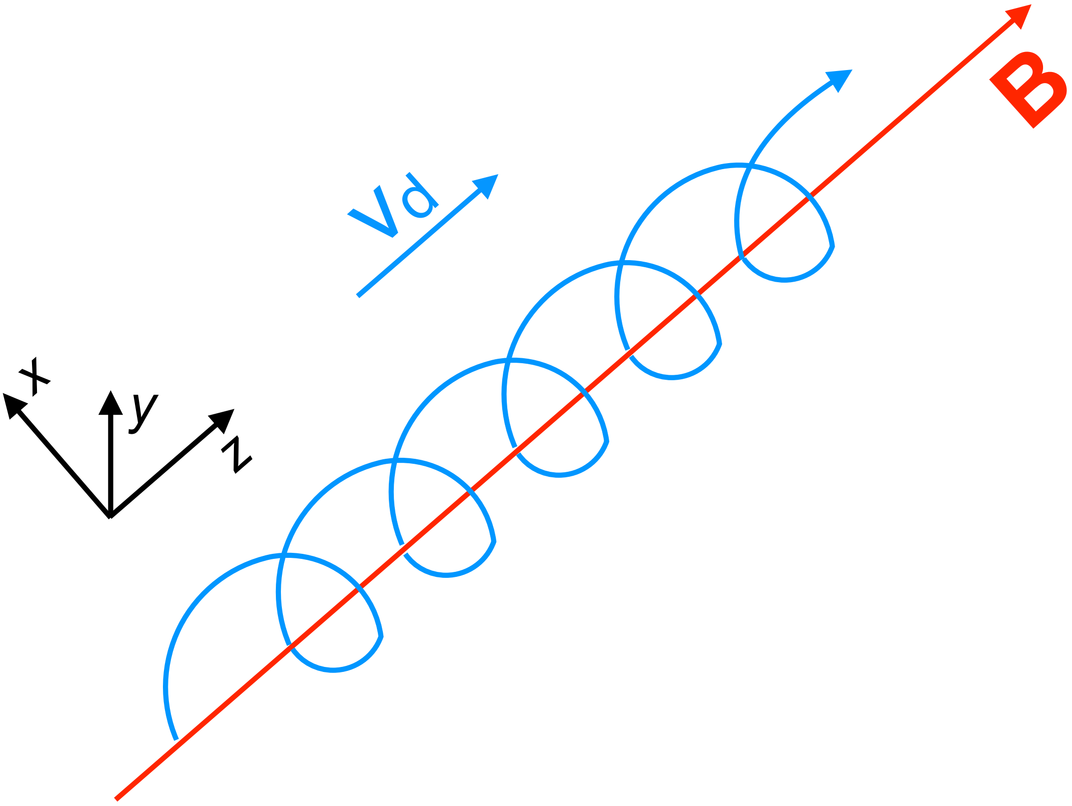

FIGURE 1.1: Schematic representation of charged particle gyrating around a magnetic field in a helicoidal trajectory. v_d is the drift velocity, i.e. the velocity in the z direction.

ω_g, is given by:

$$\omega_g = \frac{qB}{m} \tag{1.9}$$

and by equating the magnitude of the Lorentz force to the circular centripetal force, the gyroradius is:

$$r_g = \frac{mv_\perp}{|q|B} \tag{1.10}$$

where $v_\perp = \sqrt{v_x^2 + v_y^2}$. Figure 1.1 shows the trajectory of a positive ion undergoing gyromotion in the presence of a magnetic field, which appears helical when the parallel velocity is non-zero. An electron, due to its negative charge and smaller mass, would gyrate in the opposite direction, at a longer frequency and smaller gyroradius according to Eqs. 1.9 and 1.10.

As we have seen with Maxwell's equations however, electric and magnetic fields are intrinsically linked and rarely constant, especially within the Earth's magnetosphere.

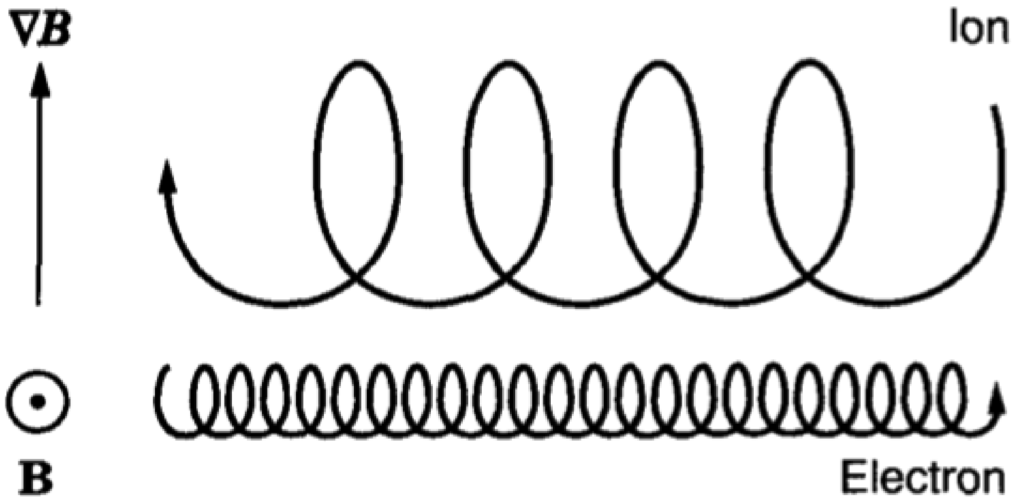

Figure 1.2: Diagram of the magnetic gradient drift motion for ions and electrons. The magnetic field is directed out of the page, with an increasing field strength upwards. Taken from Baumjohann and Treumann (2012).

Thus, we will now describe how the drift described here varies as the magnetic field changes in strength, and when an electric field is introduced.

1.1.1.1 Magnetic Gradient Drift

First, let us assume the magnetic field strength is weakly increasing in the direction perpendicular to the field itself. Eq. 1.10 states that the gyroradius will decrease with increasing B, but as the particle passes the periapsis of its orbit, it is now traveling in the direction of decreasing B, which will enlarge its orbit. This periodic variation in gyroradius, averaged over several gyrations, results in the particle drifting perpendicular to both the field and its gradient. The velocity of the magnetic gradient drift, $\mathbf{v}_\nabla$, is given by:

$$\mathbf{v}_\nabla = \frac{mv_\perp^2}{2qB^3}(\mathbf{B} \times \nabla B) \tag{1.11}$$

which tells us that ions and electrons will drift in opposite directions, and that $\mathbf{v}_\nabla$ is dependent on the particles perpendicular kinetic energy $\left(\frac{1}{2}mv_\perp^2\right)$. A diagram of the magnetic gradient drift of both ions and electrons is shown in Figure 1.2.

It should be noted that the differential drift motions of the ions and electrons, driven by the ∇B drift, induces a current known as the gradient drift current:

$$\mathbf{j}_{\nabla} = qn_e(\mathbf{v}_{\nabla\mathbf{i}} - \mathbf{v}_{\nabla\mathbf{e}}) \tag{1.12}$$

where n_e is the electron density and q is the elementary charge. This occurs equatorially in the Earth's inner magnetosphere where there is a positive magnetic field gradient radially outward, and is known as the ring current.

1.1.1.2 $\mathbf{E} \times \mathbf{B}$ Drift

The Lorentz force is always perpendicular to the drift velocity of a charged particle. Therefore, a magnetic field (with $\nabla B = 0$) alone cannot cause a charged particle to drift perpendicular to the plane of gyration. If there is a non-zero electric field, $\mathbf{E}$, perpendicular to $\mathbf{B}$, then its equation of motion is (from Eq. 1.3):

$$m\frac{d\mathbf{v}}{dt} = q(\mathbf{E} + \mathbf{v} \times \mathbf{B}) \tag{1.13}$$

meaning there is an additional force in the direction of the electric field, unbalancing the uniform gyroradius in a similar way to the ∇B drift. The drift velocity resulting from this is known as the $\mathbf{E} \times \mathbf{B}$ drift, $\mathbf{v}_{\mathbf{E}}$, and is given by:

$$\mathbf{v}_{\mathbf{E}} = \frac{\mathbf{E} \times \mathbf{B}}{B^2} \tag{1.14}$$

The $\mathbf{E} \times \mathbf{B}$ drift is independent of particle charge, so ions and electrons flow in the same direction as shown in Figure 1.3. As there is no net separation of charge, and we assume a collisionless system, no current is generated by this type of particle drift in itself. However, any force which can accelerate particles perpendicular to the magnetic field will induce a drift in a similar way an electric field does (known as a general force drift). These would be dependent on charge, and generate a current as a result.

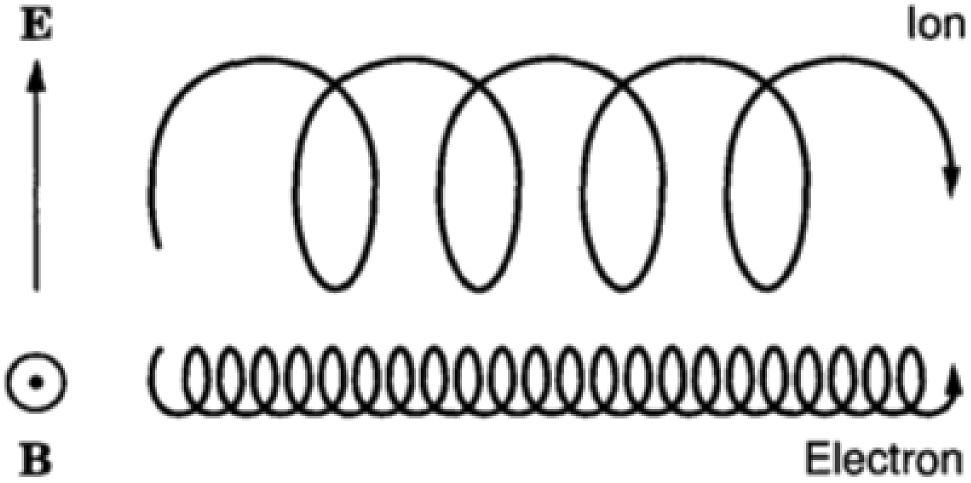

FIGURE 1.3: Diagram of the $\mathbf{E} \times \mathbf{B}$ drift motion for ions and electrons. The magnetic field is directed out of the page, with an electric field pointing upwards. Taken from Baumjohann and Treumann (2012).

1.1.2 Collections of Particles

1.1.2.1 Collisions in a Magnetised Plasma

When considering the single particle motions of ions and electrons, any interactions they may have with other particles that they are flowing through or with are neglected. In the neutral thermosphere of Earth (in which the ionosphere is embedded), the plasma must be considered partially ionised to fully capture both its and the neutrals motion. A force term must be added to Eq. 1.13 which describes the momentum lost due to ion-neutral collisions:

$$m\frac{d\mathbf{v}}{dt} = q(\mathbf{E} + \mathbf{v} \times \mathbf{B}) - m\nu_{in}\left(\mathbf{v} - \mathbf{u}\right) \tag{1.15}$$

where ν_{in} is the ion-neutral collision frequency and $\mathbf{u}$ is the neutral wind velocity. Because the neutral density is much greater than the plasma density, collisions can be idealised as head-on and thus:

$$\nu_{in} = n_n \sigma_n \langle v \rangle \tag{1.16}$$

where n_n is the neutral particle density within a molecular cross section $\sigma_n (= \pi d^2)$. The mean free path length, l, can be defined from this as the average distance a charged particle will travel before colliding with a neutral:

$$l = \frac{\langle v \rangle}{\nu_{in}} = (n_n \sigma_n)^{-1} \tag{1.17}$$

In the ionosphere-thermosphere system, l is much less that the atmospheric scale height from the base of the atmosphere to around ∼500 km in altitude, meaning ion-neutral collisions are frequent enough to be important.

Recalling Ohm's law from Eq. 1.32, the density of a current ($\mathbf{j}$) in a material is directly proportional to the induced electric field by:

$$\mathbf{j} = \sigma \left(\mathbf{E} + \mathbf{v} \times \mathbf{B} \right) \tag{1.18}$$

where σ is the electrical conductivity. In the fully ionised, frozen-in plasma of the solar wind, it was assumed that the conductivity was infinite and so could be treated as a scalar quantity. In the thermosphere ionosphere system however, frequent collisions in the presence of a magnetic field generate a conductivity that varies substantially when measured in different directions.

If we first consider a steady state system with collision partners at rest, then Eq. 1.15 can be written for electrons as:

$$\mathbf{E} + \mathbf{v_e} \times \mathbf{B} = -\frac{m_e \nu}{e} \mathbf{v_e} \tag{1.19}$$

Since the electrons move differentially to the ions, a current is induced:

$$\mathbf{j} = -e n_e \mathbf{v_e} \tag{1.20}$$

Now considering only along the direction of the magnetic field (defined as in the z direction):

$$j_z = \frac{n_e e^2}{m_e \nu} E_z \tag{1.21}$$

where $\frac{n_e e^2}{m_e \nu}$ is now defined here as in the parallel conductivity, $\sigma_{||}$. Perpendicular to the $\mathbf{B}$ field in the x and y directions, we obtain relations for the perpendicular currents by substituting $\sigma_{||}$, Eq. 1.20, and our previous definition for the gyrofrequency (Eq. 1.9) into Eq. 1.19:

$$\begin{aligned} j_x &= \frac{\nu^2}{\nu^2+\omega_{ge}^2}\sigma_{||}E_x + \frac{\omega_{ge}\nu}{\nu^2+\omega_{ge}^2}\sigma_{||}E_y \\ j_y &= \frac{\nu^2}{\nu^2+\omega_{ge}^2}\sigma_{||}E_y - \frac{\omega_{ge}\nu}{\nu^2+\omega_{ge}^2}\sigma_{||}E_x \end{aligned} \tag{1.22}$$

We may now define the conductivities perpendicular to **B**. One, in the direction of the electric field (known as the Pedersen conductivity, σ_P) and the second, perpendicular to both **E** and **B** (known as the Hall conductivity, σ_H):

$$\begin{aligned} \sigma_P &= \frac{\nu^2}{\nu^2+\omega_{ge}^2}\sigma_{||} \\ \sigma_H &= -\frac{\omega_{ge}\nu}{\nu^2+\omega_{ge}^2}\sigma_{||} \end{aligned} \tag{1.23}$$

which completes the definition for the conductivity tensor of a magnetic field aligned along z:

$$\sigma = \begin{pmatrix} \sigma_P & -\sigma_H & 0 \\ \sigma_H & \sigma_P & 0 \\ 0 & 0 & \sigma_{||} \end{pmatrix}$$

The equations presented here apply not only to electrons, but also ions. Both populate the thermosphere and collide with the neutrals, thus the collision frequency can either be ion-neutral or electron-neutral, and the gyrofrequency can be that of the ions or electrons (but recalling that they may drift/gyrate in different directions). Depending on the ratio of the collision frequency to gyrofrequency, either the Pedersen or Hall currents can be dominant. It should be noted that in the lower part of the ionosphere (known as the E-region, ~90-150 km), the ion-neutral collision frequency is much greater than the ion gyrofrequency. Therefore, ions are strongly coupled to the neutrals as many collisions happen per gyrations. Conversely, the electron-neutral collision frequency is much lower than the electron gyrofrequency, so for the most part, they drift at **E** × **B** velocity.

1.1.2.2 Momentum Equation of the Neutral gas

To appreciate the dynamics of neutrals in the thermosphere, we begin with the basic equation which encapsulates all the forcing elements acting on a gas with mass density ρ and velocity $\mathbf{u}$:

$$\rho \frac{d\mathbf{u}}{dt} = \mathbf{f} \tag{1.24}$$

where $\mathbf{f}$ is the force per unit volume, or force density. In the thermosphere, there are 6 major contributors to this force.

Both centrifugal and gravitational forces are traditionally kept together as an overall acceleration value $\mathbf{g}$. The force density due to both is therefore given by:

$$\mathbf{f_g} = \rho \mathbf{g} \tag{1.25}$$

Over the thermospheric altitude range, g varies a negligible amount.

If there is a gradient of pressure within the gas, there is an implied force difference between pressure levels. This directly results in an acceleration due Newton's second law of motion, which in terms of force density is:

$$\mathbf{f_p} = -\nabla p \tag{1.26}$$

Large thermospheric pressure gradients arise due to differential heating between the dayside and nightside atmospheres, causing a broadly anti-sunward neutral wind at all latitudes. This is one of the largest terms contributing to neutral acceleration, and so was one of the first to be accurately modelled. For example, Figure 1.4 shows a polar plot of northern hemisphere neutral winds, centred on the geographic pole, derived by Kohl and King (1967) using a temperature gradient model by Jacchia (1965). Due to the rotation of earth (anti-clockwise in the Figure), the peak in temperature, and thus the foci of highest pressure, is actually slightly post-noon.

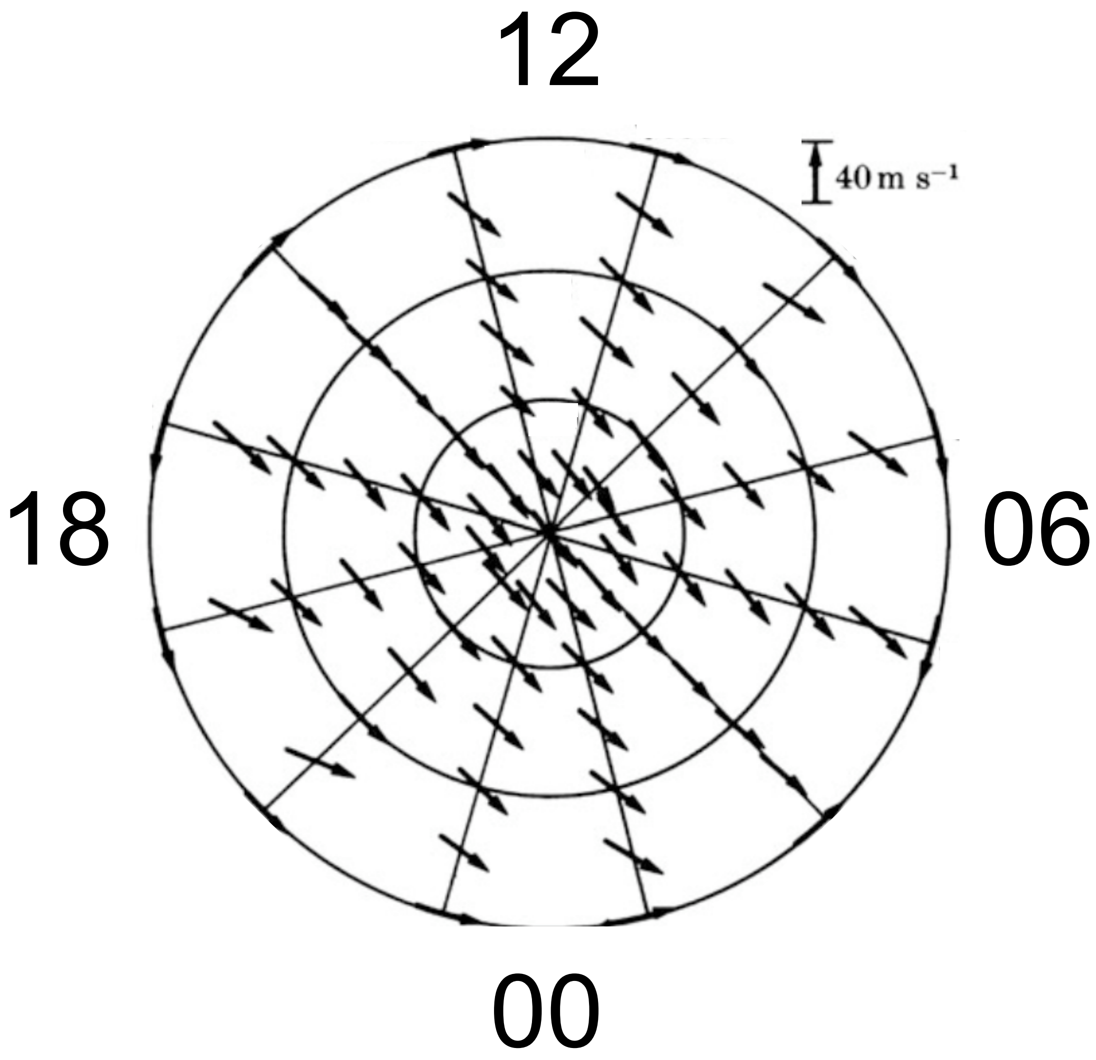

FIGURE 1.4: Neutral wind vectors in a polar plot centred on the geographic pole, with the Sun at the top and solar local time (SLT) hours around the outside. From Kohl and King (1967) using the Jacchia (1965) neutral temperature model. The figure has been modified slightly such that the Sun is at the top (12 - noon SLT). Lines of constant latitude are separated by 30°, with the outer edge being the equator.

In the reference frame of the rotating Earth, the Coriolis force deflects gas to the right in the northern hemisphere and to the left in the south:

$$\mathbf{f_C} = -2\rho\Omega \times \mathbf{u} \tag{1.27}$$

where Ω is the Earth's angular velocity.

Shears that arise due to differences in the neutral flow velocity cause a frictional deceleration related to its viscosity, μ:

$$\mathbf{f_v} = -\mu \nabla \mathbf{u} \tag{1.28}$$

Finally, collisions with colocated charged particles (described in the previous section) either drag on the neutral gas or accelerate it, depending on if it is faster or slower. This is known as the ion-drag effect:

$$\mathbf{f_{drag}} = -\rho \nu_{in} \left(\mathbf{v} - \mathbf{u} \right) \tag{1.29}$$

Adding all of these terms to Eq. 1.24 gives the complete thermospheric momentum equation for the neutral particles:

$$\rho \frac{d\mathbf{u}}{dt} = \rho \mathbf{g} - \nabla p - 2\rho \Omega \times \mathbf{u} - \mu \nabla \mathbf{u} - \rho \nu_{in} \left(\mathbf{v} - \mathbf{u} \right) \tag{1.30}$$

1.2 The Solar Wind Interaction with the Magnetosphere

1.2.1 Origin of the Solar Wind

The outer atmosphere of the Sun, the corona, consists of an extremely hot, highly structured plasma that reaches around 10^6 K. It is anomalously hotter than the solar surface (the photosphere), and even the upper parts of the interior, and is still the subject of many studies which attempt to understand its mechanisms. What is understood however, is that the coronal structure, and in turn its ejection of matter into the interplanetary medium, is closely linked to coronal holes.

As shown in Figure 1.5, the Sun's exterior magnetic field is complex. This is mainly due to a couple of factors, the foremost of which is the Sun's differential rotation rate. At the equator, one rotation takes around 24.5 days compared with 38 days near the poles. This results in the interior magnetic field, which is approximately dipoler under the surface during solar minimum, becoming wound up and twisted in the corona.

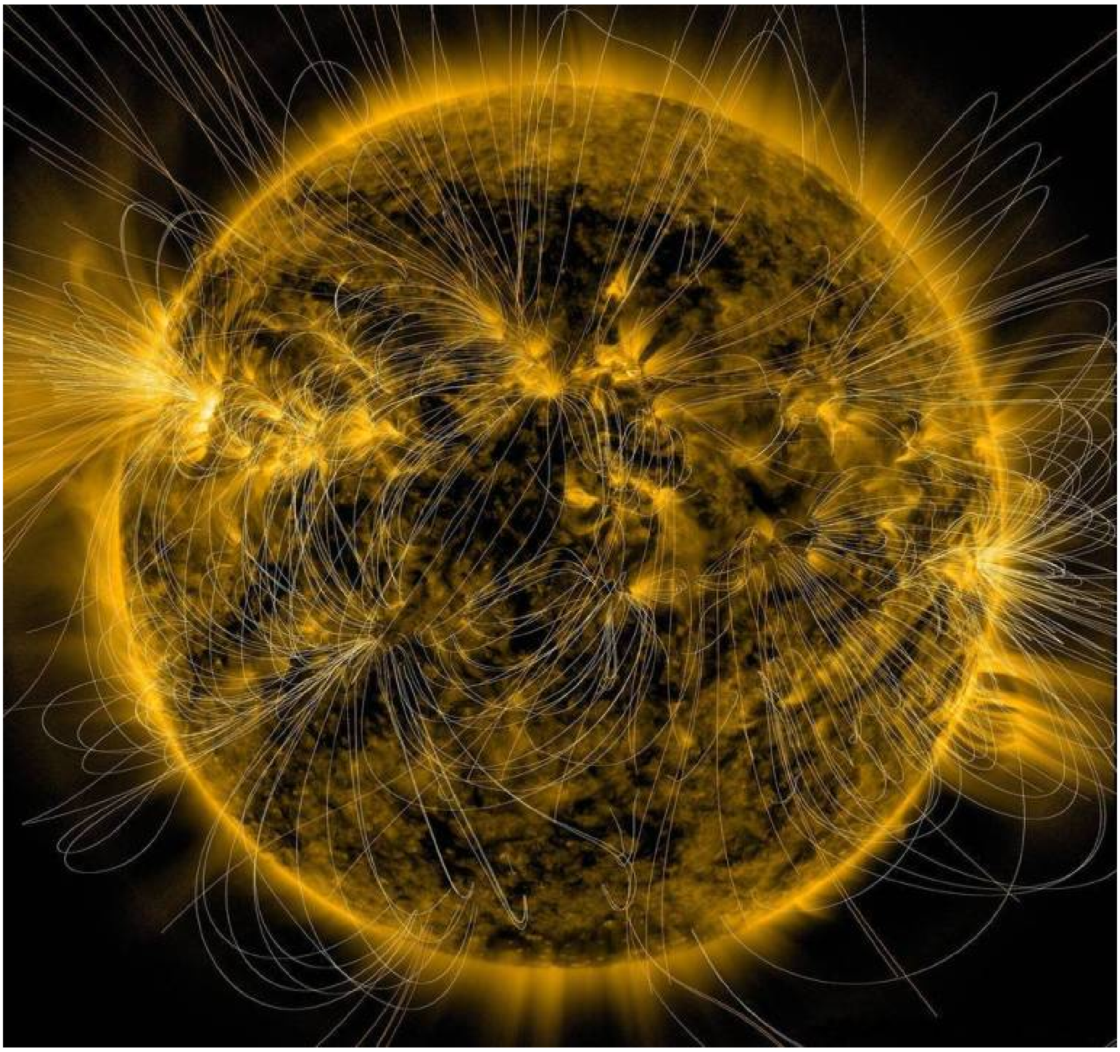

Figure 1.5: An image of the Sun taken with the Solar Dynamics Observatory spacecraft, and magnetic field lines overlain using the Potential Field Source Surface model. Image: NASA/SDO/AIA/LMSAL

Where the magnetic field lines are tied to the Sun, or ‘closed’ in a loop, is where coronal matter is not allowed to escape and instead cools to the photospheric surface, forming sunspots. Where they extend outwards however is where plasma is released at a high speed, due to the pressure difference between it and the tenuous interplanetary medium gas. This material is now not bound to the Sun, and becomes known as the fast solar wind (average velocity $\sim$750 ms^{-1}). A source of slower solar wind is also present, and currently is believed to originate from boundaries between coronal holes and streams of coronal plasma near closed field lines (average velocity $\sim$400 ms^{-1}). The ratio of fast to slow solar wind emitted over the entire Sun is dependent on the 11 year solar cycle, as coronal holes dominate during solar minimum, whilst they are rare at maximum.

1.2.2 The Frozen-in Theorem

Ohm's law states that the current density ($\mathbf{j}$) is related to electric field in the reference frame of an observer ($\mathbf{E}$). Its generalised form is derived by taking the difference between ion and electron momentum equations (noting that the current is proportional to the differential motion of the two), and is given by:

$$\mathbf{E} + \mathbf{v} \times \mathbf{B} = \eta \mathbf{j} + \frac{\mathbf{j} \times \mathbf{B}}{n_e e} + \frac{\nabla \mathbf{P}}{n_e e} + \frac{m_e}{n_e e^2} \frac{d\mathbf{j}}{dt} \tag{1.31}$$

where $\mathbf{v}$ is the plasma velocity, $\mathbf{B}$ is its magnetic field, $\mathbf{j}$ is the current density, η the electrical resistivity, $\mathbf{P}$ is the total pressure tensor and n_e, e and m_e are the electron density, charge and mass respectively. The second, third and fourth terms on the right hand side of Eq. 1.31 represent electric fields due to the Hall effect, ambipolar diffusion and electron inertia respectively, which can all be safely neglected because they are small in the solar wind, and by assuming variations in $\mathbf{j}$ occur slowly. Substituting in the inverse of the resistivity, the electrical conductivity (σ), we get:

$$\mathbf{E} + \mathbf{v} \times \mathbf{B} = \frac{\mathbf{j}}{\sigma} \tag{1.32}$$

Which essentially ignores the electrons due to their much smaller mass compared to the ions. In the solar wind, the plasma is highly conductivity such that σ tends to infinity, thus:

$$\mathbf{E} = -\mathbf{v} \times \mathbf{B} \tag{1.33}$$

Substituting into the Maxwell-Faraday equation:

$$\frac{d\mathbf{B}}{dt} = \nabla \times (\mathbf{v} \times \mathbf{B}) \tag{1.34}$$

shows us that the plasma flow is intrinsically "frozen-in" with the magnetic field, i.e. one cannot move without dragging the other, as originally postulated by Alfvén (1942). This high conductivity approximation is appropriate for the coronal and solar wind plasma, due to its negligible proportion of non-ionised particles. Thus, the solar wind moves with the interplanetary magnetic field (IMF).

The ratio of plasma pressure to magnetic pressure, known as the plasma beta quantity, tells us whether it is the magnetic field that dictates the movement of the plasma, or vice versa:

$$\beta = \frac{P_{plasma}}{P_{field}} = \frac{N k_B T}{B^2/(2\mu_0)} \tag{1.35}$$

where N is the plasma density, T is temperature, B^2 is the magnetic field strength, k_B is Boltzmann's constant and μ_0 is the permeability of free space. In the corona, β<1 so the magnetic field controls the plasma (hence the formation of coronal loops, and other banded structures on closed field lines). In the solar wind, the magnetic field is weaker and so β>1. The plasma drags the magnetic field along with it, radially outwards from the Sun. The magnetic field line is anchored to the Sun however, where plasma is still being ejected. Assuming a constant flow of particles, the magnetic field line bends with time as its footprint moves with solar rotation. If the outflow is uniform around the Sun, the IMF takes the form of a spiral shape which can be seen schematically in Figure 1.6. The sector boundaries illustrate where the Sun's magnetic field polarity changes. In reality however, varying solar wind speeds, solar differential motion and varying magnetic field strengths mean that this spiral structure is in fact a complex 3D plasma sheet that varies in shape constantly, making it extremely difficult to predict.

1.2.3 Magnetic Reconnection at Earth

Once the solar wind and the frozen-in IMF reaches Earth, there is interaction with the terrestrial magnetosphere. The foundation of this interaction begins with magnetic reconnection.

Consider two pairs of oppositely directed magnetic field lines such as those shown in Figure 1.7 at time t_1. Due to Ampere's law, a current sheet is formed in the boundary and the $\mathbf{j} \times \mathbf{B}$ force pushes plasma on either side toward it. $\mathbf{B}$ is frozen-in, so field lines also bend inwards, following the plasma. Because the magnetic field gradient is very large here, the plasma and magnetic field decouple due to drifts arising in the

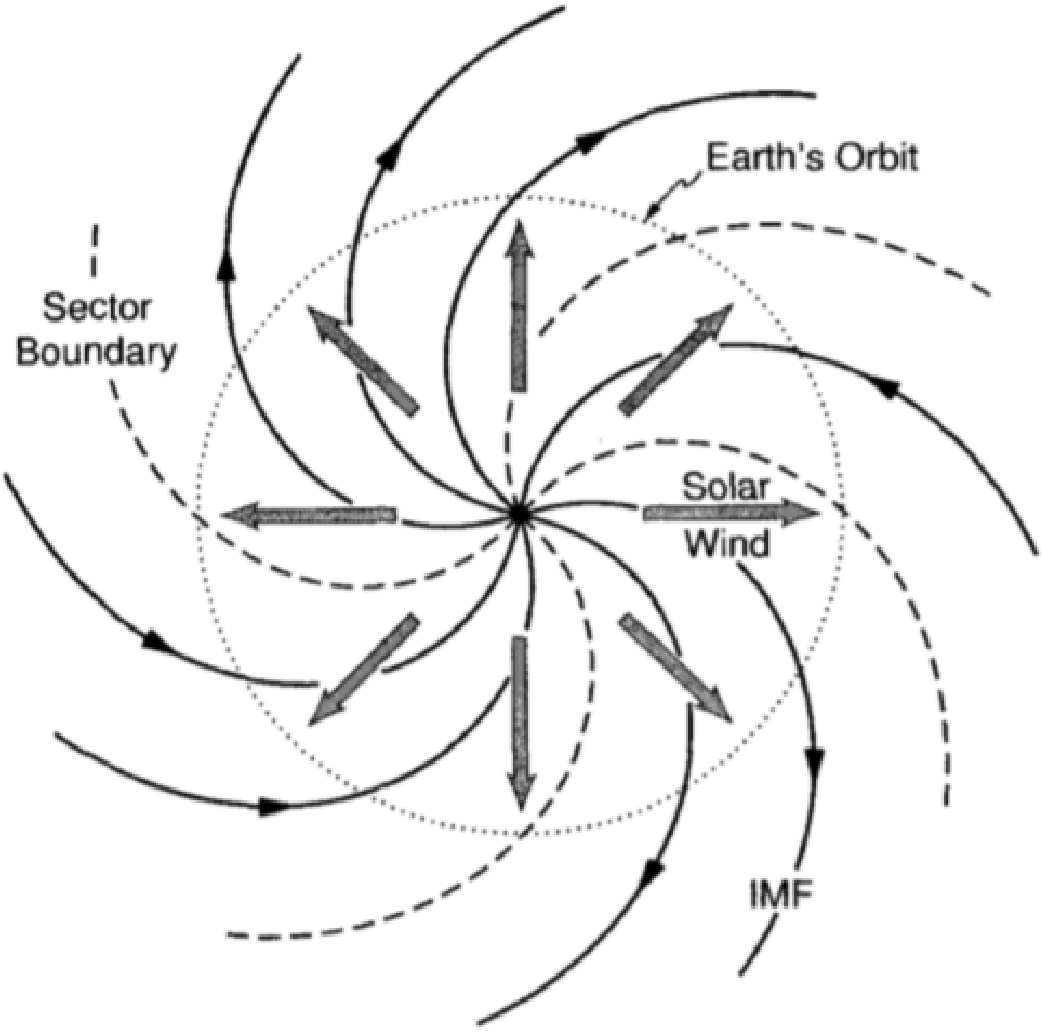

Figure 1.6: Top-down view of an idealised IMF structure. Image taken from Baumjohann and Treumann (2012).

plasma (discussed in more detail in section 1.1.1). The field lines reconnect and they diffuse through (t_2) and a plasma outflow, also driven by the $\mathbf{j} \times \mathbf{B}$ force, carries the magnetic field away perpendicular to the inflow. This kind of reconnection is known as the Sweet-Parker model.

Of course, the reconnection model shown in Figure 1.7 is a 2D representation of a 3D process. In reality, because the IMF can be orientated in any direction when it arrives at Earth, reconnection can occur at multiple different regions of the Earth's magnetopause. For instance, two differently orientated IMF scenarios are presented in Figure 1.8, from the view of an observer looking at the dayside magnetopause with their

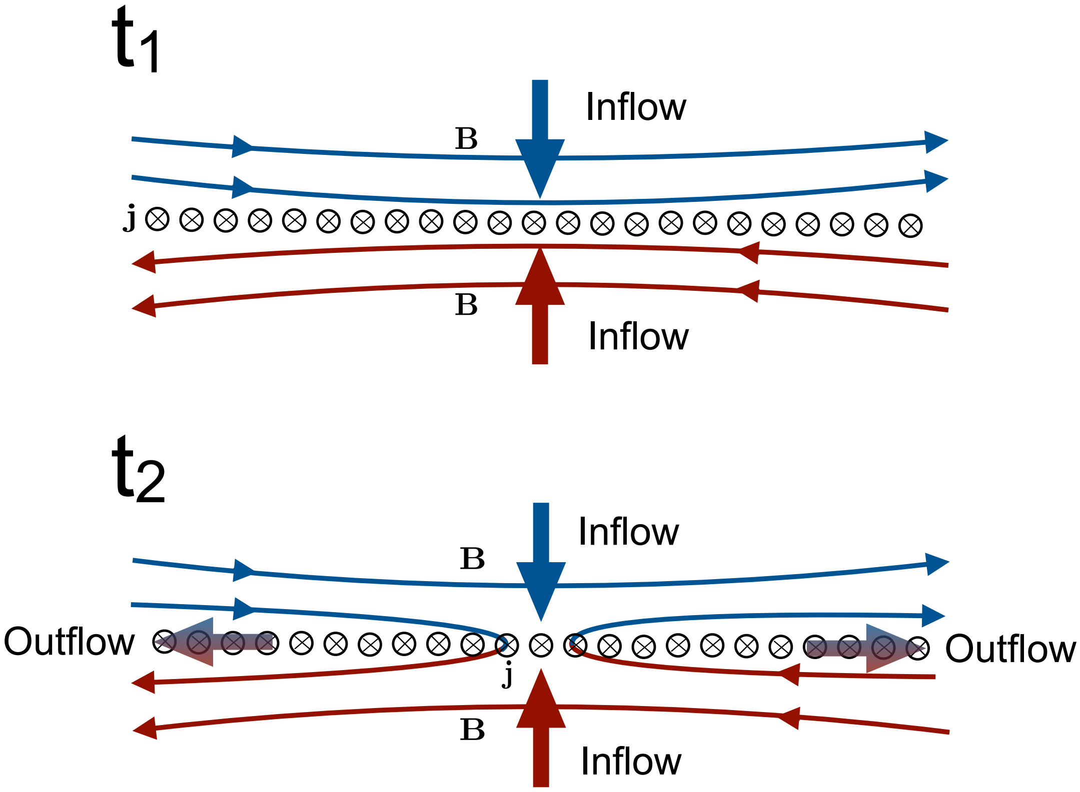

FIGURE 1.7: Diagram of Sweet-Parker reconnection taking place between times t_1 and t_2.

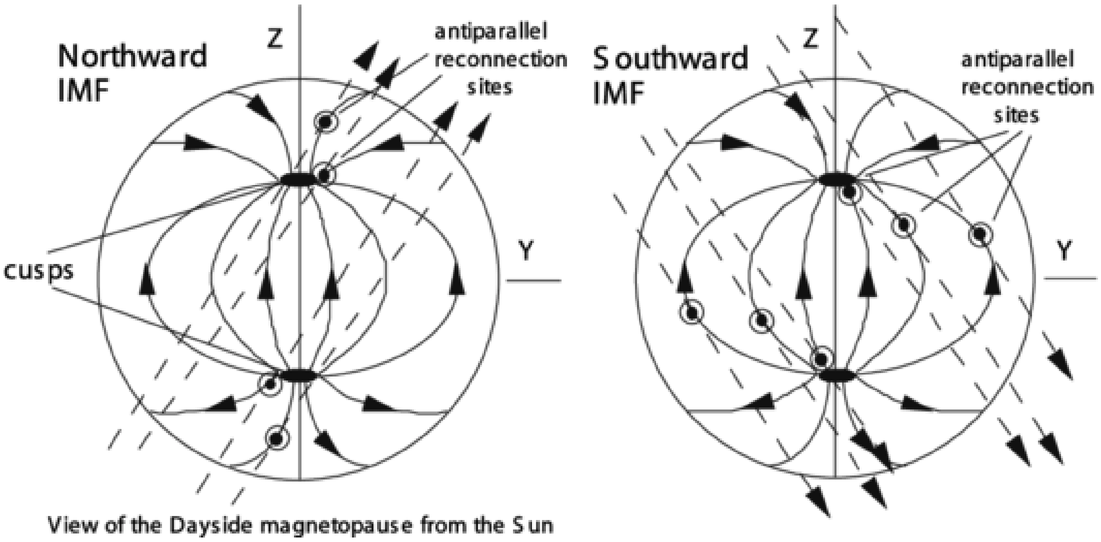

FIGURE 1.8: Head on view of the dayside magnetopause with a back to the Sun, adapted from Fuselier et al. (2003). Two IMF orientations (dashed lines), along with the points where reconnection would occur are shown.

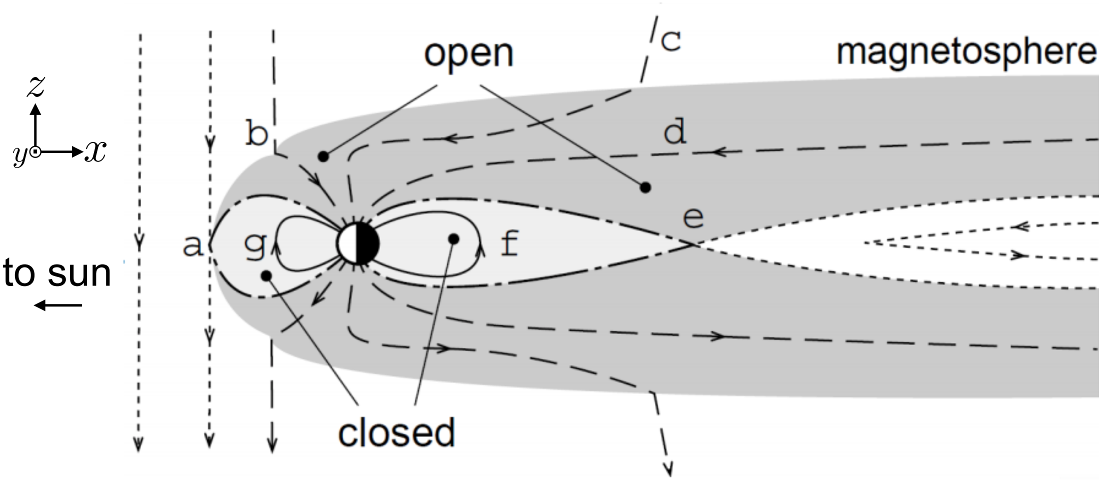

FIGURE 1.9: Diagram of the Dungey cycle at Earth for increasing time (a-g). The coordinate system shown is GSM. From Milan et al. (2003), adapted.

back to the Sun. The dashed lines are the IMF, whilst the solid lines are the terrestrial magnetosphere. The two IMF orientations are B_z/B_y positive and B_z negative/B_y positive. Earth rotates from left to right in this frame, so dawn is to the left (negative y) whilst dusk is to right (positive y). The points at where the IMF and terrestrial field lines are anti-parallel are where Sweet-Parker reconnection can occur on the dayside, but the number of all possible reconnection sites for all IMF orientations is practically limitless.

1.2.4 The Dungey Cycle

Dungey (1961) first proposed what has now come to be known as the Dungey cycle, as a way of describing how solar wind plasma is convected across from the dayside to the nightside of Earth. This is the largest cyclic process within the Earth's system, and as we will see later, is responsible for large scale motions within the Earth's ionosphere.

The Dungey cycle is most simply envisioned by considering a case of purely southward orientated IMF, and is shown fully in Figure 1.9. This is defined as parallel to the Earth's dipole field at the dayside magnetopause (along the z direction), with a polarity pointed towards the south geomagnetic pole. Both the x and y directions of this coordinate system, known as geocentric solar magnetospheric (GSM), are also shown in Figure

1.9. The dark grey shaded region is the boundary between Earth and solar wind plasma regimes (the magnetopause), and the lighter grey is“trapped” plasma on closed magnetic field lines. At time (a), reconnection occurs at the dayside magnetopause, opening field lines which where previously closed. The differing plasma populations mean frozen-in field lines in the IMF and magnetosphere travel at different rates towards the nightside, bending the field line (b). Pressure from the solar wind continues to convect the field line across the pole (c) and to the nightside where it is stretched out into the magnetotail (d). A current sheet similar to that shown in Figure 1.7 is formed between the opposing field lines in the northern and southern tail lobes, causing them to eventually ‘pinch’ together and reconnect (e), closing the field line. This process ejects plasma anti-sunward in the form of a plasmoid, and earthward which compresses the field (f). Finally, the closed field line convects back across to the dayside on the dawn and dusk flanks (g). If B_y was non-zero, the Dungey cycle could still occur with modified reconnection sites and a tilted morphology towards dawn and dusk.

1.3 The High-Latitude Ionosphere

From approximately 75 km to 1000 km altitude in the Earth’s atmosphere lies the ionosphere. As we have seen in the previous section, it is a partially ionised plasma that is embedded within the neutral thermosphere and at its very top, the exosphere. The following section will describe how this conducting layer of atmosphere is formed, its structure, the formation and properties of the auroral ionosphere, and finally the dyanmics which occur at high latitudes due to coupling with the Dungey cycle driven magnetosphere.

1.3.1 Formation & Structure

There are two main sources of ionisation which contribute to the ionosphere: solar ultraviolet (UV) radiation and particle precipitation sourced from the magnetosphere. The latter of these also emits radiation in visible wavelengths during the ionisation process, which results in the aurora. For the most part, UV photons are the only solar radiation frequencies which have an energy and intensity suitable enough for photoionisation of thermospheric constituents.

1.3.1.1 Solar UV Ionisation

The main contributor to the ionisation rate is the neutral particle density, n, which varies most with altitude (z) and follows the relationship for an isothermal atmosphere (e.g. Brekke (2012)):

$$n = n_0 \mathrm{exp}(-z/H) \tag{1.36}$$

where n_0 is the density at a reference altitude $z_0 = 0$. H is the atmospheric scale height, which is the distance by which the neutral density decreases by $1/e$. Radiation of intensity I will decay by dI according to the number of neutral ionisation partners it meets within a small distance ds. This is also dependent on the cross-section of ionisation, σ_i, by:

$$\frac{dI}{ds} = -n\sigma_i I \tag{1.37}$$

This produces a number of electrons, C, also known as the ionisation efficiency. The number of electrons produced per cubic meter per second is the electron production rate, q_i:

$$q_i = -C\frac{dI}{ds} \tag{1.38}$$

For single atoms, all incident energy is assumed to create an electron-ion pair (C=1). C is less than 1 for molecules.

As the altitude increases, n decreases and I increases. Because C and σ are constants for a particular neutral species, there will be a electron production altitude peak where the product nI is a maximum (see Figure 1.10). Overall, the production of O^+ ions is dominant over 200 km, whilst O_2^+ production is dominant below $\sim$ 130 km. This will vary greatly on factors that affect the intensity of light (e.g. season, day/night), geographic location (i.e. the angle the photon makes to the ionospheric slab of distance ds) and wavelength of the ionising photon (shorter wavelengths penetrate deeper).

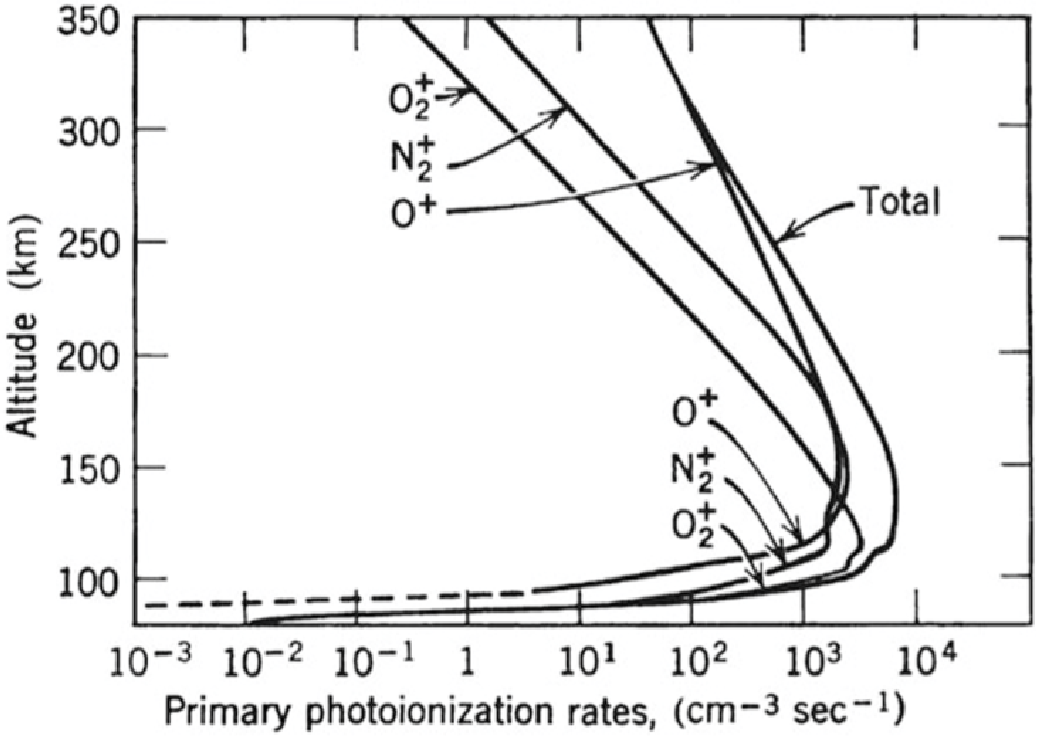

FIGURE 1.10: Photoionisation rates of different molecules in the ionosphere, as calculated by Hinteregger et al. (1965)

1.3.1.2 Particle Precipitation Ionisation

At high latitudes particularly, ionisation also occurs because of energetic particles travelling down magnetic field lines from the magnetosphere and solar wind (in the case of closed and open field lines, respectively). On the nightside, they can also be sourced from large particle injections due to magnetotail reconnection (known as substorms). Unlike photoionisation by solar UV photons, ionisation by particle precipitation occurs due to direct collisions of gyrating protons and electrons with a neutral atom or molecule. If the energy of the precipitating particle is greater than the ionisation energy of the neutral, it will knock electrons off. Energetic electrons and protons also lose energy however as they experience collisions, so more energetic particles generally reach lower altitudes. This is particularly true for electrons, which have a higher ionisation efficiency. Electron precipitation is therefore responsible for an ionisation peak around 100 km, whilst proton precipitation produces an ionisation peak around 130 km, both of which depend on the state of the magnetosphere.

1.3.1.3 Recombination and Layers

Reactions occur between the newly ionised atoms and molecules with the free electrons they produced in order to re-establish equilibrium. For instance, electrons may directly recombine with an ion to form a neutral atom and photon (of energy hf, where h is Planck's constant and f is frequency) through radiative recombination:

$$X^+ + e \rightarrow X + hf$$

Alternitively, and more commonly due to a more efficient conservation of energy, dissociative recombination can occur in molecular ions:

$$XY^+ + e \rightarrow X + Y$$

In both cases, we assume both production and loss of ions are equal, and thus the total number density of positive ions is equal to the electron density. In reality, ionisation and recombination are happening concurrently at all altitudes at varying rates - leading to the characteristic “layered” ionosphere such as that shown in Figure 1.11. Due to varying production and loss rates with changing universal time (UT), season, and geographic location, these layers are by no means static. Therefore, it is sometimes useful to define layers by the shape of an electron density profile instead of defining strict altitude ranges. For example, the differing altitudes of ionisation peaks due to electron and proton precipitation can cause mini electron density peaks at high latitudes, which would be even more pronounced on the nightside when photoionisation is at a minimum. Despite a large amount of possible variation, both the E and F regions very generally fall within the ranges of 90-150 km and 150+ km respectively. The D-region however is a dayside phenomena due to free electrons recombining with oxygen ions at night, and is ionised so weakly that it cannot be fully described by the plasma dynamics discussed in this chapter. Incoherent scatter radars are typically used to measure these electron

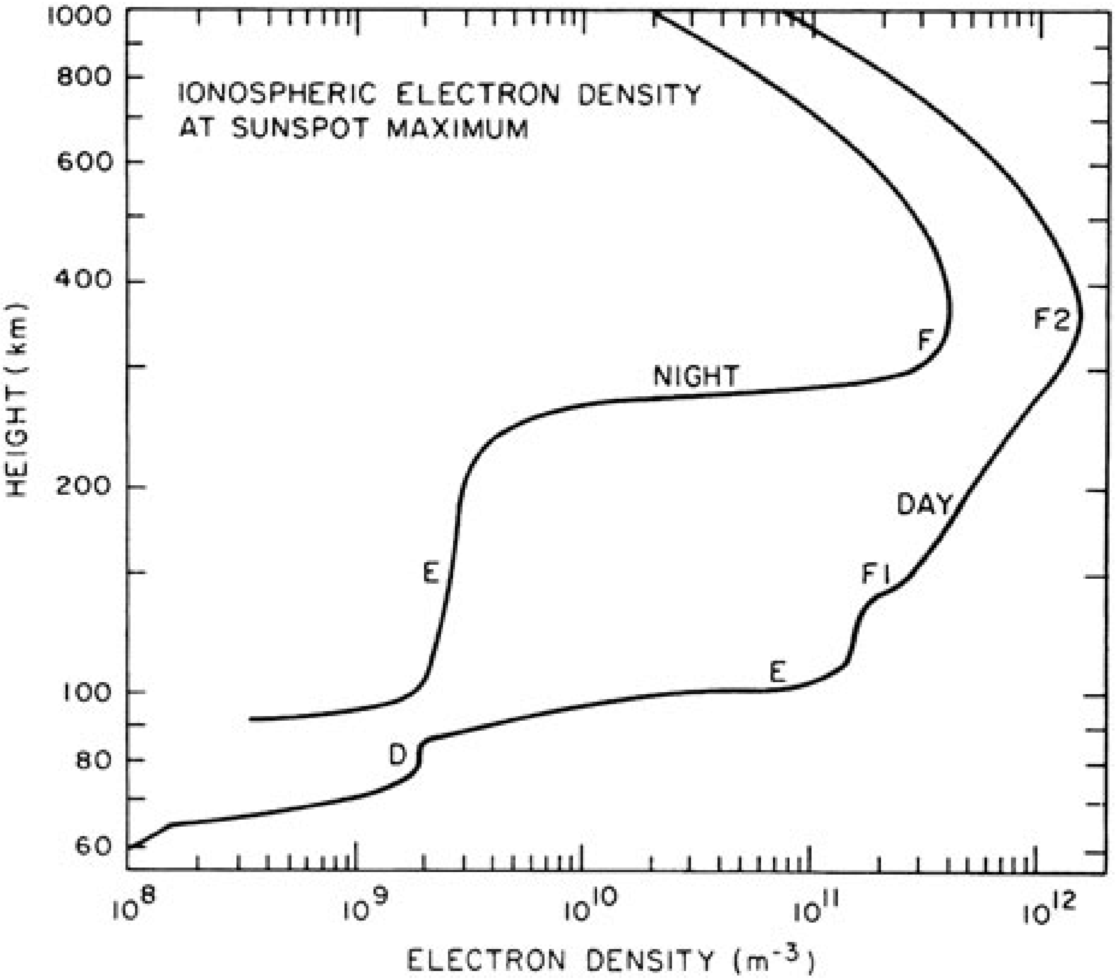

FIGURE 1.11: Idealised electron density profiles of the ionosphere from Hagfors and Evans (1968).

density height profiles at all altitudes, one of which is discussed in more detail in section 2.3.

1.3.2 The Aurora

As mentioned previously, ionisation by particle precipitation is collisional. This collision leaves the atom, molecule or ion in an exited state due to gaining energy in the momentum transfer of the collision. The excited particle then “relaxes” to its original energy state by emitting a photon, or when it collides with another particle (thus transferring the energy on once more). The energy of the photon in the prior case, hf, is equal to

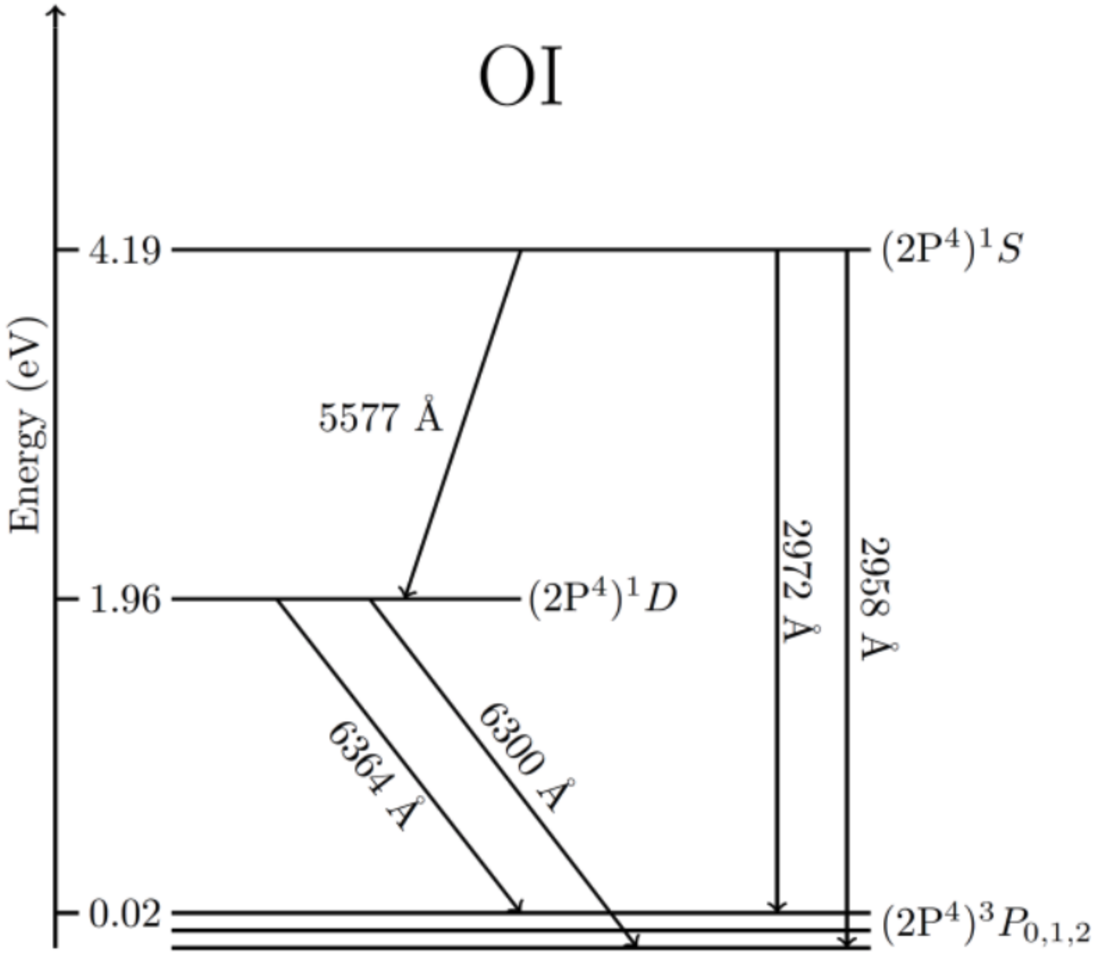

FIGURE 1.12: Possible auroral emissions of atomic oxygen due to transitions between the 4.19 eV (^1S), 1.96 eV (^1D) and 0.02 eV (^3P) states. Modified from Bhardwaj and Raghuram (2012).

the energy difference of the excited and relaxed states. So its wavelength is:

$$\lambda = \frac{hc}{E_2 - E_1} \tag{1.39}$$

where h is Planck's constant, c is the speed of light, and E_2 and E_1 are the energies of the excited and relaxed states respectively. Due to the varying composition of the ionosphere, the differing rest energies and possible excited states, numerous different wavelengths of light are emitted at several different altitudes. Single particles can also have several different characteristic emissions corresponding to various energy state transitions, which could be between an excited and ground state, or even two excited states in a gradual relaxation. For instance, Figure 1.12 shows the possible transitions of the thermospherically abundant atomic oxygen from the excited (^1S) and (^1D) states. The 5577 Å(557.7 nm) photon corresponds to the well known green line auroral emission, whilst the 6300 Å(630.0 nm) is red. Most of auroral emissions are 557.7 nm, which occur mainly below 150 km. 630.0 nm requires lower energy electrons, and so has a peak emission altitude near 250 km.

The energy of precipitating particles and their geographic location in the ionosphere varies considerably depending on the configuration of the magnetosphere. Nearly all of the visible aurora (red and green oxygen emissions) occurs in a misshapen ring around the geomagnetic poles known as the auroral oval. This roughly corresponds to boundary between open and closed magnetic field lines (modulated by Dungey cycle reconnection, see section 1.2.4), and divides the region between high energy (>21 keV) "trapped" electrons on closed field lines and even higher energy (>40 keV) "polar rain" on open (i.e. the open-closed field line boundary). Particles precipitating into the auroral oval are typically <21 keV and originate directly from the solar wind (i.e. dayside reconnection), or from the tail (due to reconnection in the nightside plasma sheet). Precipitating particles into the cusp, the dayside region of the ionosphere that maps to the dayside magnetopause, have the lowest energy as they do not get accelerated much. Thus they are responsible for the weak cusp aurora. The ovals overall equatorward extent is dependent on the flux content of the open polar cap; i.e. if field lines are being consistently opened on the dayside without being closed on the nightside or elsewhere, the auroral oval will extend to lower latitudes. Because of this close dependence of the aurora on the conditions of the IMF, non-southward B_z conditions can lead to significant structural changes of the auroral morphology.

1.3.3 Coupling to the Magnetosphere

We have seen already with the auroral oval that the high latitude ionosphere is very closely linked to the magnetosphere undergoing the Dungey cycle. Under steady state conditions where the amount of flux being opened on the dayside by magnetopause reconnection is equal to that being closed on the nightside via tail reconnection (and there is no IMF B_y component), a symmetric two-cell convection pattern of ionospheric plasma

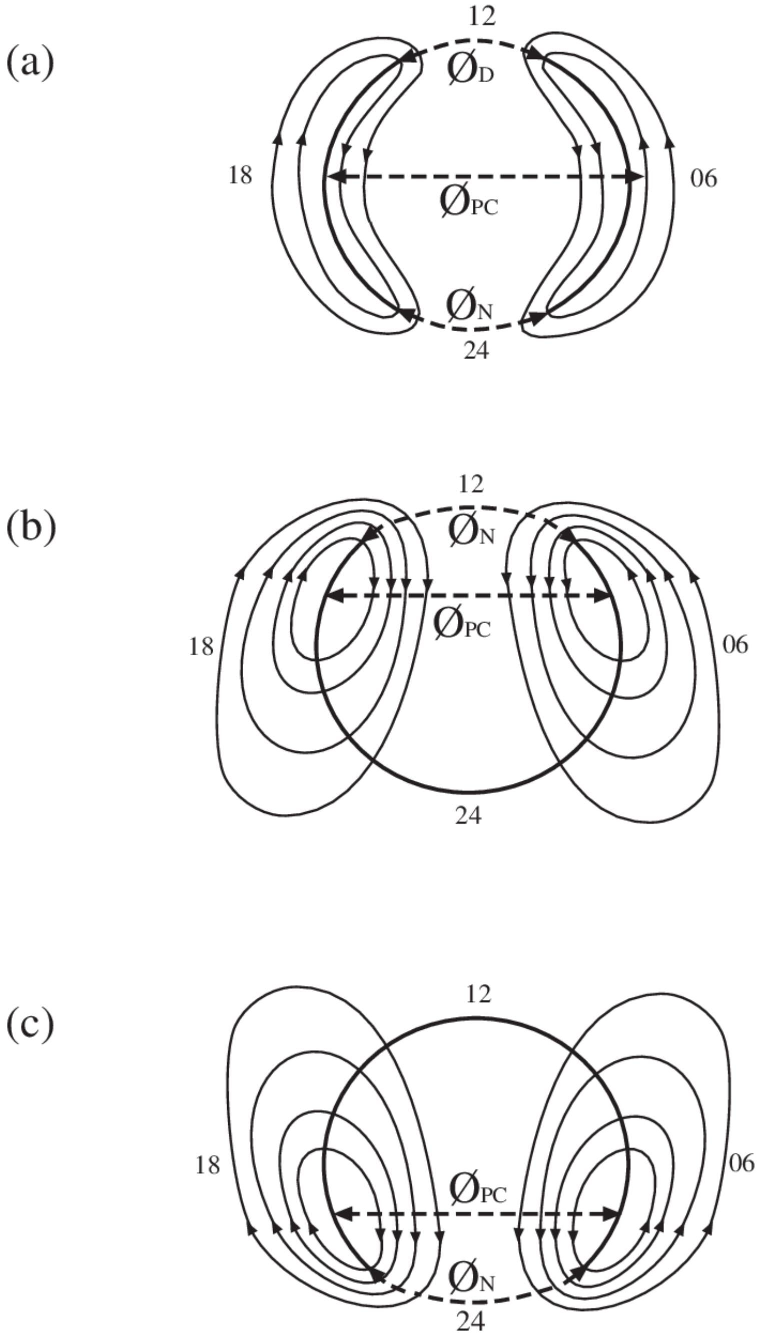

FIGURE 1.13: Examples schematics of ionospheric convective flow under [a]: Steady state dayside and nightside reconnection, [b]: Dayside reconnection only, [c]: nightside reconnection only, from Provan et al. (2002b). Each schematic is presented in a magnetic local time (MLT) system, centred on the magnetic pole with the Sun at the top and dawn to the right.

is formed (Figure 1.13a). This is the result of two processes which can be considered seperately: the case where only dayside reconnection is occuring and causing the polar cap to enlarge from the increase of open flux (anti-sunward convection, Figure 1.13b), and where only nightside reconnection is occuring causing the polar cap to shrink due to flux being removed (sunward convection, Figure 1.13c). Both cases are the result of a polar cap attempting to regain the balance of pressure and "circularize" the open-closed field line boundary (black line, though due to solar wind pressure on the magnetosphere it is actually an oval; Cowley and Lockwood (1992)).

We know from previously that the convecting plasma will have an associated electric field:

$$\mathbf{v} = \frac{\mathbf{E} \times \mathbf{B}}{B^2} \tag{1.40}$$

which will have an electric potential:

$$\mathbf{E} = -\nabla\Phi \tag{1.41}$$

Φ_D and Φ_N in Figure 1.13 are the dayside and nightside cross-boundary potential differences, between the locations where flux is opened and closed respectively. Φ_{PC} is the cross-polar-cap potential. Because the cross-polar electric field is directed from dawn to dusk (in the $-\mathbf{v} \times \mathbf{B}$ direction), the dawn cell has a positive potential and the dusk cell a negative under the conditions presented in Figure 1.13a.

Due to the constant changes of the IMF orientation the Earth will experience as it moves through the IMF spiral (see section 1.2.2), the steady state example shown in Figure 1.13a (which can only occur under purely southward IMF B_z) is unlikely to be commonly realised. As the solar wind/magnetosphere reconnection site yaws towards the dawn or dusk (depending on B_y) or moves to very high latitudes on the dayside (for extremely northward B_z), the overall convection pattern will respond accordingly. Figure 1.14 shows this IMF dependence in statistical patterns, which were generated using ionospheric velocity data from many ground based radars known as the Super Dual Auroral Radar Network (SuperDARN; described more in section 2.1). The dependence on B_y is clear in that it tilts the orientation of the anti-sunward flow, where as a positive B_z causes the polar cap to shrink significantly and convection to weaken. A purely southward IMF ($B_y = B_x = 0$, B_z negative) is the closest to the idealised picture of Figure 1.13a, but even this convection pattern in reality is tilted slightly both on the

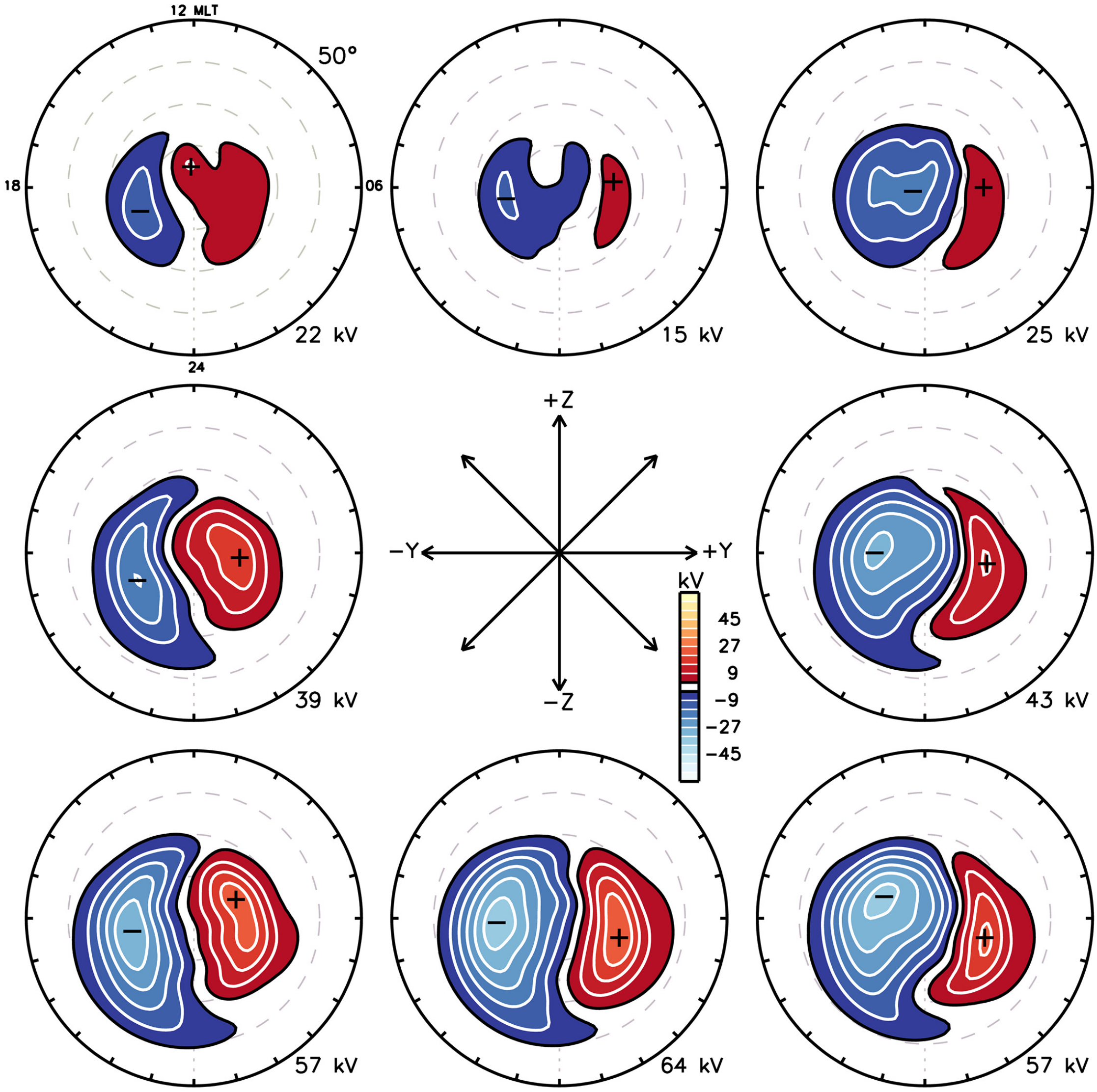

FIGURE 1.14: Statistical patterns of the high latitude ionospheric convection, based on IMF clock angle and a solar wind electric field between 1.6 and 2.1 mV/m. Colours represent the electric potential, with Φ_{PC} shown at the bottom right of each pattern. The coordinate system is also in an MLT format, with the Sun at the top and dawn to the right. From Thomas and Shepherd (2018).

dayside and nightside due to day-night conductivity gradients pushing plasma dawnward (Atkinson and Hutchison, 1978). On the nightside, the dusk cell is additionally enhanced by sub-auroral polarisation streams (SAPS) that contribute to westward flows post midnight.

Even though these statistical patterns presented by Thomas and Shepherd (2018) are climatological, they still allude to the complex nature of the convection in certain regions. Under positive B_z with a negative and zero B_y component for instance, the so-called double convection reversal occurs due to reconnection above 80° MLAT (top-left and top-middle panels of Figure 1.14, where the convection cells become deformed on the dayside). During highly variable solar wind driving conditions, the real-time convection pattern is however a mix of many different statistical features ranging from mesoscales (∼100s kilometers) to global.

1.3.4 Coupling to The Thermosphere

In the neutral momentum equation derived earlier, the acceleration due to coupling with the ionosphere is:

$$\frac{d\mathbf{u}}{dt} = \nu_{in} \left(\mathbf{v} - \mathbf{u} \right) \tag{1.42}$$

At equatorial and mid latitudes (0-50° MLAT), $\mathbf{u}$ is typically faster than $\mathbf{v}$ mainly due to solar pressure gradient acceleration. This term is therefore negative, hence the name "ion-drag". At high latitudes however, as a result of the much faster convection, the term becomes positive. $\mathbf{v} - \mathbf{u}$ can in fact be quite large, resulting in a significant neutral wind acceleration in the direction the plasma is flowing. So statistically, the high latitude neutral wind pattern resembles that of the plasma convection (Figure 1.15). Other terms in the full momentum equation (Eq. 1.30) deviate the neutrals from perfect coupling, mainly the pressure gradient and viscous accelerations. This is why dawn and dusk cells usually only partially form, especially at dawn, which is also counteracted by the Coriolis force.

1.4 Joule Heating

Joule heating, otherwise known as resistive heating, is the energy dissipation due to current driven particles colliding with a conductor. On a microscopic level, a charged particle exchanges momentum with a neutral upon collision and becomes randomly scattered, thus converting kinetic energy to thermal. In the upper polar atmosphere, the

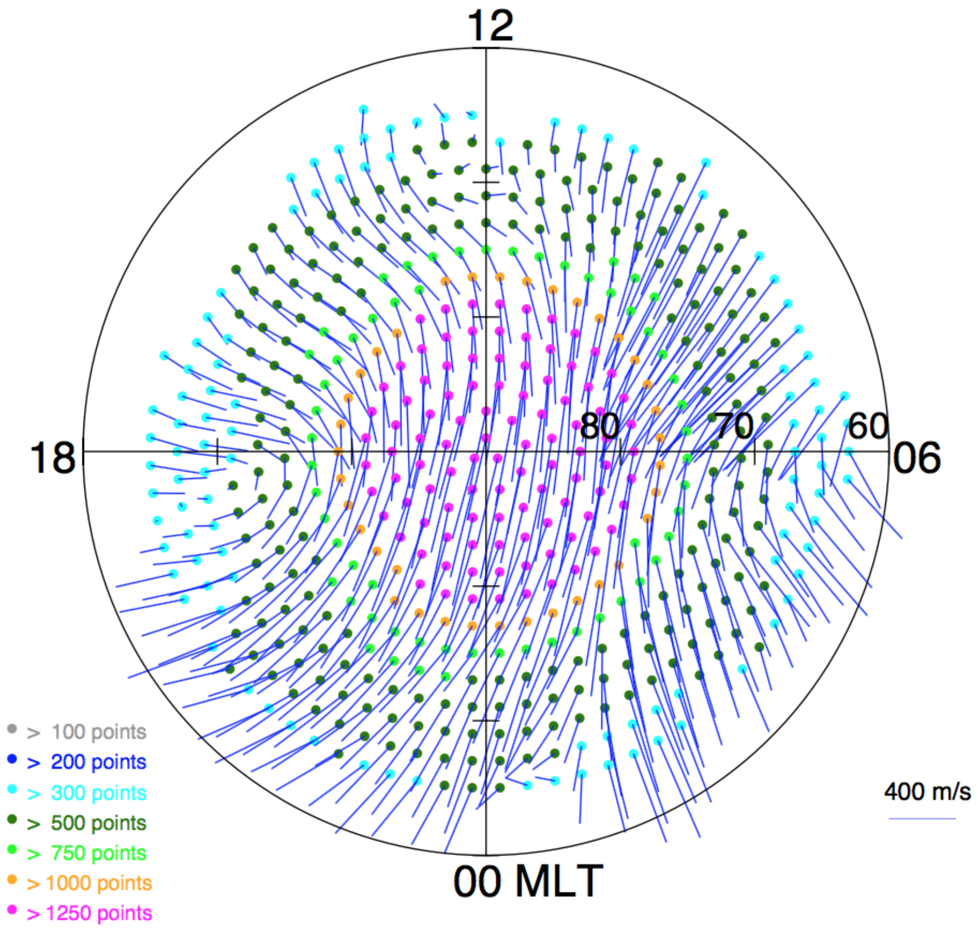

FIGURE 1.15: Statistical neutral wind pattern of the northern hemisphere for 2003, derived from CHAMP satellite measurements. From Forster et al. (2008).

current driven particles are those formed within the ionosphere that are under the influence of the large scale Dungey cycle convection mechanism. The conductor is the neutral thermosphere.

In its simplest form, Joule heating can be determined from Ohm's law as the power generated by an electric current, I, as it passes through some potential difference, ΔV:

$$P = I\Delta V \tag{1.43}$$

As we are interested in the amount of power per unit volume (Q, in units watts per metre cubed) at a particular point in 3D space, we use the differential form of Eq. 1.43. When differentiated with respect to volume, the current and potential difference become the current density, $\mathbf{j}$, and electric field, $\mathbf{E}$ respectively:

$$Q = \frac{dP}{dV} = \mathbf{j} \cdot \mathbf{E} \tag{1.44}$$

In the context of magnetosphere-ionosphere coupling, this energy initially comes from the solar wind as mechanical, but is converted to electromagnetic as it travels down field lines as Poynting flux. It includes both Joule heating and the amount of work done by $\mathbf{j} \times \mathbf{B}$ forces on the thermosphere. In the ionosphere, the Hall current (perpendicular to $\mathbf{E}$) does not dissipate, and the electric field aligned with the magnetic field is small (Lu et al., 1995). Thus, we may replace $\mathbf{j}$ with $\mathbf{j}_\perp$, which is in the direction of the Pedersen current (parallel to $\mathbf{E}$). In the reference frame of the neutral background that corotates with Earth, the total ionospheric electric field is the sum of the convection electric field ($\mathbf{E_c}$) and neutral wind dynamo electric field ($\mathbf{u} \times \mathbf{B}$), which is Joule heating:

$$Q_j = \mathbf{j}_\perp \cdot \mathbf{E} = (\sigma_P \cdot \mathbf{E}) \cdot \mathbf{E} = \sigma_P \left(\mathbf{E_c} + \mathbf{u} \times \mathbf{B}\right)^2 \tag{1.45}$$

where $\mathbf{B}$ is the terrestrial magnetic field, and σ_P is the Pedersen conductivity, i.e. the conductivity component perpendicular $\mathbf{B}$ and parallel to $\mathbf{E}$. In its expanded form, and assuming $\mathbf{E_c}$, $\mathbf{u}$ and $\mathbf{B}$ remain constant over the altitude range considered, the height integrated Joule heating rate (ΣQ_j) is written as (e.g. from Baker et al. (2004)):

$$\Sigma Q_j = \underbrace{\Sigma_P E_c^2}_{Q_c} + \underbrace{\overbrace{2\Sigma_P \mathbf{E_c} \cdot (\mathbf{u} \times \mathbf{B})}^{Q_{w1}} + \overbrace{\Sigma_P \left(\mathbf{u} \times \mathbf{B}\right)^2}^{Q_{w2}}}_{Q_w} \tag{1.46}$$

where Σ_P is the height integrated Pedersen conductivity. The term Q_c is known as the convection heating, and is simply the amount of Joule heating generated by the high latitude plasma convection via friction against a stationary neutral background. This term will be enhanced when the ionosphere is geomagnetically active (which is analogous to stronger $\mathbf{E_c}$), or when Σ_P is high due to solar EUV irradiance and particle precipitation. The terms encompassed by Q_w are the modification made to Q_c to account for the neutral wind dynamo, and are collectively known as the wind correction. Q_{w1} takes into account the difference between the plasma and neutral velocity, being negative if they flow in the same direction and positive when they oppose (effectively being a measure of the momentum exchanged upon collisions between the two). Q_{w2} is the neutral wind heating on a stationary plasma background. It should immediately be clear that the complex interaction between the plasma and neutrals described in the prior section can (and as Chapters 3 and 5 will show, does) drastically complicate Joule heating in the ionosphere.

Although it was recognised as important (Cole, 1962), Joule heating was not initially parameterised in global thermospheric models (e.g. Kohl and King (1967); Jacchia (1965)) due to the lack of data coverage for the high latitude electric fields, and even fewer measurements of the high latitude neutral wind. Early estimations of global Joule heating rates thus relied on indirect measurements, such as ground based magnetometers to infer the electric field from mean currents (Roble and Matsushita, 1975) or numerical models (Fuller-Rowell and Rees, 1980). As more direct electric field measurements started to become readily available, so did the study into the morphology of Joule heating statistically. Foster et al. (1983) for instance used AE-C satellite data to determine the first data driven statistical patterns of $\Sigma_P E_c^2$ (i.e. Q_c in equation 1.46), and was able to bin into seasonal and geomagnetic activity based ranges, illustrating the importance of both in modifying the conductivity and convection electric field magnitudes. Heelis and Coley (1988) created patterns with a slightly higher spatial resolution using DE2 satellite data, but focused more on discussing where in local time the Joule heating enhancements were; for instance, where E_c^2 is usually high in the convection return flow regions and where Σ_P is high in the vicinity of the auroral oval.

Perhaps the most significant modifier of the convection electric field, and in turn Joule heating, had until this point been left out of Joule heating statistics, that being the orientation of the IMF, which heavily dictates the local time and latitude of where both dayside and tail magnetospheric reconnection maps to in the ionosphere. This was included following the development of a new convection model by Heppner and Maynard (1987), and those succeeding that utilised the ever increasing data availability (such as that provided by SuperDARN) and improved modelling techniques (e.g Weimer (1995); Ruohoniemi and Greenwald (1996)).

These older studies assumed a negligible neutral wind, mainly because of limited

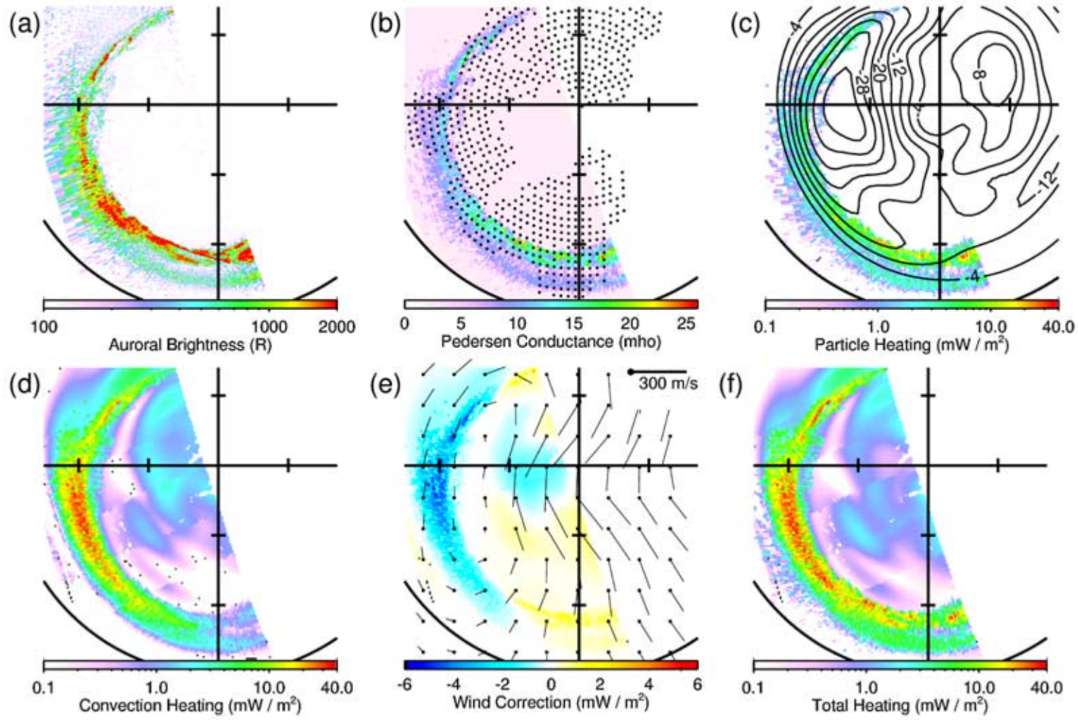

FIGURE 1.16: Joule heating components and parameters from Baker et al. (2004). (a: Auroral brightness measured by GUVI; (b) Σ_P derived from GUVI measurements; (c) Particle heating rate (Q_p) and SuperDARN electric potential contours; (d) Convection heating (Q_c); (e) Wind correction (Q_w) with overlain HWM14 neutral wind vectors; (f) Total heating ($Q_c + Q_w + Q_p$). Note that the total Joule heating rate (Q_j) does not include Q_p.

data availability showing it to be slower than the plasma. Neutral wind models of the high latitude thermosphere however had improved significantly since only representing the broad day-night pressure gradients (e.g. Jacchia (1965)). Now, they showed the neutrals significant (and sometimes large) velocity component due to ion-drag. Global circulation models such as TIEGCM, and empirical models, like HWM93, have both been used in addition to E_c and Σ_P models to calculate total Joule heating rates (e.g. Zhang et al. (2005) and Huang et al. (2012)), and have shown that the neutrals can be very important in modifying the Joule heating morphology and magnitude - effectively becoming a measure of how “out-of-sync” the thermosphere and ionosphere are. Variability in the amount of particle precipitation has also been shown to significantly enhance the Pedersen conductivity much more than models used in statistical studies suggest (e.g. Vickrey et al. (1981)).

Figure 1.16 is from Baker et al. (2004) and shows how changes in the convection electric field, Pedersen conductivity and neutral winds all propagate into the total Joule heating rate ($Q_c + Q_w$) for single event. Q_c (d) is high where the electric potential gradient in (c) is greatest, and where the Pedersen conductivity due to precipitation (b) is enhanced. Q_w (e) is more complicated, causing a large reduction in heating on the duskside and near the pole where the neutrals and plasma flow together strongly in the same direction. Even though the total heating shown in (f) includes particle heating, which is not discussed here, the influence of the wind correction and Pedersen conductivity terms can still be seen. When we consider however that the neutrals will be delayed in fully responding to changes in ion-drag, dependent on the ion-neutral collision frequency and other forces affecting them (see section 1.3.4), calculating Joule heating accurately is not straightforward when using any kind of model.

1.5 Summary

To summarise, a brief introduction to the remaining content of this thesis has been presented in this chapter. This includes basic physics behind the solar wind plasma, its interaction with Earth's magnetic field, and its dynamics in the context of single particles and as a particle collection. In addition, Earth's high latitude thermosphere-ionosphere system has been described, with special consideration given to how they are coupled and how they impart energy to one another.

The background provided here, especially that on thermosphere-ionosphere coupling, is an important motivation for the three scientific projects presented in Chapters 3, 4 and 5, and answers the questions:

- How does Joule heating vary on a global, statistical scale when the neutral winds are considered?
- How long does it take for the thermosphere to respond to a change in forcing from the ionospheric plasma, and is there any variation spatially?
- When thermospheric response timescales vary, how is Joule heating affected?

Chapter 2

Data & Instrumentation

This chapter discusses the instrumentation used within this thesis. A general overview of their operation will be given, as well as the post-processing of raw data performed to get the desired products. Table A1 contains a summary of these instruments, as well as the primary parameters that will be discussed. In addition to these, the interplanetary magnetic field B_y and B_z components, as well as the geomagnetic ap index, were obtained from the OMNI-web service provided by NASA. The Horizontal Wind Model 14 (HWM14; Drob et al. (2015)), which was utilised in chapter 3, is also described briefly.

Table 2.1: The main intruments utilised in this thesis, along with their primary data products.

Instrument	**Parameter derived**
SuperDARN	Ionospheric plasma E×B velocity
SCANDI	Thermospheric horizontal neutral wind velocity
Svalcam	630 nm auroral intensity
ESR	Electron density height profiles

2.1 SuperDARN

The Super Dual Auroral Radar Network (SuperDARN) consists of 36 high frequency (HF) radars (23 in the northern and 13 in the Southern hemisphere) which probe the E and F regions of the ionosphere (Greenwald et al., 1995a). Its primary objective is

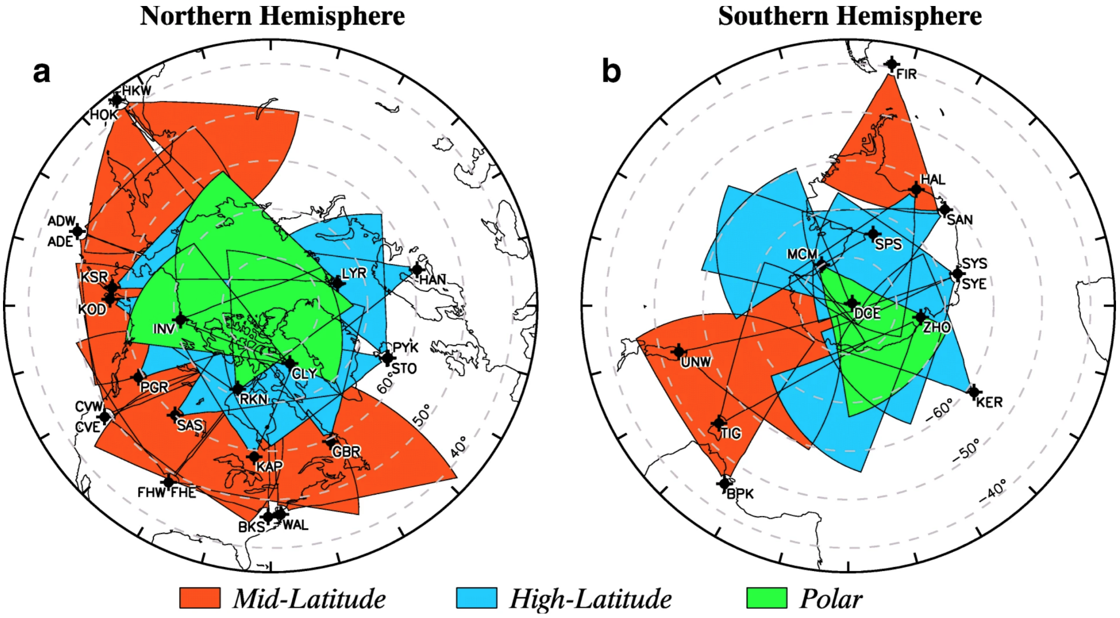

FIGURE 2.1: Fields of view of the SuperDARN network as of 2019 from Nishitani et al. (2019). Three letter site codes at the origin of each radars field-of-view are presented in a table, with their respective names, host institutions and locations, in Appendix A.1.

to combine data from all operating radars to measure the global morphology of the high latitude plasma convection, which has led to numerous scientific advances since its inception in 1993 (Chisham et al., 2007; Nishitani et al., 2019). The current state of the network's coverage as of 2019 is shown in Figure 2.1, and a full list of radars along with their respective site codes and positions can be found in Appendix A.1.

2.1.1 Coherent Radar Scatter

All SuperDARN radars work on the principle of coherent radar scatter. That is, an HF beam projected into the ionosphere that is scattered from magnetic field aligned plasma irregularities and received back at the radar. The received signal can then be used to determine a variety of parameters such as backscattered power, line of sight (LOS) Doppler velocity of the plasma and spectral width. The irregularities consist of strong electron density gradients travelling at E×B velocity, and most commonly are the result of the gradient drift instability in the E and F-regions of the ionosphere (e.g. Ossakow and Chaturvedi (1979)).

In order for HF waves to scatter from F-region irregularities and return back along the beam path (for a monostatic radar such as those used by SuperDARN), they need to achieve orthogonality to the magnetic field such that Bragg scattering can occur (explained in more detail later on). This is harder to achieve at high latitudes compared to middle-low latitudes, as the field is nearly vertical. To do this, a single SuperDARN radar will send out multiple beams in different directions and at certain elevation angles which are gradually refracted by the ionosphere into a horizontal path. The amount of refraction is determined by the frequency of the transmitted wave (f) and electron density (n_e), and is described by the Appleton-Hartree equation for the ionospheric refractive index (n) in its simplified form, neglecting the magnetic field contribution (as it is several orders of magnitude smaller than the electron density term; Maslin (2017)):

$$n^2 = 1 - \left(\frac{2\pi \sqrt{\frac{n_e e^2}{m\epsilon_0}}}{f^2} \right) \tag{2.1}$$

where e and m are the charge and mass of an electron respectively. In theory, if perfect information about the ionospheric composition is known, beam frequencies can be selected such that they are bent just enough to be orthogonal to the magnetic field in the irregularity region of choice. Hence, there have been numerous efforts to improve “ray tracing” techniques over the years (e.g. Coleman (1998); Ponomarenko et al. (2009)). The adaptive frequency capabilities of the SuperDARN radars (usually within the range of 10-14 MHz) mean that predictable changes to ionospheric density (such as day/night differences) can be accounted for, or to just simply sample different distances by anticipating the amount HF refraction and changing the frequency (and thus n in Eq. 2.1) accordingly.

Different take-off elevation angles of the transmitted waves can also lead to different modes of ionospheric propagation, which is illustrated in Figure 2.2 (from the ray tracing carried out by de Larquier et al. (2013), using an International Reference Ionosphere (IRI) model ionosphere). Steep rays can penetrate through the entirety of the ionosphere without being refracted, whilst certain rays are at just the right take-off angle such that they become orthogonal (black coloured region) within about 700 km range. These can occur at a wide variety of E and F-region altitudes (discussed in more detail in section

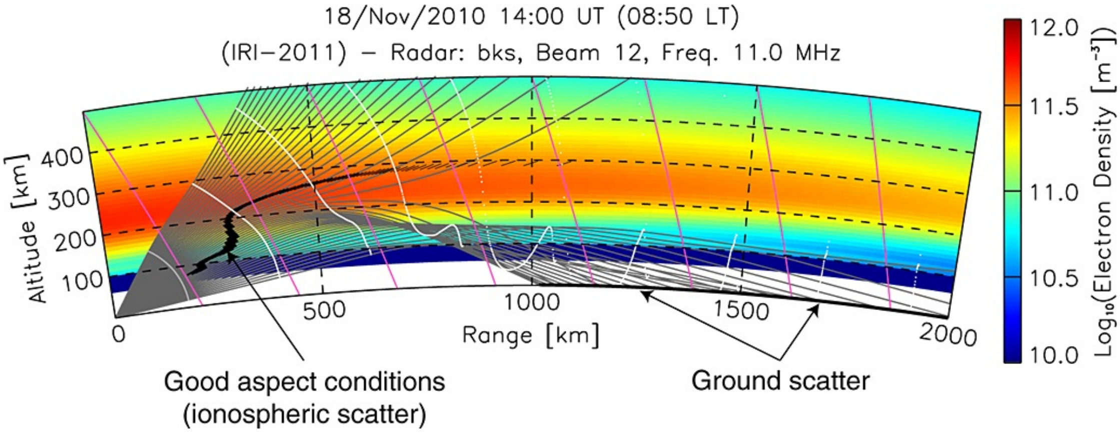

FIGURE 2.2: Ray tracing on the Blackstone SuperDARN radar, beam 12, at 11 MHz from de Larquier et al. (2013). The colour scale is electron density from the IRI. The black segments indicate where the rays are within 1° of orthogonality to the magnetic field (pink lines), where ionospheric backscatter is expected to occur.

2.1.2) and are known as "$\frac{1}{2}$-hop" scatter. They are known as such because rays may also be reflected towards the ground, which can subsequently reflect back up to the ionosphere at longer ranges (undergoing $1\frac{1}{2}$-hop, $2\frac{1}{2}$-hop, etc. ionospheric scatter) or return to the radar straight away via the same ray path (1-hop ground scatter). This means that very long ranges can be sampled by a single radar, but also that filtering out of ground scatter is required.

The process by which HF waves are scattered by the ionosphere enough to form a detectable echo is essentially a form of Bragg scattering. For waves of wavelength λ incident on a scattering volume at an angle θ, Bragg's condition states that constructive interference will occur when:

$$2d \sin\theta = n\lambda \tag{2.2}$$

where d is the interplanar distance and n is the number of ds separating each waves scatter point. If we apply this to an ionospheric irregularity, set $\theta = 90°$ for orthogonality and d to the irregularity width (n=1), then:

$$2d = \lambda \tag{2.3}$$

This means the wavelength of the transmitted wave must be double the irregularity width in order to receive strong backscatter at the radar. Varying the wave frequency

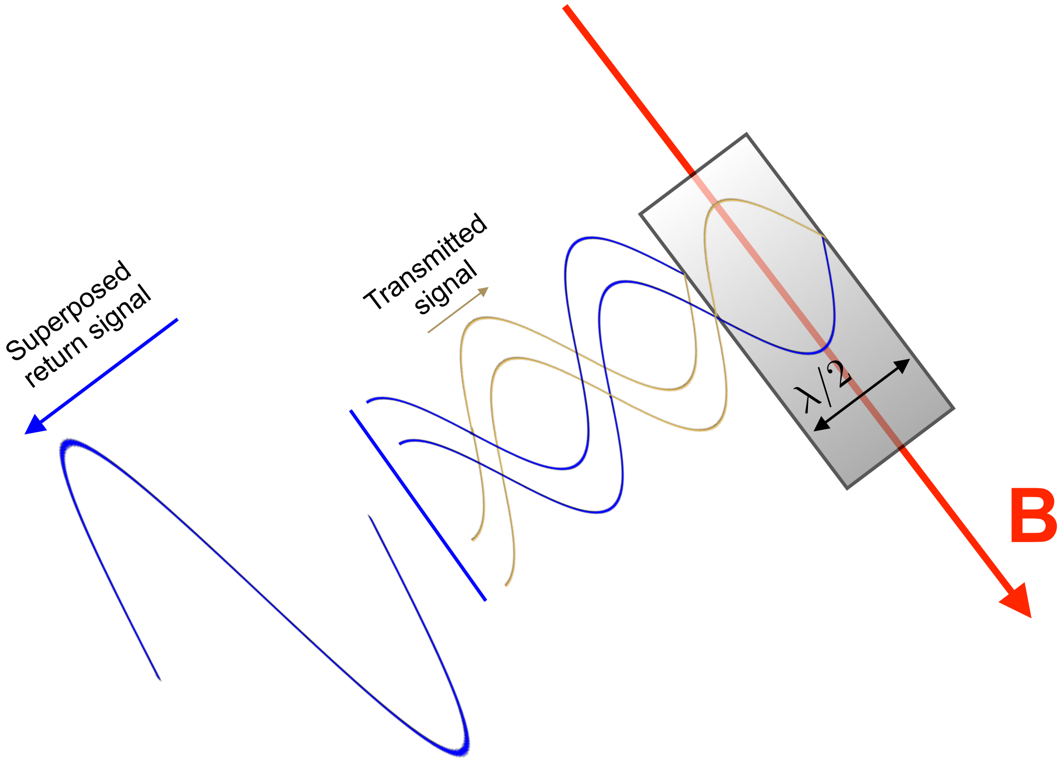

FIGURE 2.3: A diagram showing the Bragg scattering mechanism for two rays of transmitted signal (yellow waves). The return signals (blue) are in phase because the field-aligned irregularity is half a wavelength is width, and so constructively interfere to form a easily detectable signal.

thus allows observation of varying irregularity sizes. A schematic diagram of this type of scattering is shown in Figure 2.3, where the transmitted wave from the radar (yellow) hits orthogonally to a field aligned irregularity (shaded region) of width $d = \lambda/2$. The reflected waves from both boundaries (blue) are in phase, and thus constructively interfere to form a strong return signal along the original beam path, which is detectable. For this to work, the irregularities must stay coherent for a period long enough for the transmitted wave to reflect orthogonally at both boundaries. Assuming the waves travel at the speed of light, and the operating frequency is between 10-14 MHz, then:

$$\begin{aligned}\lambda = \frac{c}{f} = \frac{3\times10^8}{10 \text{ to } 14\,\mathrm{MHz}} &= 21.4 \text{ to } 30\,\mathrm{m} \\ \text{Irregularity size} = \frac{\lambda}{2} &= 10.7 \text{ to } 15\,\mathrm{m} \qquad (2.4)\end{aligned}$$

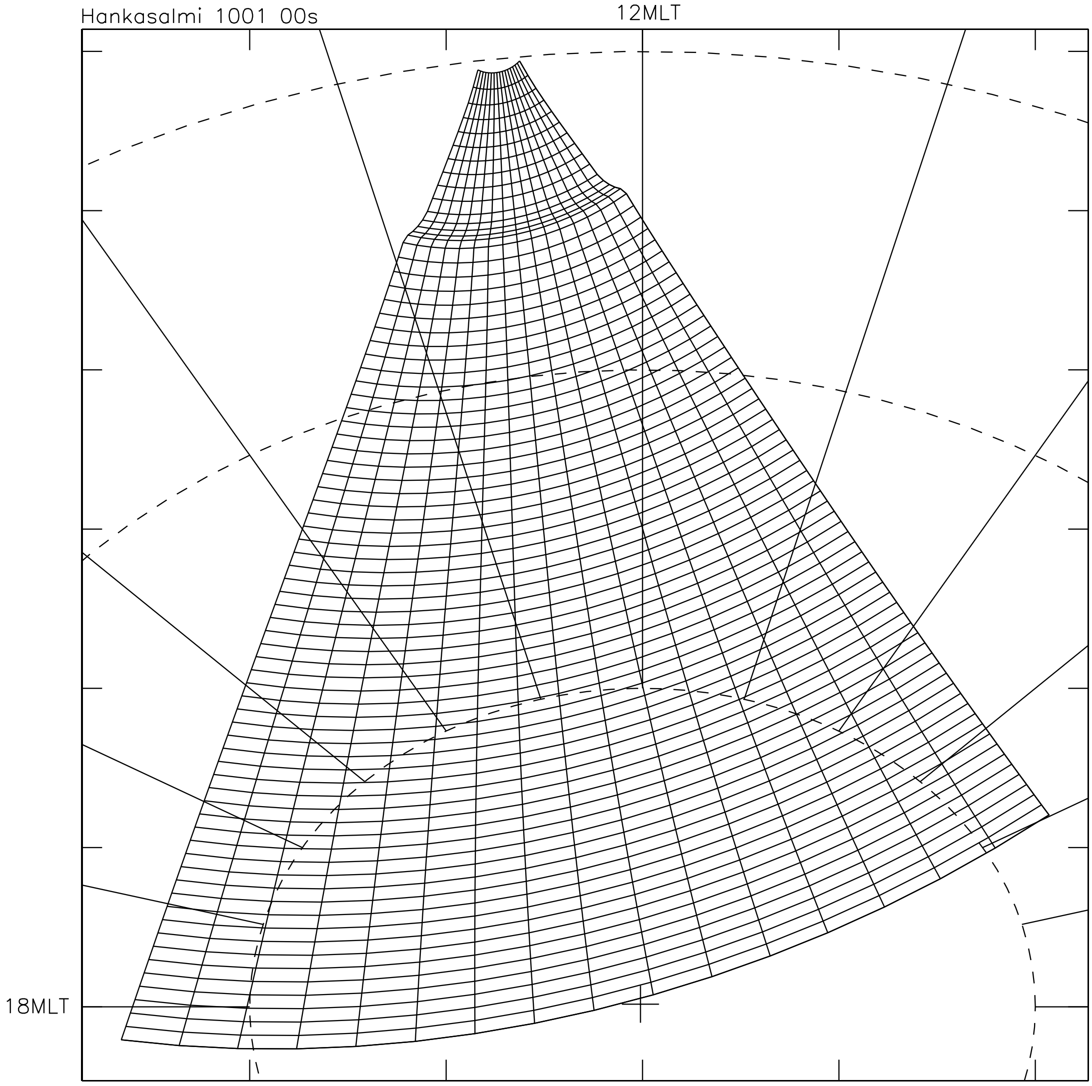

FIGURE 2.4: Example beam/range gate layout of the Hankasalmi SuperDARN radar. Coordinates are in MLAT-MLT format, with concentric circles separated by 10°.

and so the time the irregularity is required to be coherent is:

$$t = \frac{10.7 \text{ to } 15\,\text{m}}{c} = 36 \text{ to } 50\,\text{ns} \qquad (2.5)$$

which is quite short, and not unreasonable.

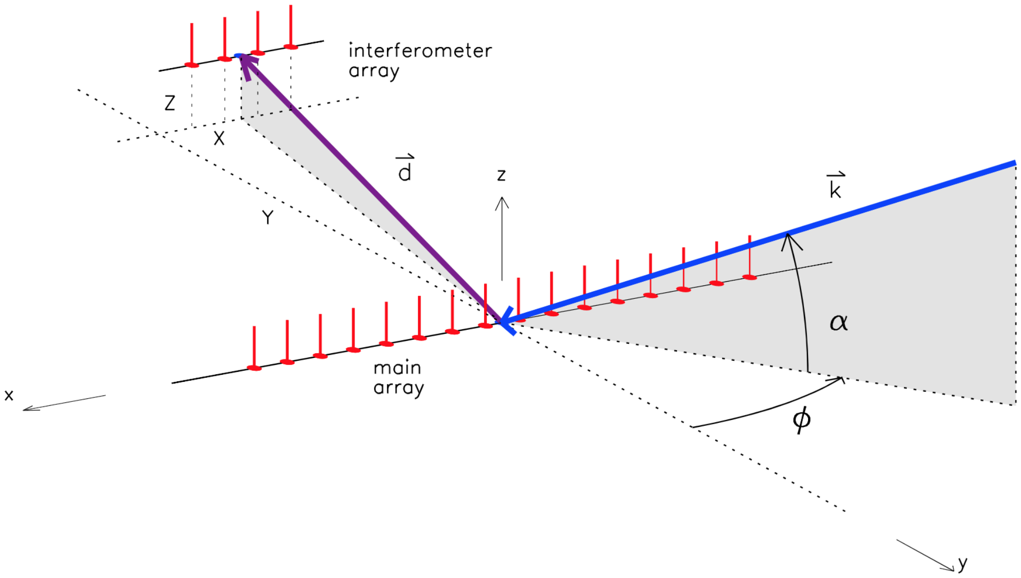

FIGURE 2.5: Typical layout of a SuperDARN radar. Antennas are denoted by red dots and vertical lines. The interferometer array is offset from the main array by position vector d. From Shepherd (2017).

2.1.2 Radar Operation

Each radar in the SuperDARN network attempts to receive a backscattered signal from 16 longitudinally spaced beams (about 3° wide each, resulting in a ~50° wide fan) and 75 different ranges (due to the vertical spread of radiated beam power and determining range from a virtual height model such as Chisham et al. (2008)). Figure 2.4 shows the beam/range gate layout for the Hankasalmi radar, which employs this common 16/75 convention and extends around 3500 km from the radar site in Finland. The congested ranges near the 14th gates are the result of a sharp altitude change in backscatter, which can also be seen in the black shaded region of Figure 2.2 (at a range of around 300 km).

Radar sites typically have the layout shown in Figure 2.5. The front main array consists of 16, log-periodic antenna with may transmit and receive, whilst the back array contains 4 receive-only antenna. Electronically phasing the main array allows steering of the radar beam, which is typically done in 16 different azimuthal (ϕ) directions (shown in Figure 2.4). The purpose of the interferometer array is to determine the angle of arrival (α) of the backscattered signal (from the phase difference between itself and the main array), which is then used to calculate range and altitude of the target region.

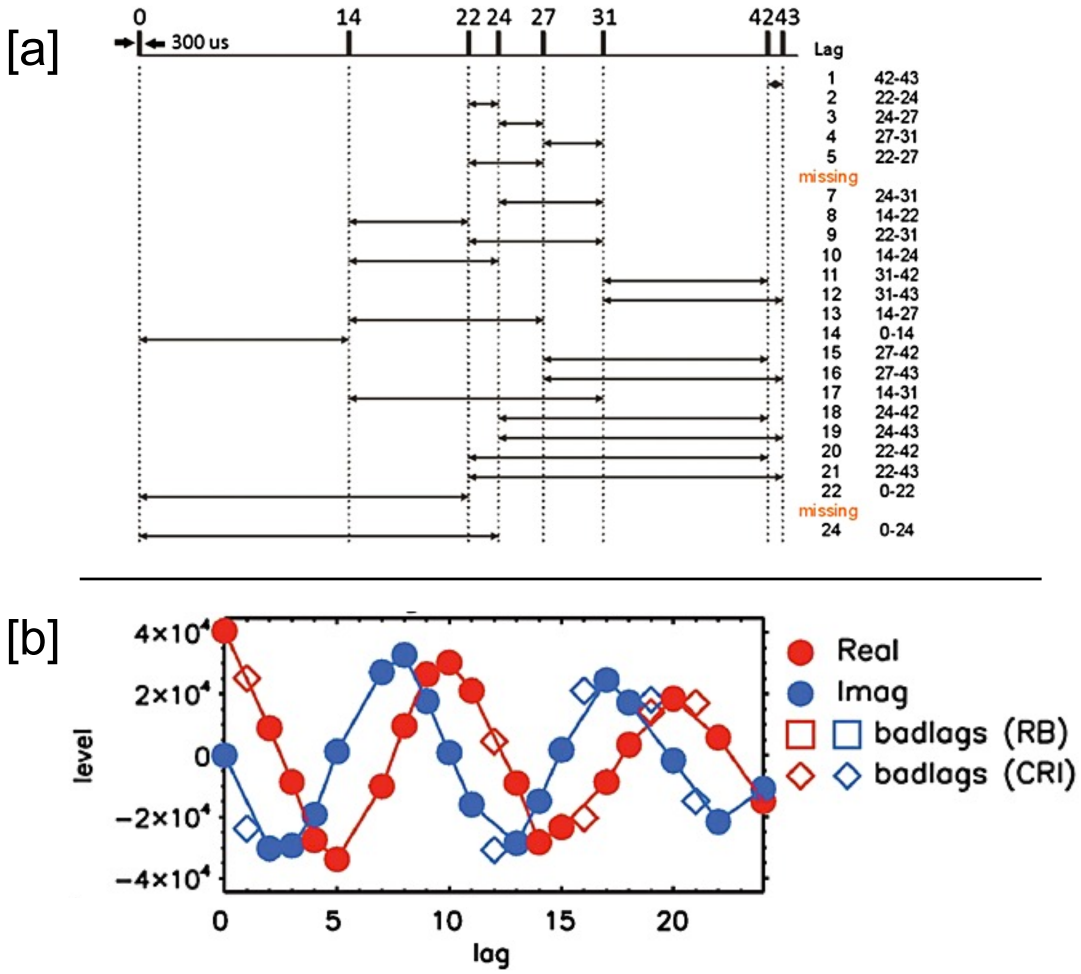

FIGURE 2.6: [a]: Sample 8-pulse, 23 lag sequence. The pulse length is 300 μs and the horizontal axis at the top is the number of lag time periods. [b]: ACF from beam 7, range gate 27 of the Fort Hays West SuperDARN radar on 2011/09/10. Bad lags are generally defined as those which either were affected by transmit-recieve overlaps (RB), or interference from scattering in multiple different regions returning at the same time (CRI). Both plots from Ribeiro et al. (2013).

The primary goal of each radar is to measure the E×B velocity of the scattering volume along the LOS of the beam. To do this, the Doppler shift of the backscattered signals needs to be determined. A multi-pulse sequence is used with an uneven time spacing such that several unique “lags” are formed between pairs of pulses. This is so as to minimise return signals being detected at the same time (range aliasing). Once the backscattered signals are sampled from those pulses and the differences found, a complex autocorrelation function (ACF) can be determined at each range gate and lag (which is averaged over several sequences to remove un-correlated signals, for around

7 s of integration). Figure 2.6a shows an example of an 8-pulse sequence that gives 23 unique lags including zeroth, producing the example ACF shown in b. These are the real (R: in phase) and imaginary (I: 90° out of phase) amplitudes, which decay with lag as the plasma being sampled becomes less correlated with itself.

To determine the Doppler velocity, spectral width and backscattered power of the ACF, a fitting software known as FITACF (heavily developed since its original creation, currently version 3.0 as of 2019) is run on the data from each radar. A linear fit to the ACF phase angle ($\tan^{-1}(I/R)$) gives the doppler velocity, and a Lorentzian fit to the ACF amplitude provides estimates for the spectral width and backscattered power (effectively modelling the de-correlation of amplitude with increasing lag). This assumes the shape of the Doppler spectrum (Fourier transformed ACF) is Lorentzian in nature, which has been shown to be most common (Hanuise et al., 1993). Ground scatter from integer-hop return signals can be identified due to very low LOS velocities, a narrow spectral width, and high power. They are then filtered out as appropriate.

2.1.3 High Latitude Convection Mapping

After each radar in the SuperDARN measures LOS plasma velocities with their respective fields of view, a key goal of the network is now able to be realised. That is, to form a picture of the high latitude convection pattern described in section 1.3.3. This is done using a collection of software cross-maintained by the SuperDARN community known as the Radar Software Toolkit (RST: SuperDARN Data Analysis Working Group. Thomas et al. (2018)).

The first obstacle is obtaining the full horizontal plasma vectors. In theory, pairs of radars whose FOV share a common volume can do this if they obtain backscatter from the same region via a merging algorithm (e.g. Greenwald et al. (1995b)). In reality however, this is unsuitable most of the time for global scale studies because it requires overlapping measurements in many, relatively small regions, to be useful. The solution currently employed is to find a form of the electric potential, Φ, which best fits all the LOS velocities measured by SuperDARN radars. This assumes that Φ is related to electric field, **E**, and convection velocity, **v**, by the **E** × **B** drift relation:

$$\begin{aligned}\mathbf{E} &= -\nabla\Phi \\ \mathbf{v} &= \frac{\mathbf{E}\times\mathbf{B}}{B^2}\end{aligned} \tag{2.6}$$

To begin the mapping process, LOS velocities from all available radars are mapped onto an equal area MLAT-MLON grid in AACGM coordinates (Shepherd, 2014). This is done by preforming a spatial and temporal boxcar filtering (taking into account radar scans before and after the scan of interest, as well as cells surrounding the target cell) with heavier weightings for data acquired within the cells themselves (Ruohoniemi and Baker, 1998). The gridded velocities are then translated to an MLAT-MLT grid, and overlapping vectors are merged using a least-squares linear regression akin to the merge technique by Cerisier and Senior (1994). For the potential to be fitted, a latitude where at least 3 LOS velocity vectors over $100\,\mathrm{ms}^{-1}$ lie is found in software, and a circular region is defined known as the Heppner-Maynard boundary (HMB) (Heppner and Maynard, 1987; Shepherd and Ruohoniemi, 2000). Here, the electric potential is assumed to be zero, and can be thought of as the limit of the convection pattern. Vectors which then happen to sit below the HMB are discarded.

The electric potential is then determined by the gridded LOS velocities and HMB using the “map-potential” technique described by Ruohoniemi and Baker (1998). The argument being that even though true horizontal vectors probably cannot be determined due to spatial/backscatter coverage in most regions, the LOS velocities act to constrain the possible large scale convection pattern morphologies. Indeed, map-potential has at least been shown to be much more successful than alternative techniques such as “beam-swinging” (Provan et al., 2002). The potential, Φ, is expressed in terms of spherical harmonic functions, magnetic co-latitude (θ) and local time (ϕ) (e.g. Chisham et al. (2007)):

$$\Phi(\theta,\phi) = \sum_{l=0}^{L}\sum_{m=0}^{Min(l,M)} (A_{lm}\cos m\phi + B_{lm}\sin m\phi)P_l^m(\cos\theta) \tag{2.7}$$

where P_l^m are the Legendre polynomials, l and m are the order and degree of the expansion respectively (L and M are maximums), and A_{lm} and B_{lm} are complex coefficients

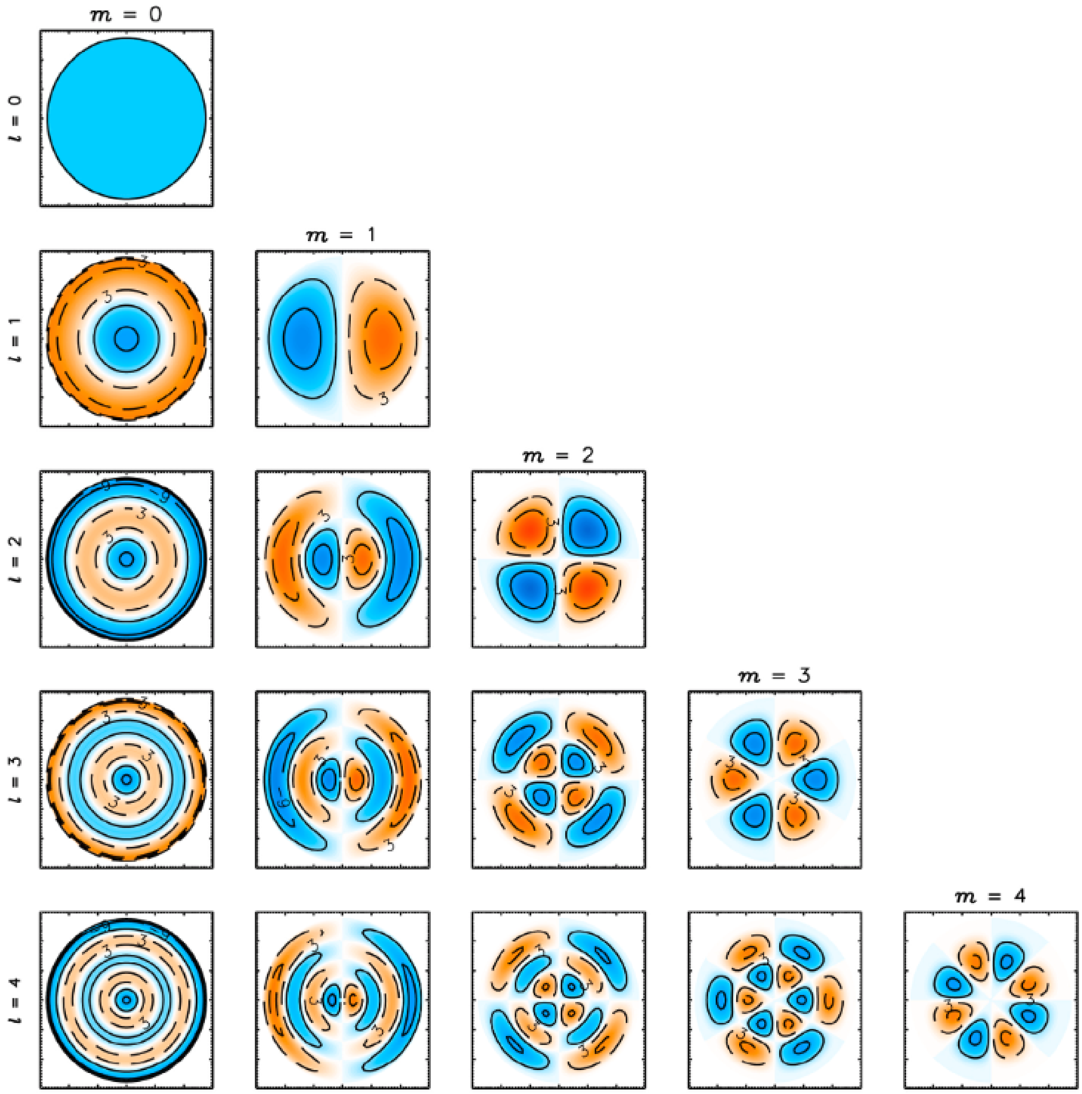

Figure 2.7: Basis functions associated with varying degrees of order (l) and degree (m) for the spherical harmonic expansion shown in Eq. 2.7. Figure taken from Grocott et al. (2012).

with dimensions $l \times m$. The values of both l and m determine the global scale characteristics of the fit, with higher orders able to resolve much smaller scale convection structures. Figure 2.7 shows the basis functions of this fit from Grocott et al. (2012), with an arbitrary latitude scale and varying values of l and m up to 4. Note that the standard, two cell convection pattern originates only within the first few orders/degrees, particularly $l = m = 1$. Depending on the scientific objectives, 6th order fits are generally sufficient for global scale convection studies without over-fitting. This is the order of fit used throughout chapters 3, 4 and 5 in this thesis.

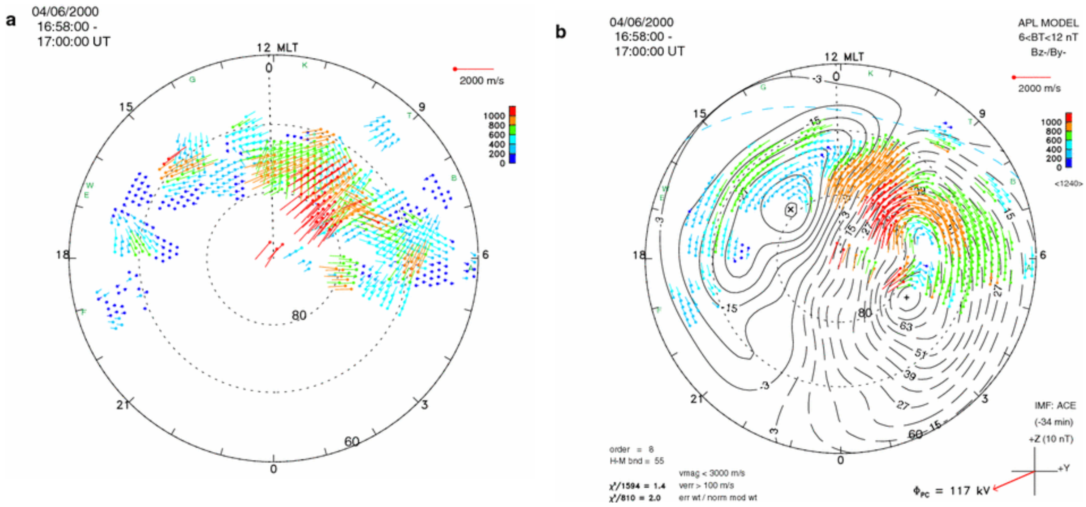

FIGURE 2.8: [a] Example gridded LOS velocities from radars in the SuperDARN network. [b] Fitted vectors and the electric potential spherical harmonic expansion contours to the data in [a]. Both taken from Chisham et al. (2007).

Figure 2.8 shows an example of the map-potential technique applied to real LOS velocity data, taken from Chisham et al. (2007). Figure 2.8a shows all the LOS vectors mapped onto the MLAT-MLT coordinate system, which then go on to be combined in the gridding process. Figure 2.8b shows fitted vectors in each bin where data was present, along with the global contours of electric potential derived using the expansion shown in Eq. 2.7. The blue dashed line shows the software determined HMB for this interval.

It should be noted however that even though the coverage of SuperDARN is large (and has grown significantly since the date shown in Figure 2.8), there are still often gaps in coverage such as that seen on the nightside in Figure 2.8. To ensure that the global fit is constrained in these regions to reasonable estimates, a statistical model often supplements velocity vectors at a lower weightings that those measured by the radars. There have been several of these models over the years with varying degrees of data coverage (e.g. Ruohoniemi and Greenwald (1996, 2005); Cousins and Shepherd (2010)), and are typically parameterised by the IMF B_z and B_y components (e.g. Figure 1.14).

Recall that in the ionospheric E-region, collisions between the plasma and neutrals occur much more often per gyro-rotation than in the F-region. The convection patterns shown in 1.14, as well as those produced by other studies and models, are thus assumed to be of the F-region $\mathbf{E} \times \mathbf{B}$ drifting plasma that is mostly unperturbed by collisions.

Identifying E-region plasma drift measurements from F-region so as not to "contaminate" generated convection patterns is thus an important consideration for high latitude ionospheric research (Chisham and Pinnock, 2002).

For chapter 3 of this thesis, we employ the Ruohoniemi and Greenwald (1996) model, which is best used with the high latitude data of that study. For chapters 4 and 5 however, the Thomas and Shepherd (2018) model is used, which includes data from the somewhat recent mid-latitude expansion of the SuperDARN network.

2.2 SCANDI

SCANDI is a special type of Fabry-Perot Interferometer (FPI) located on Svalbard that can spatially resolve horizontal neutral wind vectors within its FOV, which is displayed in Figure 2.9 in comparison to the two overlapping SuperDARN radars. The techniques used to determine these allow for mesoscale neutral wind structures to be observed within the designated sectors (zones) displayed, offering a resolution only slightly coarser than SuperDARN (at around 100 km). Since 2007, SCANDI has been stationed at the Kjell Henriksen Observatory (KHO) in Longyearbyen, a latitude allowing dayside observations during the polar night, and of the cusp. A comprehensive description on the operation of SCANDI can be found in Ronksley (2016) and Aruliah et al. (2010).

2.2.1 Instrument Operation

SCANDI (Aruliah et al., 2010) is based on a non-traditional FPI design by Conde and Smith (1997), which has since become known as a Scanning Doppler Imager (SDI). Both SDIs and FPIs however work using the same underlying physics, that is, they both aim to measure the Doppler shifts of auroral and airglow emissions. FPIs have a long history within studies of the thermosphere (e.g. Babcock (1923); Hays and Roble (1971)), as they are sensitive enough to detect both weak green (557.7 nm) and red (630 nm) line emissions. Only 630 nm SCANDI data was used in this thesis for chapters 4 and 5.

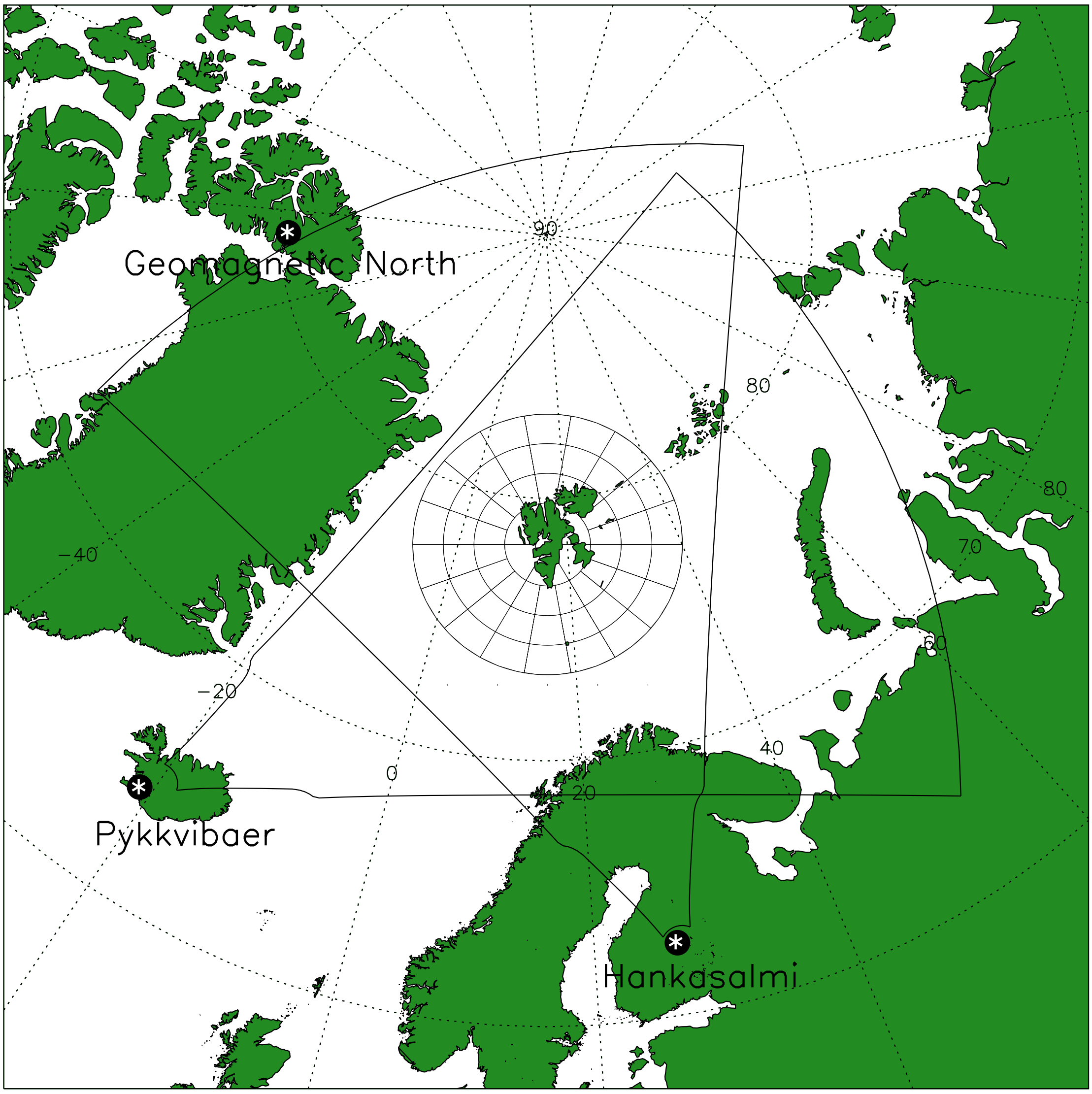

FIGURE 2.9: The location of the SCANDI FOV using a 61 zone setup. Also shown are the FOV's of the two overlapping SuperDARN radars.

The schematic layout of a basic FPI is shown in Figure 2.10. An etalon, comprising two close and partially reflective (silvered) mirrors, accepts incident light which is partially internally reflected multiple times. At each reflection on the furthest etalon wall, a fraction of light is refracted through and focused by a lens onto a screen (or CCD camera). The result is an interference pattern of concentric circles caused by in phase light rays (of different path lengths) constructively interfering. Therefore, for a mirror

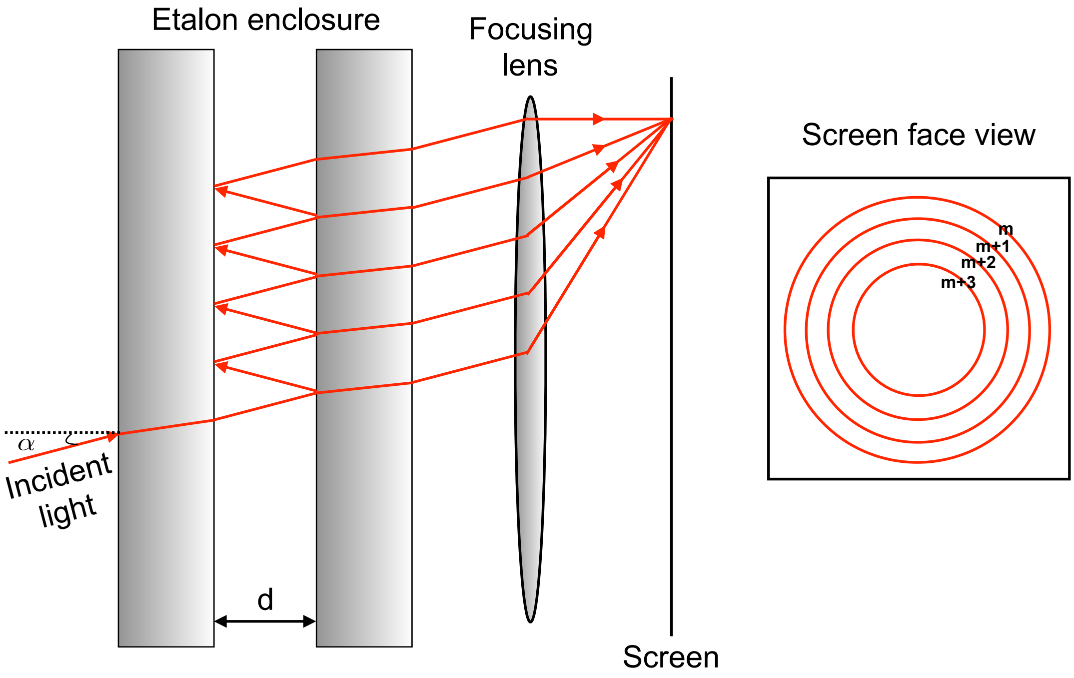

FIGURE 2.10: Simple diagram of a traditional FPI layout.

separation, d, and incident angle, α, light of wavelength λ will satisfy the condition:

$$2d\cos\alpha = m\lambda \tag{2.8}$$

where m is the order of constructive interference band. The path difference between superposing waves must therefore be $m\lambda$, for integer values of m.

Because λ has a $\cos\alpha$ dependence, and α is small such that $\tan\alpha \approx \alpha$, successive fringes are shifted in wavelength due to the focusing lens according to:

$$m\lambda = 2d\left(1 - \frac{R^2}{2f^2}\right) \tag{2.9}$$

where R is the radial distance of the fringe from the centre of the screen, and f is the focal length of the lens. The LOS velocity (v_{los}) is then given using the Doppler relation:

$$\frac{v_{los}}{c} = \frac{\Delta\lambda}{\lambda} \tag{2.10}$$

for a viewing angle of approximately 1° in a single look direction. Usually, the shift in fringe radius (and in turn, wavelength) is only a few pixels or less on the CCD, meaning FPIs can be subject to large errors.

The spectral resolving power (SRP) of the FPI is its ability to distinguish between circular bands caused by different wavelengths. SCANDI (and other FPIs) use the Taylor criterion to help define this, which states that wave maxima must be separated by at least the full-width-half-maximum (FWHM) to be resolvable. A minimum wavelength difference, $\Delta\lambda$, for consecutive fringes produced by two monochromatic sources (wavelength λ) can be derived (e.g. Juvells et al. (2006)):

$$\left|\frac{\lambda}{\Delta\lambda}\right| = \frac{\pi m r}{1 - r^2} \tag{2.11}$$

where r is the coefficient of reflection of the etalon mirror.

The difference between FPIs and SDIs (such as SCANDI) is that the latter can measure these emission spectra interference patterns at several different locations in the sky at once. The layout of SCANDI is shown in Figure 2.11. The fisheye lens points at a mirror which is rotated through several look directions (which is later used to determine the horizontal wind vector), ultimately resulting in a FOV of 140° which translates to an approximate 1000 km diameter at 250 km altitude (see Figure 2.9). Light pases through a collimator and filter wheel, which allows varying observations of either the red or green line emissions. Light from the collimator then is expanded to the diameter of the etalon (150 mm), which when projected onto the Electron Multiplying Charged Coupling Device (EMCCD) camera later produces interference bands up to $m + 4$, 5 orders in total. The etalon has a varying width, which means Doppler shifted wavelengths can be measured by comparing successive images with different values of etalon separation (known as the scanning functionality of the SDI). Doing this allows the interference pattern, which is a projection of the entire sky, to be split into different zones, each treated separately. Figure 2.12 shows an example of a 25 zone configuration from Aruliah et al. (2010), and it's relation to the SCANDI FOV. The number of zones is controlled by software, and dependent on the quality of detector and signal-to-noise ratio. For the studies presented in chapters 4 and 5, the 61 zone configuration shown in Figure 2.9 was used, giving an approximate 100 km resolution horizontally of LOS neutral wind velocity measurements

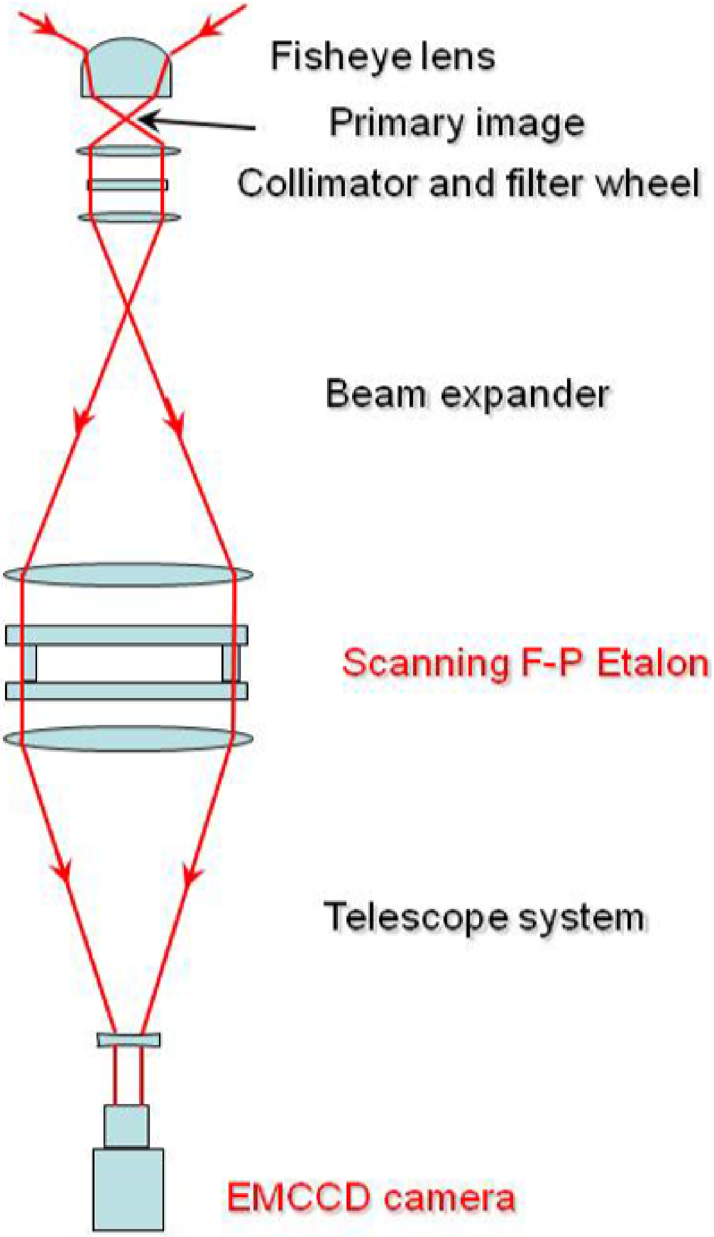

Figure 2.11: Layout of the SCANDI SDI located at KHO, Longyearbyen, Svalbard. Taken from (Aruliah et al., 2010).

at 250 km altitude. Multiple scans are taken in an integreation period of around 7 minutes.

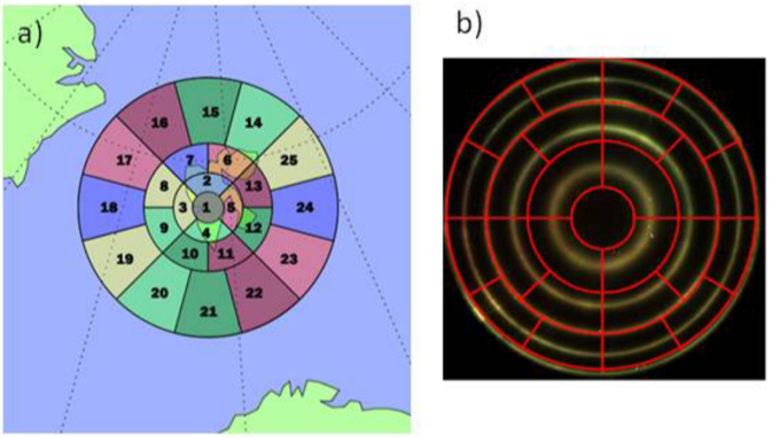

FIGURE 2.12: Example 25 zone configuration of SCANDI from Aruliah et al. (2010). [a]: FOV above Svalbard. [b]: Relation to the interference pattern imaged.

2.2.2 Neutral Wind Vector Determination

One major assumption that the SCANDI analysis software uses to turn LOS neutral wind velocity measurements into vectors, is that the vertical wind is constant across the FOV. This is probably untrue, as the horizontal scale size for the vertical wind is often shorter than the SCANDI FOV diameter (e.g. Anderson et al. (2011)). However, it is more acurate than assuming a zero vertical wind because that would induce errors from non-zero values, in addition to ambiguities accross the FOV. A second assumption made is that the vertical winds are small compared to the horizontal, which is often typically the case (10's ms^{-1} vs 100's ms^{-1}).

The exact algorithm used for vector determination was developed by Conde and Smith (1998), and is presented again here. Each zone sampled is part of an annulus shape, centred about the FOV zenith with a radius and respective zenith angle ϕ. Each annulus is divided into n sectors (such that the total number of sectors in each annulus equals the total number of SCANDI zones), with the kth sector corresponding to an azithimuthal angle of θ_k. The LOS velocity component can be written in terms of the uniform vertical wind (v_z), :

$$v_{los}(\theta_k, \phi) = v_z \cos\phi \tag{2.12}$$

which would be constant in all sectors within the same annulus. However, a similar argument can be said for a horizontal wind receeding at the same speed (ϵ) in all sectors of the same annulus:

$$v_{los}(\theta_k, \phi) = \epsilon \sin \phi \tag{2.13}$$

Therefore, in a single annulus, we may not determine if the flow measured by SCANDI is uniformly vertical, or diverging uniformly horizontally. However, in the centre sector for example where the LOS is directly along the zenith, we know the vertical wind is the sole contributor to v_{los}. So, again assuming vertical wind homogeneity across the FOV, v_z can be subtracted from the LOS measurements of each zone, leaving only the horizontal wind contributions to the LOS velocity:

$$v^H_{los}(\theta_k, \phi) = v_{los} - v_z \cos \phi \tag{2.14}$$

which is related to the horizontal wind vector ($\mathbf{U} = (U_x, U_y)$) by:

$$v^H_{los}(\theta_k, \phi) = \sin \phi \, (U_x \sin \theta_k + U_y \cos \theta_k) \tag{2.15}$$

Both the zonal (U_y) and meridional (U_y) wind fields can then be expanded as a Taylor series of first order in terms of zonal and meridional distance from the zenith (x and y respectively):

$$\begin{aligned} U_x &= u_0 + \frac{\delta u}{\delta x} x + \frac{\delta u}{\delta y} y \\ U_y &= v_0 + \frac{\delta v}{\delta x} x + \frac{\delta v}{\delta y} y \end{aligned} \tag{2.16}$$

Finally, these fitted components are resolved perpendicularly to the LOS of the sector, then combined with the actual LOS velocity measured by SCANDI in that zone. This gives a best estimate of the actual zonal and meridional neutral wind components in each zone.

2.3 EISCAT Svalbard Radar

Located just down the road from SCANDI, near Longyearbyen, lies an installation of the European Incoherent Scatter Scientific Association (EISCAT) known as the EISCAT

FIGURE 2.13: Left: ESR control hut and 32 m steerable dish. Right: 42 m field aligned dish. Photos: Daniel Billett

Svalbard radar (ESR) (Wannberg et al., 1997). Unlike the SuperDARN radars which use coherent scatter to measure the doppler velocity of E×B drifting plasma, ESR operates using the principles of incoherent scatter to measure height profiles of electron density. This is done separately on two monostatic dishes, one 32 m steerable and one 42 m static that is aligned parallel to the magnetic field. Both dishes and the control hut are shown in Figure 2.13, however only the 42 m field aligned dish was used in this thesis during chapter 5. The fundamental difference between incoherent and coherent scatter (besides the large differences in transmit frequency; VHF vs HF) is that incoherent scatter radars observe weak ion-acoustic structures in any direction, whilst coherent scatter radars observe structures only aligned with the magnetic field.

2.3.1 Incoherent Radar Scatter

EISCAT (Rishbeth and Williams, 1985) radars work on the principle of incoherent scatter. Instead of an HF beam like the SuperDARN radars, the EISCAT antenna can transmit anywhere in the VHF-UHF range (typically between 200 MHz and 1000 MHz depending on mode. ESR dishes usually transmit around 500 MHz). The reason for this is so the transmitted waves have negligible refraction in the ionosphere (according to eq.

2.1), and so essentially travel in a straight line with a very narrow field of view and short horizontal range. This does however mean that a large altitude range of the ionosphere can be sampled with a single beam.

The flagship parameter determined by the EISCAT radars is the ionospheric electron density. A technique using Thomson scattering was first proposed by Gordon (1958), which involved relating the electron density to the power of emitted waves from scattered electrons.

The power of the return signal as a result of Thomson scattering of electrons is extremely weak compared to the transmitted signal, thus requiring a very sensitive receiver with high gain. The radar equation giving the received power (P_r) for an electron target is:

$$P_r = \frac{\sigma P_t G_t A_r}{\left(4\pi R_i^2\right)\left(4\pi R_s^2\right)} \tag{2.17}$$

where P_t and G_t are the transmitted power and gain, R_i and R_s are the ranges to and from the scattering volume, A_r is the effective receiving antenna area (given by $\frac{G_t\lambda^2}{4\pi}$) and σ is the scattering cross-section of the electrons. Single electrons only have a scattering cross-section of around $1\times10^{-28}\,\mathrm{m}^2$ (Grydeland et al., 2004), which is why it is integrated over a scattering volume of around $10\,\mathrm{km}^3$ by selecting the appropriate gain and pulse length. Because both dishes at ESR are monostatic, $R_i = R_s = R$, which can be calculated to a high precision from many different altitudes where scattering occurs (due to time delays between the transmitted and received pulses). The simplified radar equation is thus:

$$P_r = \frac{\sigma P_t G_t^2 \lambda^2}{64\pi^3 R^4} \tag{2.18}$$

The scattering cross-section can be calculated from the backscattered signal power spectrum, which is directly related to the electron density. However, this process assumes the electrons are free. In reality, the electrostatic interaction between ions and electrons means this is not the case. After the first observations using the above method were made (Bowles, 1958), it was noticed that the power spectrum actually showed characteristics of measuring the bulk motions of ions instead of electrons. This was subsequently explained as the result of Debye shielding.

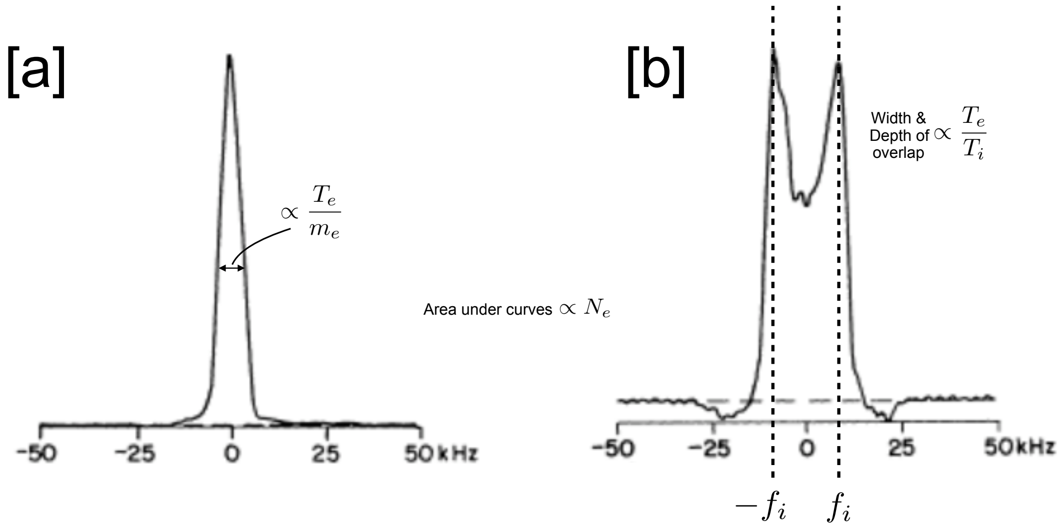

FIGURE 2.14: Examples of low E region (a) and F region (b) backscattered power spectrum from the Tromsø EISCAT radar, adapted from Rishbeth and Williams (1985).

The scale of the interactions between ions and electrons is called the Debye length, and given by:

$$\lambda_D = \left(\frac{\epsilon_0 k_B T_e}{N_e e^2} \right)^{\frac{1}{2}} \tag{2.19}$$

where ϵ_0 is the permittivity of free space, k_B is Boltzmann's constant, T_e is the electron temperature, N_e is the electron density and e is the elementary charge. As the wavelengths of the EISCAT radars are longer than λ_D, the scattering can not truly be Thomson-like. However, electrons undergo random thermal motion which induces ion and electron acoustic waves, emitting over a wide range of wavelengths. These waves cause modifications to the electron density, some parts of which will have a diameter equal to half the transmitted wavelength, satisfying the Bragg condition. Therefore, EISCAT backscatter is actually a form of coherent scatter, generated by incoherent scatter. Because both ion and electron accoustic waves drive these changes, parameters from both can be determined instead of from just the electrons.

2.3.2 Backscatter Spectrum Analysis

If fully incoherent Thomson scattering from electrons was actually occurring, a single hump power spectrum would be seen from the return signal such as in Figure 2.14a.

These can actually be observed in the low E region sometimes, where a low N_e results in a large Debye length. This spectrum is Doppler broadened due to the Maxwellian distribution of thermal electron speeds, and the FWHM is related to the electron temperature and composition by $\frac{T_e}{m_e}$. The total backscattered power, i.e. the area under the curve, is directly proportional to N_e as predicted. The centering of the spectra about the transmitter frequency (denoted here by a frequency of zero) describes the LOS speed of the backscatter volume according to the offset (Doppler shift). Thus Figure 2.14 shows a target that was stationary along the LOS.

In the F region, where the Debye length is basically always smaller than the transmitted wavelength, a spectrum such as that shown in Figure 2.14b is received instead. This is the result of thermal fluctuations in the ions, and results in two humps instead of one. These are actually two separate spectral distributions of ion-acoustic wave backscatter that overlap, with the amount they overlap related to the amount of Landau damping (Landau, 1946) occurring, controlled by the electron-ion temperature ratio $\left(\frac{T_e}{T_i}\right)$. One hump is centred at f_i, corresponding to waves travelling towards the radar, and one at -f_i corresponding to those travelling away.

2.4 Svalcam

Svalcam (Taguchi et al., 2012) is a typical all-sky camera, also located at KHO near Longyearbyen, Svalbard. It comprises of an EMCCD camera of pixel dimensions 512×512, and a narrow passband interference filter which rotates through three different wavelengths: 630 nm (red, ∼250 km), 557.7 nm (green, ∼150 km) and 572.5 nm (background). Only the 630 nm red line data is used in this thesis during chapter 4, to match the emission altitude of the airglow measured by SCANDI during those events. At 250 km altitude, the projected Svalcam FOV diameter spans roughly 50° of longitude at the latitude of Svalbard. 1 s and 4 s exposures are taken sequentially.

The Van Rhijn effect is an optical distortion that the all-sky camera data is susceptible to, due to using a fish-eye lens to obtain the wide FOV. Wavelengths measured at low elevation angles, near the edge of the 512×512 EMCCD, are artificially brightened because they are projected and superimposed onto a 2D image. This is corrected by using the method described by Kubota et al. (2001), where the measured intensity at a certain zenith angle θ ($I(\theta)$) is related to the true intensity by:

$$I(\theta) = \left[1 - \left(\frac{R_E}{R_E + h}\right) \sin\theta^2\right] I_{true}(\theta) \tag{2.20}$$

where R_E is the radius of Earth and h is the emission altitude.

2.5 OMNI Data Products

OMNI is a data set of several Earth and near-Earth geomagnetic parameters collated and maintained by the Space Physics Data Facility (SPDF) at NASA. The data extensively spans from 1963 to the current year, and can be downloaded freely from `http://omniweb.gsfc.nasa.gov/`. OMNI products of interest in this thesis are twofold: the IMF B_y and B_z components, and the geomagnetic ap index.

Over the years, a total of 11 near-Earth spacecraft have been used to determine the OMNI IMF values. Data availability for any one time is dependent on the spacecraft in operation at that moment, which is combined and averaged together onto different time integrations, but not until after time shifting each to the same dayside magnetopause location of 1 AU. Since 1983, averaged data is available on as low as a 1-minute cadence, which is what was used during the studies in this thesis. The bulk of the data as of 2019 is from the ACE, Wind and Geotail spacecrafts.

The ap index is a general measure of global geomagnetic activity. It is a linear version of the 3-hour Kp index, and is converted to using a standardised look-up table (Bartels and Veldkamp, 1949). The Kp index is measured using ground based magnetometer data from 13 sub-auroral stations across the Earth. At each station, the horizontal disturbance magnetic field is measured by subtracting a quiet day background, and then converted to the local quasi-logarithmic K-index (Bartels et al., 1939). It is then globally averaged with K-indicies from all other stations to determine Kp (from the German “planetarische kennziffer”, or planetary index). In the OMNI dataset, ap is provided by the Geo-Forschungs Zentrum (GFZ) Potsdam, Germany.

2.6 HWM14

The Horizontal Wind Model 2014 (HWM14; Drob et al. (2015)) is a climatological neutral wind model of the thermosphere to the base of the exosphere. Within HWM14, there are special considerations made to capture the winds at high latitudes that are affected by Dungey cycle plasma convection (known as a modular component, the Disturbance Wind Model, DWM, by Emmert et al. (2008)).

The formulation of the model includes data from numerous sources such as ground based Fabry-Perot interferometers, sounding rockets, incoherent scatter radars, lidars and satellites, spanning over 60 years of observations. Vector spherical harmonic functions are used to represent seasonal and diurnal variations in the wind, low-order polynomials constrain geomagnetic variations based on the ap index, and fluctuations in the horizontal wind with altitude are determined by cubic spline interpolation. Inputs to the model are thus universal time, day of year, geomagnetic ap index, altitude, and geographic latitude/longitude.

Chapter 3

Statistical Neutral Wind Contributions to Global Joule Heating Estimates

The following chapter contains published work from the article:

Billett, D. D., Grocott, A., Wild, J. A., Walach, M. T., & Kosch, M. J. (2018). Diurnal variations in global Joule heating morphology and magnitude due to neutral winds. *Journal of Geophysical Research: Space Physics*, 123(3), 2398-2411.

During this study, both AG and JAW acted as academic supervisors, whilst M-TW and MJK provided valuable discussion.

3.1 Introduction

The influence of the thermospheric neutrals on both where and how much Joule heating is enhanced and reduced was briefly mentioned in section 1.4. As Joule heating is ultimately the frictional heat generated upon neutral-ion collisions, one of the most important factors becomes the velocities of the colliding particles. The greatest momentum exchange, and in turn frictional work done, will usually occur when both the plasma and neutrals are travelling in opposite directions. However, there are thermospheric and ionospheric processes which vary diurnally, making the calculation of Joule heating even more difficult. In this chapter, the resultant effect of those diurnal variations on the morphology and magnitude of Joule heating are carefully examined for the high latitude northern hemisphere (polewards of 50° geomagnetic latitude (MLAT)). This was carried out in this study using measurements of the convection electric field by SuperDARN, estimates of the magnetic field from the IGRF model (Thébault et al., 2015), neutral winds from the HWM14 (Drob et al., 2015), and Pedersen conductivities from models set out by Hardy et al. (1987) and Rich et al. (1987).

As we recall, the total height integrated Joule heating rate over the entire ionosphere is given by:

$$\Sigma Q_j = \underbrace{\Sigma_P E^2}_{Q_c} + \underbrace{\overbrace{2\Sigma_P \mathbf{E}\cdot(\mathbf{u}\times\mathbf{B})}^{Q_{w1}} + \overbrace{\Sigma_P\,(\mathbf{u}\times\mathbf{B})^2}^{Q_{w2}}}_{Q_w} \tag{3.1}$$

where Σ_P is the height integrated Pedersen conductivity, $\mathbf{E}$ is the convection electric field, $\mathbf{u}$ is the neutral wind velocity vector and $\mathbf{B}$ the magnetic field. Q_c, known as the convection heating, is the work done by the convection plasma against a static neutral background. Q_w, the wind correction, is made up of the two terms which involve the neutral wind. Q_{w1} is the term which takes neutral-plasma flow direction into account, and thus can be negative when those vectors are in the same direction. Finally, Q_{w2} is the wind heating term, the work done by the neutral wind on a static plasma background. In this study, Q_c, Q_w and Q_j are all treated and discussed seperately so as to extract the detailed contribution the neutral winds are making to Joule heating.

3.1.1 Diurnally-Varying Processes

When referring to processes that change diurnally, it is necessary to define our frame of reference. For example, a fixed local time system, centred looking down on one of the Earth's spin axis poles, will not experience varying degrees of sunlight over a 24-hour period (apart from miniscule seasonal changes due to the Earth's orbit). However, a system centred looking down on any other region, such as one of the Earth's geomagnetic

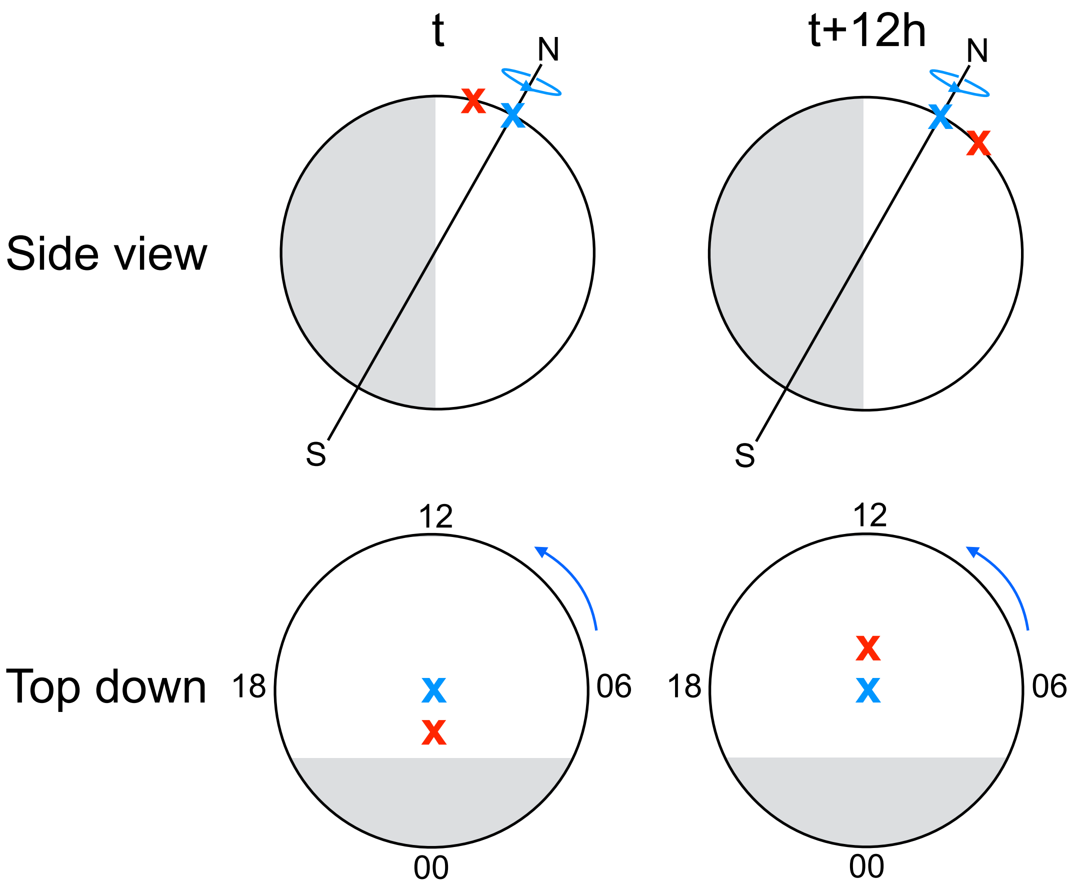

Figure 3.1: Diagram showing the diurnal changes of both the north spin axis pole (blue x) and south geomagnetic pole (red x) on Earth, fixed in local time. The grey area indicates the region of the Earth in darkness. Blue arrows indicate the direction of Earth's rotation. Left images are at a time t, whilst the right are at a time 12 hours later (UT). Top images are a side view of the Earth with the Sun to the right. Bottom images show a top down view of the spin axis pole, with values of solar local time around the edge.

dipoles, will vary because of the offset to the spin axis. This is shown schematically in Figure 3.1, where the blue and red crosses indicate the location of the spin north pole and geomagnetic south pole respectively (not to scale). In this study, diurnal processes are defined as those occuring periodically due to the 24h day-night cycle in the centred dipole coordinate system with a fixed magnetic local time (MLT). This is the most common system to use when considering ionospheric interactions with the magnetosphere, as it roughly places the viewer at the centre of the Dungey cycle convection and open/closed field line boundary (see section 1.3.3). The exact coordinate system used herein is AACGM, and is described in more detail by Shepherd (2014). For the purposes of this study, we assume **E** and **B** do not vary significantly diurnally in a fixed MLT frame. This might not strictly be true, but the effect has been shown to be suitably small (between 10-30% of the total change in cross polar-cap potential; Cnossen et al. (2012)).

3.1.1.1 Pedersen Conductivity

The most obvious diurnal variation, which has already briefly been touched upon, is the varying degrees of solar irradience that can be seen in Figure 3.1. We saw in section 1.3.1 that the density of the ionosphere is dependent on the amount of solar EUV radiation which falls incident on the thermosphere, which is linearly proportional to its conductivity (Chapman, 1956). Thus, Σ_P varies both diurnally and seasonally.

In order to determine the total Σ_P for the high-latitude ionosphere, two components were evaluated seperately. The first, Σ_P^{Sun}, is the contribution due to changing solar EUV radiation. An empirical relation exists for this which has been shown to be well representative (e.g. Zhang et al. (2005), after Rich et al. (1987)):

$$\Sigma_P^{Sun} = 12.5\left(\frac{f_{10.7}}{180}\right)^{\frac{1}{2}} \frac{0.06 + \exp\left[1.803\tanh\left(3.833\cos\chi\right) + 0.5\cos\chi - 2.332\right]}{\left[1 - 0.99524\sin^2\left(\lambda_{ss}\right)\right] \times \left[1 + 0.3\cos^2\left(\lambda_{ss}\right)\right]} \tag{3.2}$$

where $f_{10.7}$ is the 10.7 cm radio flux intensity, χ is the solar zenith angle and λ_{ss} is the sub-solar point co-latitude. This equation captures the conductivity variation both diurnally (as λ_{ss} changes) and seasonally (as χ changes).

The second component of the Pedersen conductivity is that due to ionisation by particle precipitation, Σ_P^{Aurora}. This is especially relevant in the vicinity of the auroral oval, and during the hemispheric winter months where Σ_P^{Sun} will be lower. Hardy et al. (1987) developed an empirical relation for Σ_P^{Aurora} as a function of the auroral energy (E_0) and energy flux (I):

$$\Sigma_P^{Aurora} = \left[\frac{40E_0}{(15 + E_0^2)}\right] I^{0.5} \tag{3.3}$$

It is currently not possible to obtain these parameters with a large enough spatial coverage suitable for studies concerned with global scale variations (using instruments such as GUVI for example). However, Hardy et al. (1987) also developed a statistical model

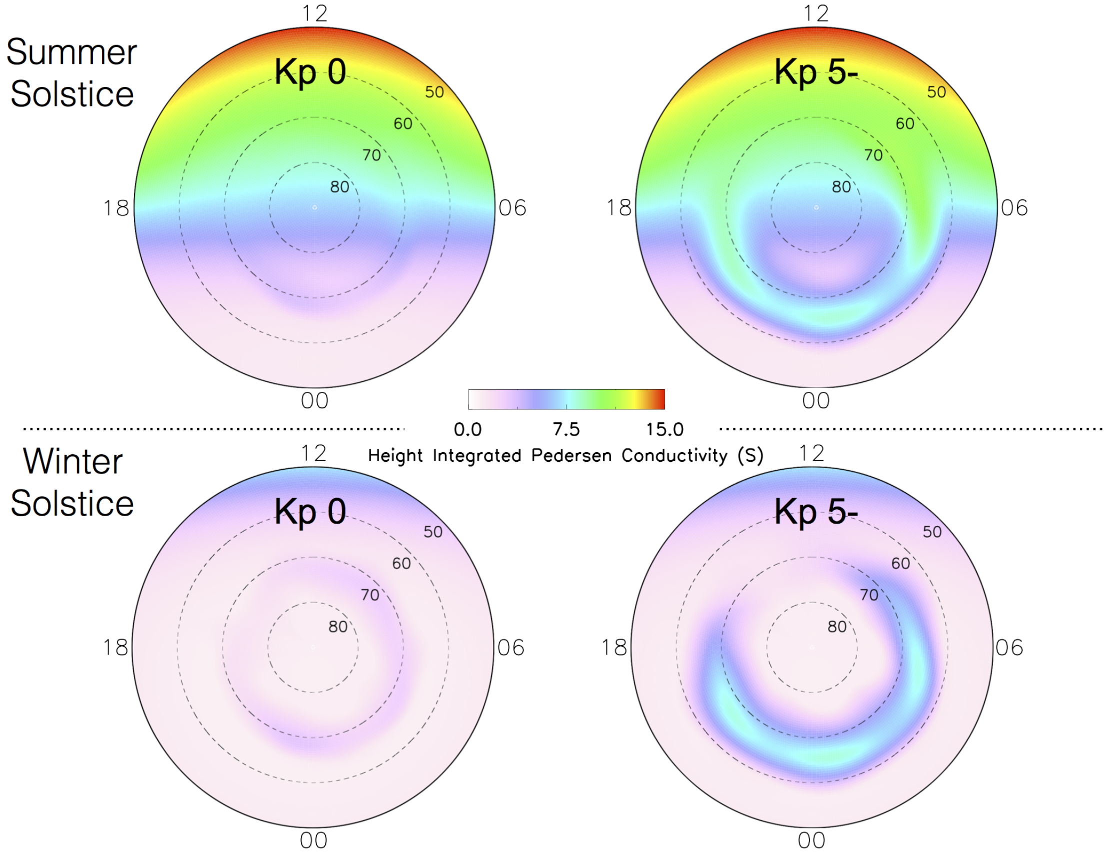

FIGURE 3.2: Height integrated Pedersen conductivities for upwards of 50° MLAT, as determined by the root-sum-square of Eq. 3.2 and the Hardy et al. (1987) statistical model. Plots are centred on the geomagnetic north dipole, with MLT around the edge. All plots at at a universal time of 00.

for Σ_P^{Aurora} using Eq. 3.3 and data from the DMSP and Solwind satellites, ordered by the geomagnetic Kp index.

Combining the two different contributions of the Pedersen conductivity requires taking the root-sum-square of both, i.e. $\Sigma_P = \sqrt{\left(\Sigma_P^{Sun}\right)^2 + \left(\Sigma_P^{Aurora}\right)^2}$. This is to account for cases where one of the sources of ion production is much more dominant than the other (such as Σ_P^{Aurora} being less important during the summer; Wallis and Budzinski (1981)). Σ_P determined using Eq. 3.2 and the Hardy et al. (1987) statistical model is shown in Figure 3.2 for Kp indexes of 0 and 5-, at the summer and winter solstices. For increasing levels of geomagnetic activity, the auroral oval of conductivity expands equatorward and intensifies. For decreasing solar zenith angle (i.e. varying UT and season), the dusk-dawn conductivity terminator moves further towards magnetic midnight, with increased Σ_P magnitude on the dayside.

We can interpret the output of these models in terms of how they affect the Joule heating rate described by Eq. 3.1, which we will generally expect to be higher in sunlit regions and in the vicinity of the auroral oval (although in Chapter 5, we show the latter of these might not always be a good assumption). Higher Kp indices will increase the total area integrated heating rate around the geomagnetic pole, and so will the tilting of the hemisphere to be sunward facing during the summer (and the geomagnetic pole with UT).

3.1.1.2 Neutral Winds

The velocity of thermospheric neutrals is also affected by increased solar EUV, although not as directly as the ionospheric conductivity. This is via the pressure gradient term of the momentum equation (Eq. 1.30), which at lower latitudes is the driver of the neutral wind diurnal tide. The resulting temperature increase from absorption of solar EUV increases pressure at all thermospheric altitudes, pushing neutrals towards the nightside in general. Other components of the momentum equation such as the Coriolis force, and importantly at high latitudes, the ion-drag term, act to deviate the neutrals from the diurnal tidal motion.

The Horizontal Wind Model 2014 (HWM14; Drob et al. (2015)) is an empirical model which aims to represent the thermospheric neutral winds climatologically, and is based on several years of data from ground based instruments (such as FPI's) and satellites (such as DE2). Inputs to the model are UT, day of year, geomagnetic ap index, altitude, and geographic latitude/longitude. To show extremes of varying solar pressure gradients, Figure 3.3 presents output from the HWM14 at two different times on the same day of year, for moderate geomagnetic activity. At 0600UT (1800UT), the geomagnetic pole is least (most) sunlit. In both wind patterns, the presence of an ion-drag induced dusk-cell can clearly be seen which migrates nightward as the reference frame rotates more into sunlight. Day to night wind speeds also become more enhanced, which are most obvious directly across the pole (which is also the general direction of

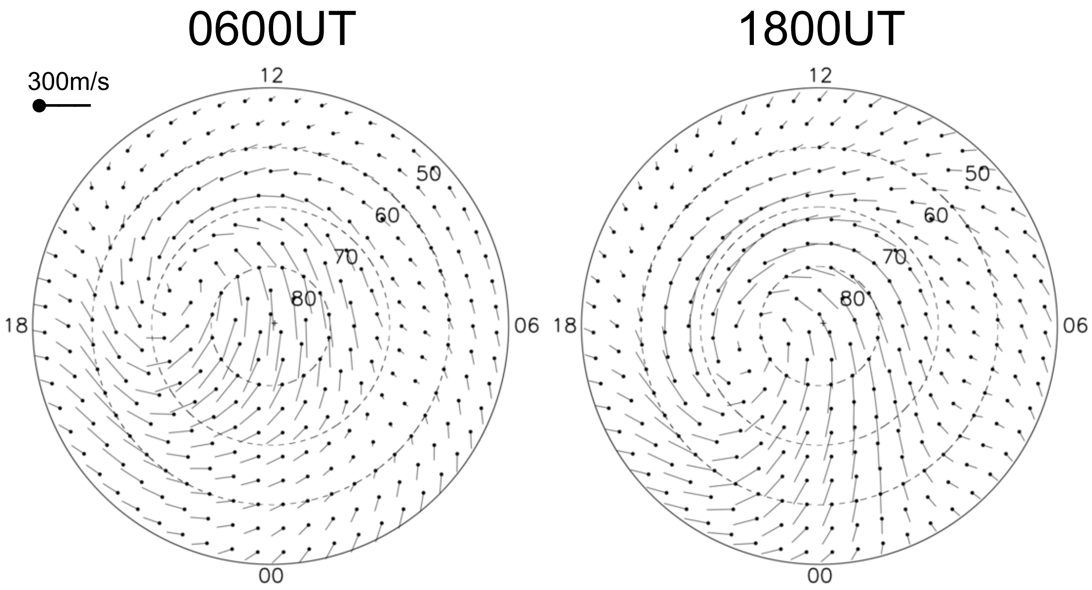

FIGURE 3.3: HWM14 output upwards of 50° MLAT for 0600UT and 1800UT at summer solstice, ap 22, 160 km altitude.

ion-drag statistically (Ruohoniemi and Greenwald, 1996)). During this study, HWM14 was run at a consistent altitude of 160 km which has been shown to reasonably represent the total height integrated thermospheric winds (Lu et al., 1995).

As described in section 1.4 and parameterised by the Q_{w1} term in Eq. 3.1, neutral-plasma alignment is an important factor for calculating the total Joule heating rate. If ion-drag was the only force acting on the neutrals to the point where global neutral winds matched the plasma convection exactly, there would be no Joule heating. Any deviation from each other results in enhanced Joule heating. If we consider the migrating neutral wind dusk-cell shown in Figure 3.3, along with a non-varying statistical plasma convection pattern for instance, Joule heating on the dusk-side will change quite drastically over a day as the neutrals moves in and out of alignment with the plasma convection cell. This is in addition to the diurnal variation due to conductivity that was described in section 3.1.1.1, however it is more complex because not only can it alter the magnitude, but also the global morphology of Joule heating.

3.2 Methodology

A database of northern hemisphere plasma convection patterns from 2000-2006 were used in this study, generated using a two-minute integration of all available data in the SuperDARN network (see section 2.1.3). A quality threshold of 200 plasma velocity vectors was set to remove patterns with insufficient data coverage, and the statistical model used to supplement data was that by Ruohoniemi and Greenwald (1996). Approximately 55% of all convection patterns in this period met the quality threshold, totalling around 800,000 maps of the high latitude electric potential. As we recall from section 2.1.3, the electric field is determined from the gradient of the electric potential.

Using each map of the convection electric field ($\mathbf{E}$), as well as the height integrated Pedersen conductivity (Σ_P), neutral wind velocity $\mathbf{U}$, and magnetic field ($\mathbf{B}$) from the models described previously, Joule heating, as well as the convection heating and wind correction terms, were calculated using Eq 3.1 everywhere in the northern hemisphere upwards of 50° MLAT. An equal area polar grid was used, centred on the geomagnetic pole and 1° wide in latitude. This maintains equal spatial resolution. The result is one Joule heating pattern corresponding to each SuperDARN convection pattern used. A limitation of this process is the usage of the geomagnetic ap index in the HWM14; which is a conversion of the kp index onto a linear scale, averaged over a 3-hour period from ground based magnetometer data (Dessler and Fejer, 1963). This means that the HWM14 is unable to represent the IMF dependence of the high latitude plasma convection, which has been shown to somewhat influence the neutrals statistically (Forster et al., 2008).

The Joule heating patterns were then averaged into statistical bins, which were chosen to extract changes due to season, UT, and geomagnetic activity level. These bins are shown in Figure 3.4a, for a total of 144 statistical Joule heating patterns representing two seasons (light and dark), 3 ranges of geomagnetic activity (low, medium and high) and 24 hours of UT. The bins for both season and geomagnetic activity were chosen to be broad enough to maintain a suitable number of patterns in each UT bin, a histogram of which is shown in Figure 3.4b. There is clearly a strong UT and seasonal dependence on the number of events, which implies a greater amount of ionospheric backscatter

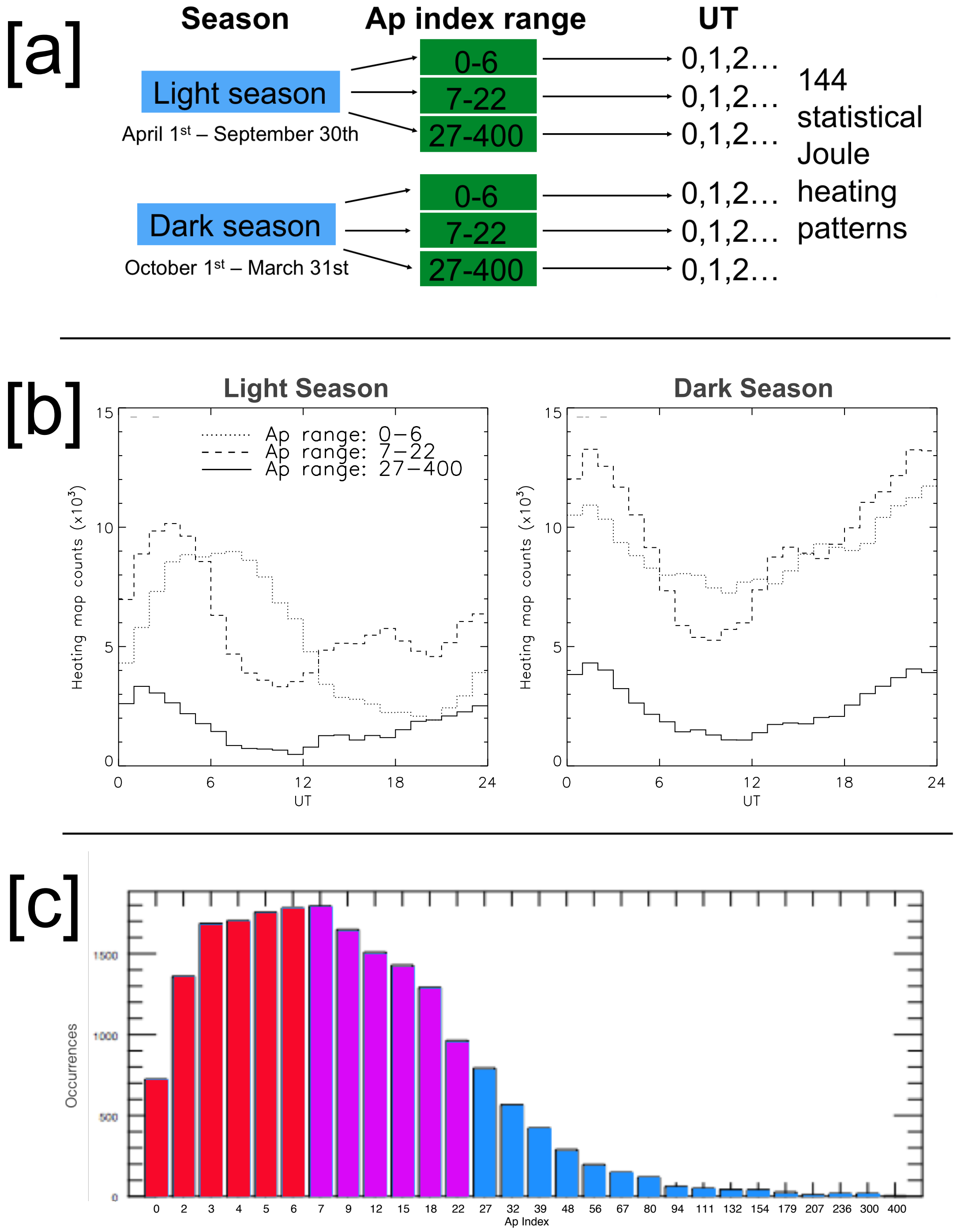

FIGURE 3.4: [a]: A diagram showing the binning of derived Joule heating patterns into statistical UT bins. [b]: Histograms showing the number of Joule heating patterns which go into each statistical UT pattern, for the defined seasons and geomagnetic activity levels. [c]: Histogram showing the distribution of events with ap index.

globally when the polar cap recieves less sunlight. This could be an observational bias of the SuperDARN radars, for instance due to the differences in HF wave propogation in day and night time ionospheres (e.g. Milan et al. (1997)), or coverage gaps in the network itself. It should also be noted that due to the rarity of extremely active periods (above ap 80/kp 6), the ap=27-400 range is heavily weighted towards the lower indices in that range (Figure 3.4c). It was decided to not lower this range further to include more data, as this would add a substantial amount of low activity data. In this study, we therefore simply categorize into low, medium and high activity levels where the convection electric field is expected to get progressively stronger, whilst extending more equatorward.

3.3 Results

Figure 3.5 illustrates the global morphology and magnitude changes in Joule heating, over the course of a 24 hour period, due to the diurnal processes described in section 3.1.1. Shown here are the Q_c (a) , Q_w (b) and Q_j (c) statistical patterns, every 3 hours of UT, for the 7-22 ap index range, light season.

It can immediately be seen that the magnitude of Q_c varies over the course of the day, with a hemispheric minimum/maximum near 03 and 15UT respectively. Enhancements are confined to the regions where the electric potential gradient ($\mathbf{E}$) is statistically steepest. Here, those are the dayside cusp region that usually coincides with the convection flow reversal boundary (around 80° MLAT, noon MLT), and the dawn/dusk flanks (around 70° MLAT, between 01-10 and 13-22 MLT).

The smallest and greatest magnitudes of negative/positive Q_w occur near 03 and 15UT respectively, similar to what is seen in Q_c. Q_w however has a more complex, non-uniform evolution with UT. This is because as previously mentioned, Q_w can be either positive or negative depending on ion-neutral velocity vector orientation. This is clearest on the duskside, where the regions of neutral wind “heating” and “cooling” (i.e. a reduction in potential heating) changes quite drastically over a 24-hour period. For instance, the region by 75° MLAT changes from negative to positive Q_w around 06UT, then enlarges and strengthens through to a maximum at 12UT. This duskside

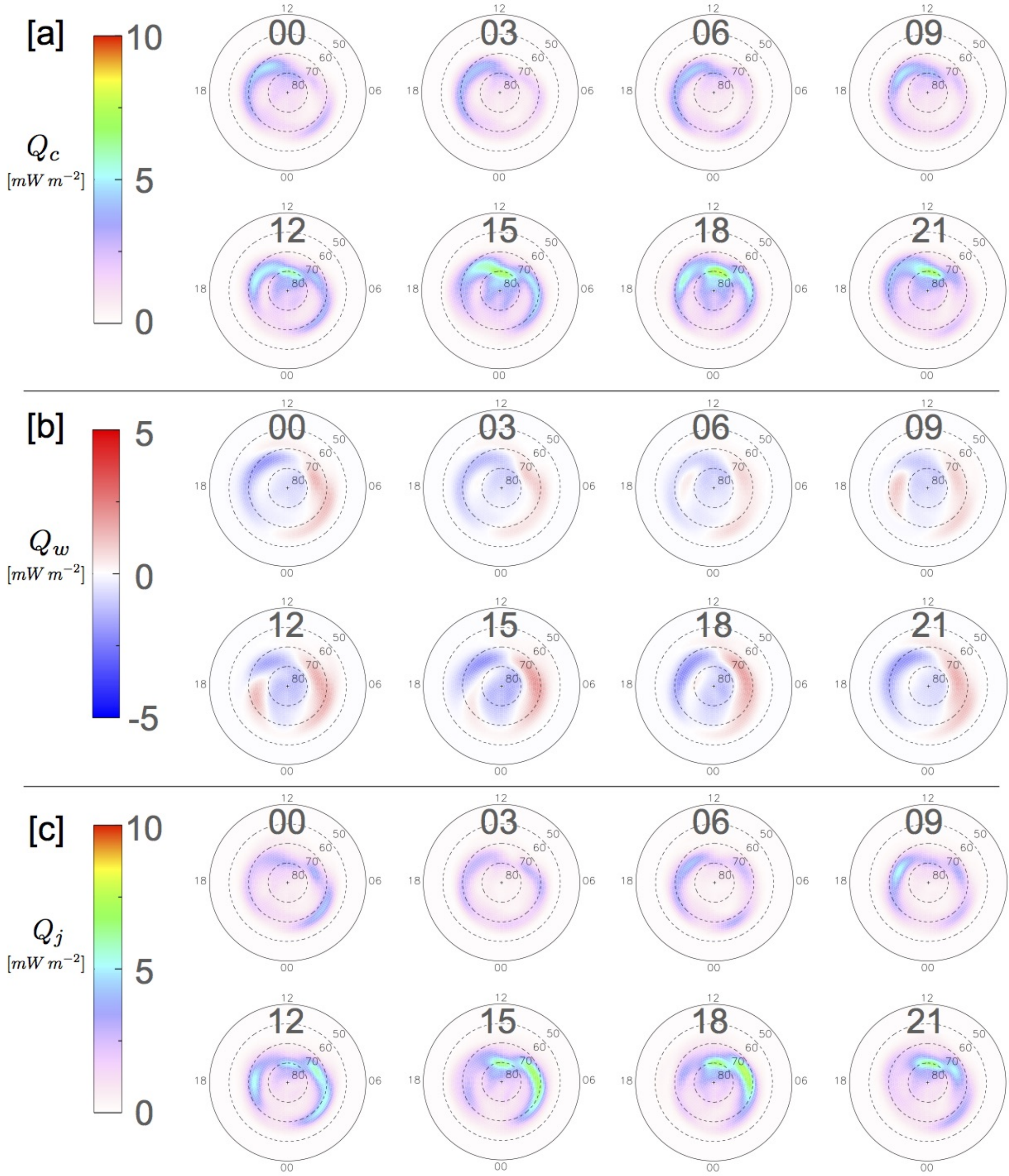

FIGURE 3.5: Q_c [a], Q_w [b] and Q_j [c] statistical plots at 3-hour UT intervals during the light season (April 1st - September 30th), for the moderate geomagnetic activity level ap range (7-22). Plots are in a polar format centred on the geomagnetic pole and orientated with the sun at the top, magnetic local dawn to the right. Plots extend to 50° MLAT.

heating enhancement then dies out by 18UT, leaving only a reduction in Joule heating again. The dawnside behaviour of Q_w is much simpler, in that it is always positive. The noon-midnight cross-polar cap Q_w always imparts a net decrease in Joule heating.

Summing Q_c and Q_w gives the total Joule heating (Q_j) maps shown in Figure 3.5c. Due to the contribution of the neutral winds, Q_j differs greatly from Q_c in many ways. For instance, as a result of consistent wind cooling across the polar cap, the Q_c cusp hot spot is diminished at all UTs. Conversely, there is a greater enhancement of Q_j all across the dawnside. As before, overall heating magnitudes are at a minimum at 03UT and a maximum at 15UT - except for on the duskside. This is where the morphology (i.e. the sign) of Q_w varies with UT. Here Q_j is generally diminished from Q_c, to the point where it is now lower than on the dawnside from 12UT-00UT.

To evaluate this UT dependence for the other bins shown in Figure 3.4 (the other geomagnetic activity ranges, as well as the hemispheric dark season), we now average each statistical map into MLT sectors and plot keograms of the results with changing UT. We use 24 MLT sectors in total, spanning one hour of local time each, but exclude data above 80° MLAT in the averaging (as including this area will distort the morphologies of the dawn/dusk flanks). The results are shown in Figure 3.6, with a black cross placed in the panels for Q_c and Q_j to mark where the largest heating value was for that timestep.

Firstly, it is noted that in all Q_c keograms, the region of maximum heating is nearly always in the pre-dusk region at around 16 MLT. For increasing geomagnetic activity, this region moves closer to magnetic noon. In the dark season, the spatial variability of the peak Q_c is higher, especially for the ap=27-400 geomagnetic activity range. Overall peaks in heating occur around 1800UT for both seasons and all activity ranges, which is also the time that dawnside enhancements of Q_c are noticeable.

Dawnside Q_w is always positive with changing UT, for both seasons and all ap index ranges. On the duskside it is initially always negative, but there is a period of time centred around 11UT/19MLT where it becomes positive. The UT length and local time width of this heating period varies with both season and ap index range; increased geomagnetic activity for instance narrows the local time and UT extent, whilst the dark season widens both (compared the light season).

As a result of the contribution from the neutrals and much like in Figure 3.5, Q_j is enhanced on the dawnside for all ap ranges and both seasons. An increase in magnitude is seen for increasing geomagnetic activity in both seasons, and Q_j is larger

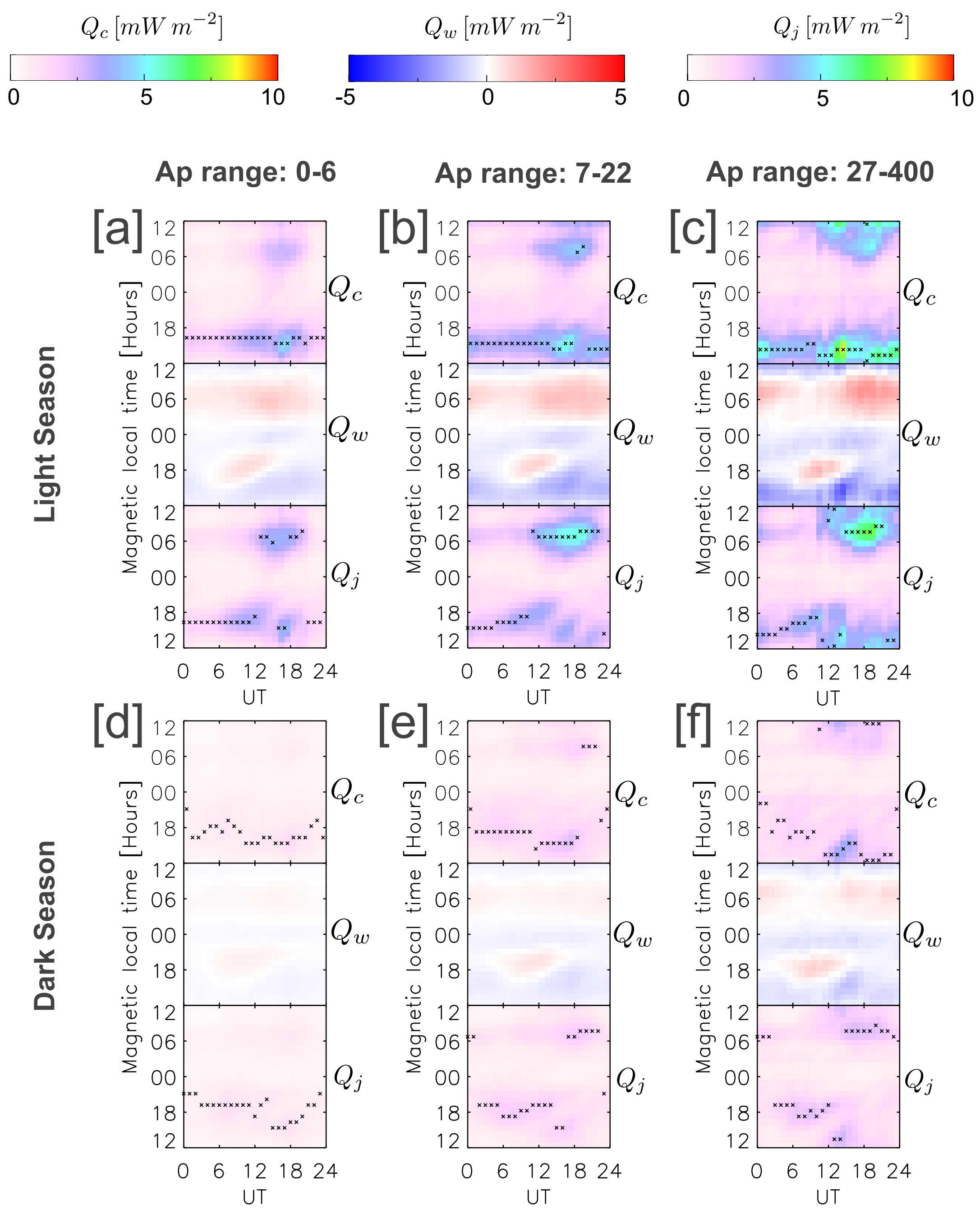

FIGURE 3.6: UT-Keograms of the average Q_c, Q_w and Q_c in each hour of MLT for [a]: Light season, ap=0-6 [b]: Light season, ap=7-22 [c]: Light season, ap=27-400 [d] Dark season, ap=0-6 [e]: Dark season, ap=7-22 [f]: Dark season, ap=27-400. The black crosses indicate where the highest value of Q_c and Q_j are for that UT bin.

in the light season compared to the dark. We also observe that the local time where Q_j is a maximum is now much more often on the dawnside compared to Q_c, especially from

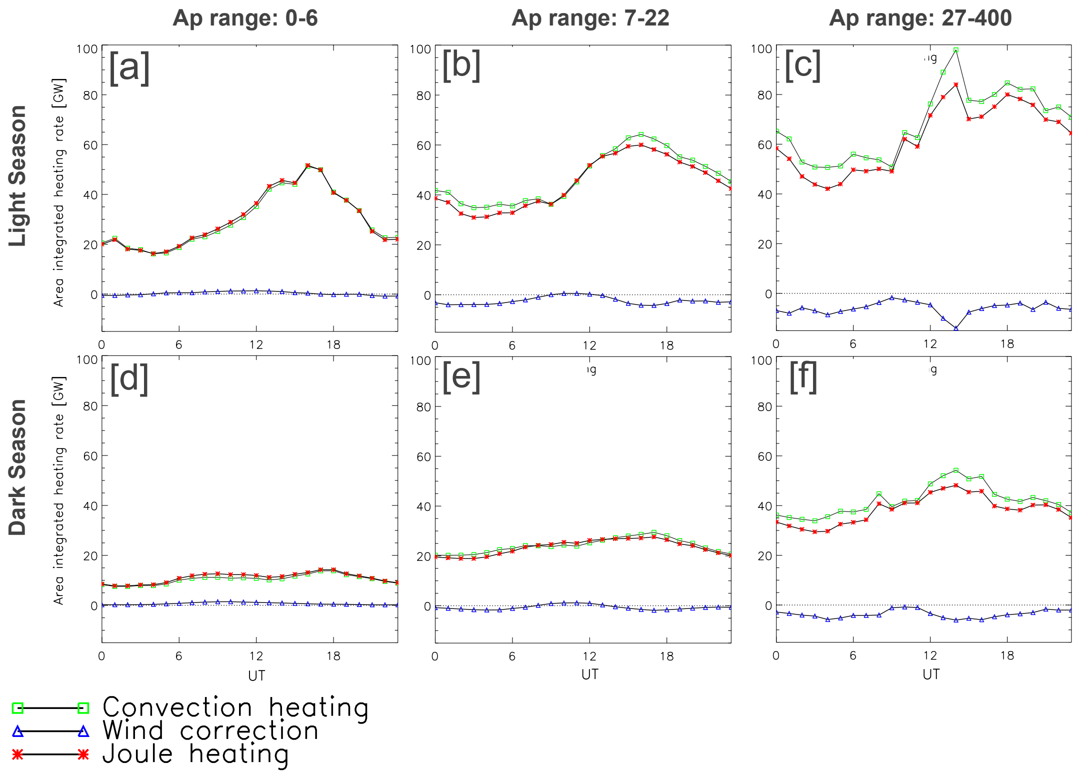

FIGURE 3.7: UT dependences of the area integrated convection heating, wind correction and Joule heating rates, upwards of 50° MLAT, for each Ap index range and season.

12UT onwards. Increased geomagnetic activity also appears to cause more dawnside Joule heating maxima. Duskside Joule heating is much more variable for all activity ranges and both seasons than duskside Q_c. During the light season, there is a clear nightward migration of peak Joule heating between 06 and 12UT which does not occur in the dark season.

TABLE 3.1: Minimum and maximum values of ΣQ_c, ΣQ_w and ΣQ_j for each of the 24-hour UT ranges shown in Figure 3.7. All values are in GW, to the nearest whole number.

	Light Season			Dark Season		
ap Range	0-6	7-22	27-400	06	7-22	27-400
Max ΣQ_c	55	64	98	14	30	54
Min ΣQ_c	16	34	51	8	21	34
Max ΣQ_w	2	1	-2	2	1	-1
Min ΣQ_w	-1	-4	-14	0	-2	-7
Max ΣQ_j	55	60	83	14	28	48
Min ΣQ_j	16	32	42	8	18	29

Using the statistical patterns we have developed, we now calculate the entire northern hemisphere integrated Q_c, Q_w and Q_j rates to observe their dependence on season, geomagnetic activity and UT. This is done by multiplying the heating rate in each grid cell by the area it encloses (at a projected altitude of 160 km), and then summing over all cells. The results are shown in Figure 3.7, and are hereby referred to as ΣQ_c, ΣQ_w and ΣQ_j for the area integrated convection heating, wind correction, and Joule heating rates respectively. Table 3.1 lists the minimum and maximum ΣQ_c, ΣQ_w and ΣQ_j for both seasons and all ap index ranges.

ΣQ_c (red stars) for both seasons and all ap index ranges has a relatively simple diurnal variation, with a peak around 16UT and trough near 04UT. The magnitude, as well as the difference between the maximum and minimum ΣQ_c rates, is larger for increasing ap index range and in the light season. There is more variability in the ap 27-400 bins (Figures 3.7c and f).

ΣQ_w (blue triangles) is much smaller in magnitude than ΣQ_c, but varies differently with UT. The variation is semi-diurnal, with peaks near 00UT/11UT and troughs near 4UT and 16UT. As the ap index range increases, the global contribution becomes increasingly negative; in fact, the neutrals never provide a net positive contribution to global Joule heating rates for the 27-400 range (Figures 3.7c and f). Increasing ap index range is the main contributor to increased ΣQ_w magnitudes, although they are also slightly higher in the light season compared to the dark. ΣQ_j (green squares) is close to ΣQ_c for all bins and follows a similar diurnal trend (minimum and maximums at 04UT and 16UT respectively). In fact during the 0-6 ap index range, ΣQ_w has an effect so little such that both the minimum and maximum ΣQ_c is approximately equal to the minimum and maximum ΣQ_j (to the nearest GW; see table 3.1). However, the deviation caused by the neutral winds becomes considerable in the 27-400 ap index range for both seasons and at certain UT's.

Table 3.2: Minimum and maximum values for the curves shown in Figure 3.8. All values are to the nearest 0.5%.

	Light Season			Dark Season		
ap Range	0-6	7-22	27-400	06	7-22	27-400
Min ΣQ_w%	-3.5% 0UT	-11% 04UT	-17% 04UT	+2.5% 00UT	-8% 04UT	-18% 04UT
Max ΣQ_w%	+4.5% 10UT	+1.5% 11UT	-4% 09UT	+13.5% 10UT	+5% 11UT	-2% 10UT

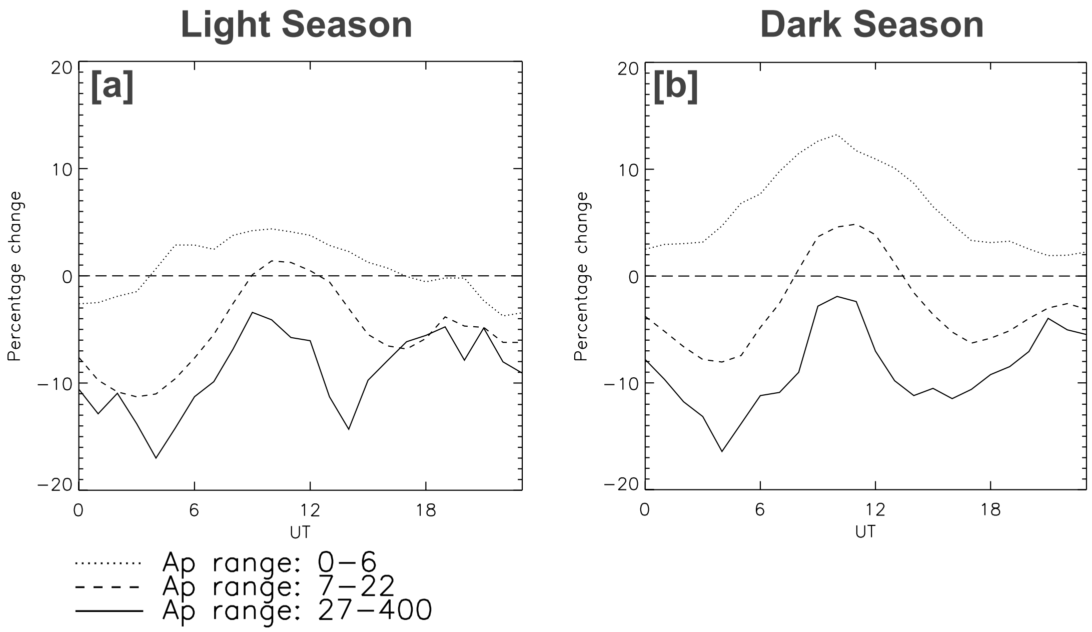

FIGURE 3.8: How the neutral wind contribution to the area integrated Joule heating rates varies with UT for each of the ap index ranges and seasons shown in in Figure 3.7.

To better show the importance of the neutral winds in each of the season and geomagnetic activity bins, Figure 3.8 shows the percentage contributions ΣQ_w makes to each ΣQ_j with varying UT. Table 3.2 lists the minimum and maximum values of each, with the UT they occur at.

It can be seen that the times where neutral winds contribute the most and least globally to Joule heating usually remains similar, irregardless of season and geomagnetic activity. That is, always around 4UT and 11UT for the minima and maxima respectively, except for the lowest ap index range. There is also an additional, lower magnitude, minimum and maximum around 00UT and 15UT for all the curves shown in Figure 3.8; a product of the semi-diurnal variation of ΣQ_w seen in Figure 3.7.

3.4 Discussion

Overall, the variation of the convection heating with UT is relatively easy to explain, and is easiest to see in the area integrated rates (Figure 3.7). The minimum and maximum of

ΣQ_c occur at 04 and 16UT, which are the UTs that the northern hemisphere geomagnetic pole is least/most illuminated by sunlight. This change is most prominent on the Earth's dayside because the solar conductivity terminator is quite sharp (see Figure 3.2), which is why Q_c varies much more in this region (see Figure 3.5a) than on the nightside. Because the wind correction typically does not contribute more than ±20% (Figure 3.2), the total Joule heating also exhibits this UT variation clearly.

It was also considered that UT variations in the convection electric field (**E**) could contribute to variations ΣQ_c. For a given ap index range, this would result in Q_c morphology changes. Examining Figure 3.6, the only significant local time variation in Q_c occurs for the ap=27-400 range and in the dark season. The former could be attributed to a lower number of Joule heating patterns at high geomagnetic activity (see Figure 3.4), whilst the latter is consistent with findings by Matsuo et al. (2003) and Pettigrew et al. (2010) that reconnection topology, and in turn the electric field, **E**, can be more variable during the hemispheric winter months during IMF B_z northward conditions.

As geomagnetic activity increases, so does the strength of **E** in general. **E** is strongly dependent on the orientation of the IMF, but ap index is ultimately derived from ground magnetometer data, and so doesn't have an inherent IMF dependence. A southward orientated interplanetary magnetic field is however more likely to result in a higher ap index; this can be seen in Figure 3.9, which is the distribution of ap indices with IMF B_z and B_y from 1999-2006. As all three of the ap index ranges presented in this study are heavily weighted by ap indices under 100, the statistical Joule heating patterns used are made up of convection electric fields spanning all clock angles. The result is patterns of the high-latitude convection which resemble a simple two cell morphology, where **E** grows in magnitude and extends to lower latitudes with increasing ap index. This is not unlike the convection model by Heelis et al. (1982), which uses the kp index. The strengthening of **E** can be seen in Figure 3.6 and Table 3.1 because the magnitude of Q_c increases with ap, as much as a factor of 4 in the dark season. This is consistent calculations of Q_c from older studies (e.g. Ahn et al. (1983) and Foster et al. (1983)).

The diurnal variation of the wind correction term, leading to the morphology

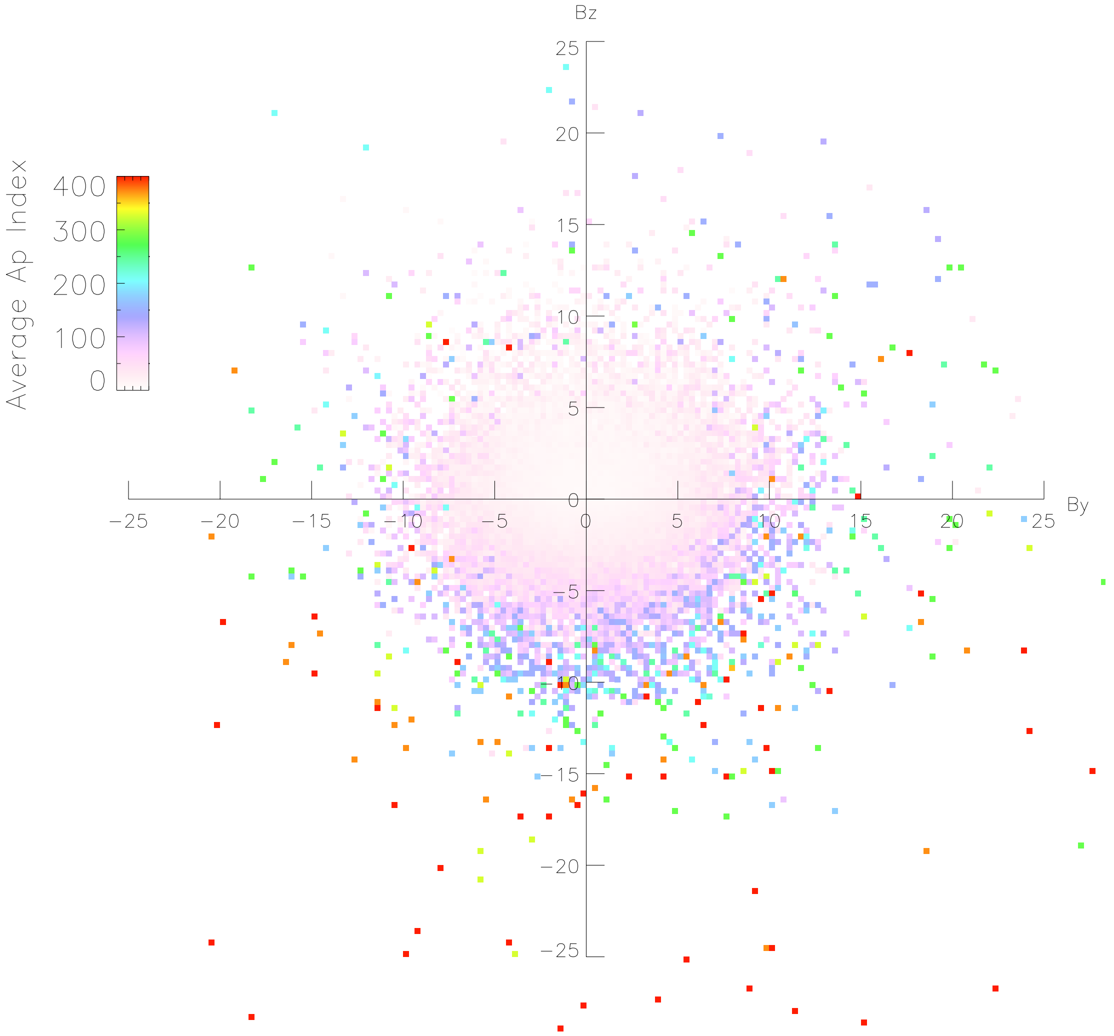

FIGURE 3.9: Distribution of average the ap index with IMF B_z and B_y from 1999-2006. Data is from the NASA OMNI database.

changes seen in Figures 3.5 and 3.6 can best be explained by recalling the diurnal variation of the neutral winds shown in Figure 3.3 due to solar pressure gradients. This generally applies to both seasons used in this study, although the variation in solar pressure during the dark season is much weaker than in the light for the latitudes considered. If we consider an arbitrary plasma convection pattern which does not vary with UT (or at least, not as much as the neutral wind pattern), then as mentioned in section 3.1.1.2, the neutrals will move in and out of alignment with the plasma, modifying Joule heating. This is shown with example HWM14 output from two different UTs at summer solstice

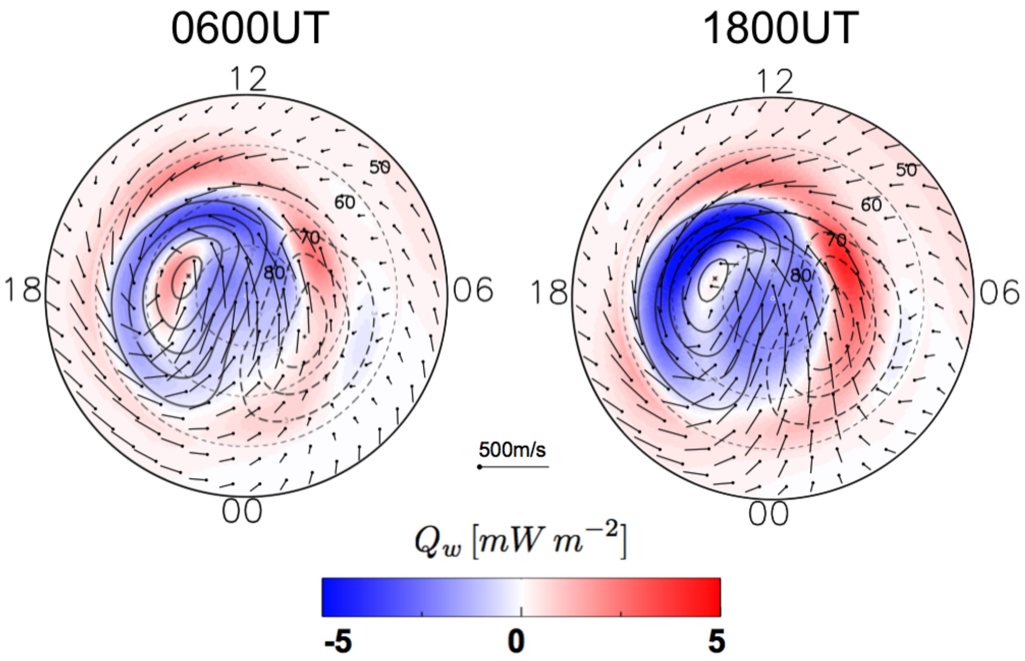

FIGURE 3.10: Two abritrary intervals of Q_w at summer solstice. Overlain are the corresponding plasma convection contours and HWM14 output (ap=48, $f_{10.7}$ = 226) used in the calculation.

in Figure 3.10.

For this illustration, it can be seen that Joule heating is always enhanced (positive Q_w) across the dawnside where the neutrals and plasma flow anti-parallel to each other. This is also what occurs statistically, as shown by the Q_w and Q_j keograms in Figure 3.6. Because the magnitude of Q_w is dependent on the plasma-neutral velocity difference, stronger neutral winds associated with larger solar pressure gradients (Dhadly et al., 2018), greater geomagnetic activity (Aruliah et al., 1991) and a balancing of the Coriolis and centrifugal forces (Forster et al., 2008) all lead to the variation of dawnside Q_w with UT, season and ap index range seen in this study. High dawnside Joule heating is a common feature of many studies, both in models and statistics (Deng and Ridley, 2007; Matsuo et al., 2003; McHarg et al., 2005; Thayer et al., 1995).

Across the polar cap, both solar pressure and the ion-drag force act very generally in the same direction, leading to the broad wind cooling (negative Q_w) seen in Figure 3.10 and the statistical patterns. This translates into the total Joule heating rate, largely reducing magnitudes across the noon-midnight meridian for all UTs (Figure 3.5c). On the duskside, the neutral wind morphology is generally quite close to that of the plasma, and thus also mostly reduces Joule heating. But as can be seen in Figure 3.10, varying solar pressure pushes a neutral wind cell through the plasma convection, creating discord between the plasma and neutral velocities and thus generating heat. This means the morphology of duskside Q_j is quite variable with UT.

We also observed that the size of the duskside wind heating region shortens in local and universal time extent with increasing ap index range (Figure 3.6, Q_w plots). This is because as geomagnetic activity increases, we also expect the strength of the ion-drag force to increase. This pulls neutrals more closely into alignment with the plasma at high latitudes, resulting in a reduction in Joule heating compared to quiet conditions.

In examining the area-integrated wind correction rates (ΣQ_w) shown in Figure 3.7, it was noticed that as geomagnetic activity increased, there was more of a tendency for the neutral winds to provide a net reduction in Joule heating. This is in agreement with Lu et al. (1995), and shows that the thermosphere is more often a current dampener than a current generator for the ionosphere, except for geomagnetically quiet conditions (Figure 3.7a and d). Over the course of a single 24-hour period, the contribution of the neutral wind to global integrated Joule heating rates can vary by as much as 16% (dark season, ap=27-400), and is generally higher in the dark season compared to the light season. We postulate that this is because of the difference in conductivity between the seasons, and that geomagnetic activity is a stronger mediator of neutral wind speeds than solar EUV pressure. This is almost certainly true for the high-latitude plasma convection (Ruohoniemi and Greenwald, 2005), and has also been seen in neutral wind statistics (Killeen et al., 1995).

3.5 Summary

A statistical study of the diurnal variations in northern hemisphere Joule heating rates has been presented, with special consideration for varying levels of geomagnetic activity and season. Approximately 800,000 SuperDARN electric potential patterns were used, in conjunction with the HWM14 and conductivity models by Hardy et al. (1987) and Rich et al. (1987). The neutral wind contribution to the overall Joule heating rate, known as the wind correction, was examined separately in order to determine its importance and explain its variability with universal time. To summarise, the conclusions of this chapter which add to our understanding of the thermosphere-ionosphere system at Earth are:

- The ion-drag force acts to orientate neutrals into the plasma direction on the duskside, but less so on the dawnside due to a balance between ion-drag and centrifugal/Coriolis forces. As geomagnetic activity increases, so does ion-drag, and thus the neutral winds have a tendency to reduce Joule heating rather than to increase it.
- Joule heating morphology varies considerably with UT on the duskside because the neutral winds are affected by varying solar pressure gradients, generating discord between the statistical plasma and neutral wind cells present there.
- Neutral winds consistently enhance Joule heating on the dawnside. This varies significantly with UT and season, as solar pressure gradients increase neutral wind speeds anti-sunward, against the traditional flow of plasma convection.
- The percentage contribution of neutral winds to global Joule heating rates in the hemispheric dark months is greater than in the sunlit months. This could be because high conductivities contribute much more to convection heating term than the wind correction than they do to the wind correction term.

As this study considered only the climatology of the neutral wind contribution to Joule heating, it was effectively assumed that the neutrals had completely reached an equilibrium with regards to ion-drag. In reality, if the plasma flow pattern were to change morphology considerably (such as due to a change in the IMF for instance), the heavy neutrals would require constant forcing from the plasma over some unknown length of time before they became representative of the statistical patterns shown in this chapter. This has implications for Joule heating, as it will be enhanced during the re-orientation period of the neutral wind. The following chapter will examine this neutral wind “lag” time in more detail.

Chapter 4

Spatially Resolving the High Latitude Neutral Wind Response to Changes in Plasma Convection

The following chapter contains published work from the article:

Billett, D. D., Wild, J. A., Grocott., A., Aruliah, A. L., Ronksley, A. M., Walach, M.-T., & Lester, M. (2019). Spatially Resolved Neutral Wind Response Times During High Geomagnetic Activity Above Svalbard. Journal of Geophysical Research: Space Physics

During this study, both AG and JAW acted as academic supervisors. M-TW provided valuable discussion, and ALA, AMR and ML assisted with data acquisition and interpretation.

4.1 Introduction

As shown in Chapter 3, discord between thermospheric neutrals and ionospheric plasma plays an important role in the way energy is dissipated into the atmosphere. The high latitude plasma convection is relatively quick to respond to changes in the solar wind

(Murr and Hughes, 2001), and is the main driver of neutral winds at high latitudes through the ion-drag force (Killeen et al., 1984). Due to the comparative mass of the neutral thermosphere however, there is a much greater degree of inertia compared to the ionosphere. In other words, any changes in the plasma velocity, assuming it is forcing neutrals along the direction of plasma motion, will take some time to become fully apparent. The implication of this is that Joule heating will be increased, as there is now increased friction between the ionosphere and thermosphere. This "lingering" property of the thermospheric state is known as the neutral wind flywheel effect (Lyons et al., 1985).

This neutral wind delay to plasma changes has been the subject of numerous efforts over the years to quantify. Initial studies assumed that ion-drag was the only force acting on the high latitude neutrals, thus simplifying the neutral momentum equation (Eq. 1.30) to:

$$\frac{d\mathbf{u}}{dt} = \nu_{ni}\left(\mathbf{u} - \mathbf{v}\right) \tag{4.1}$$

Where ν_{ni} is the neutral-ion collision frequency, and $\mathbf{v}$ and $\mathbf{u}$ are the plasma and neutral velocity vectors respectively. In this case, it can be seen that the neutral velocity will approach the ion velocity in a time constant, τ, such that (after Baron and Wand (1983)):

$$\tau = \frac{1}{\nu_{ni}} = \frac{(\mathbf{u} - \mathbf{v})}{d\mathbf{u}/\delta t} \tag{4.2}$$

Using this method, only information regarding the plasma and neutral velocity was required to calculate τ. For example, Killeen et al. (1984) calculated τ by utilising numerous instruments on board the Dynamics Explorer 2 (DE2) spacecraft during quick (~19-minute) passes of the southern magnetic pole. Kosch et al. (2001) on the other hand used coincident ground based data from EISCAT and an FPI to do the same for a localised region in Norway, over the course of several of hours. Example results from each of these studies are shown in Figure 4.1. From Killeen et al., we can see that τ varies substantially (between 40 and 200 minutes) at different locations for any one time. Kosch et al. showed that this variability is even more drastic over long timescales and small spatial scales (varying by up to 300 minutes in the space of a 30-minute period). In general, these results are similar to all studies which have used τ as the true neutral

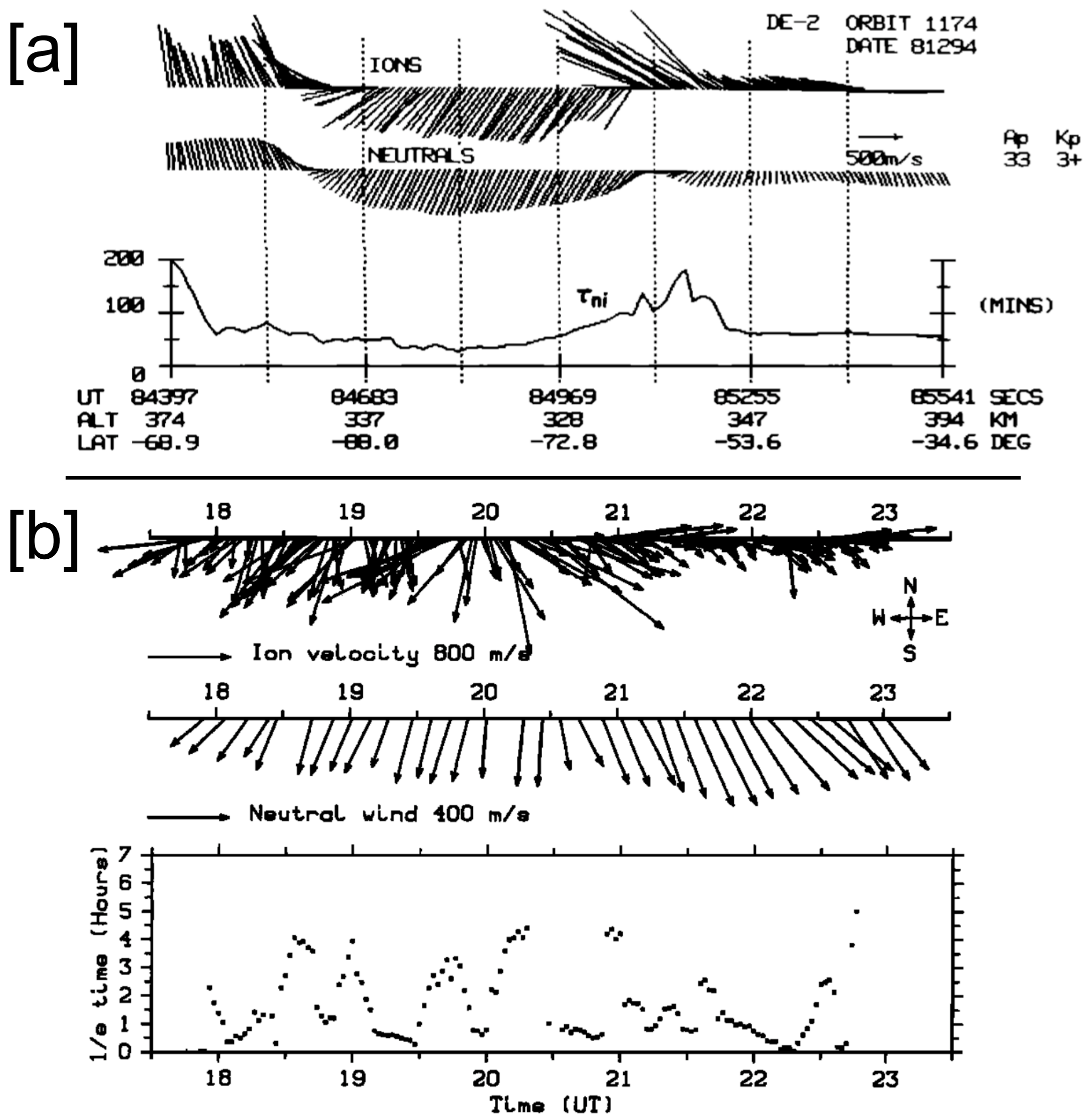

FIGURE 4.1: [a]: DE2 plasma and neutral parameters presented by Killeen et al. (1984) from a single, 19-minute pass of the geographic south pole. [b]: EISCAT-FPI measurements of the plasma and neutral velocity above Tromsø, Norway from Kosch et al. (2001). From to bottom in both: plasma vectors, neutral wind vectors, and the calculated ion-neutral time constant τ.

wind re-orientation time to plasma velocity changes (e.g. Heelis et al. (2002) and Joshi et al. (2015)). However, it is clear that there are still numerous challenges to determining thermospheric response timescales. The effects due to local time, time and spatial scales considered, amount of forcing from the plasma, and more, are still not well understood.

The τ approach to determining a re-orientation timescale is limited in its usefulness because the strength of the ion-drag force is rarely, if ever, consistent. This is due to the considerable variability of the plasma both spatially and temporally (e.g. Matsuo et al. (2003)), along with the dynamic UT, local time and seasonal dependences of the neutral wind at high latitudes, presented in the previous chapter. Therefore, applying the momentum equation as it was to determine a theoretical neutral acceleration timescale often results in large, unphysical values for τ when real data is applied to it. Hence the wide ranging values from the studies so far mentioned. The pressure gradient term, which is ignored in τ calculations, has also been shown to not be insignificant at high latitudes. For instance, solar EUV heating is large on the dayside, and even during the hemispheric winter months, has an impact on neutral velocities (Jacchia, 1965). Alternative sources of heat, such as Joule and particle heating, have also been attributed to imparting neutral wind responses (Nozawa and Brekke, 1995; Tsuda et al., 2009).

In this chapter, a different approach is taken to determining how long it takes for the high latitude neutral wind to respond to a change in the plasma convection. Using spatially resolved F-region neutral and plasma velocity measurements from SCANDI and SuperDARN respectively, the thermosphere-ionosphere system is considered carefully in a wider context than is possible with just point measurements. A cross-correlation analysis is performed for a high activity event to determine the lag of the neutral wind behind changes in the plasma, and the variability of lags across an approximate 1000 km FOV is examined. It is acknowledged that there will be no catch-all timescale which is representative of the entire thermosphere, but a determination method is presented here which aims to decrease ambiguity under certain conditions. In particular, this method works best for high activity events where there is a clear neutral wind signature to a plasma velocity enhancement.

4.2 Event Selection

In order to invoke a large thermospheric response to a change in ion-drag forcing, a search was conducted for large transitions of the IMF B_z component. This would result in the most drastic change to the plasma convection morphology and thus, if the ion-drag force can overcome other forces, result in an obvious neutral wind velocity change.

The search therefore began by finding all IMF B_z transitions where the magnitude was constantly the same sign at least 2 hours before and 1 hour after the transition. The before timescale was chosen so that the thermosphere had time to respond to the current state of the ionospheric convection, and the timescale after the transition was so that forcing from the plasma convection acted over a long enough time to elicit a neutral wind response. It is recognised that as previously mentioned, the full neutral wind accleration timescale could be well over 2 hours in length. However, as long as discrete and large neutral velocity changes occured in response to the plasma changes within the observation period, the cross-correlation analysis would work in producing a time delay of the neutral wind time series to the plasma.

Over the course of the years that SCANDI and SuperDARN were conjunctly operating over Svalbard, only 9 events met the IMF criteria where velocity data from both was available. From these, only one had consistent SuperDARN radar backscatter within the SCANDI FOV, along with uninterrupted neutral wind measurements. This one showed drastic neutral wind velocity changes after a corresponding plasma velocity change, i.e., large changes as an apparent response to a similar change in the plasma. The other 8 events without consistent backscatter showed slow and weakly varying plasma velocities, constrained more by the map potential algorithm (i.e., they were more dictated by statistical plasma convection patterns).

The event occurred on the 8th December, 2013, when SCANDI was mainly confined to the dawnside. An overview with IMF data, plus the average plasma and neutral velocity magnitudes within the SCANDI field of view is shown in Figure 4.2, including extra time either side of the B_z transition that occurred at around 06:00 UT. Even though the event was selected due to this specific period, IMF conditions were significantly disturbed in the hours preceding.

4.3 Results

Over the entire period shown in Figure 4.2, there were multiple high magnitude transitions of the IMF B_z component, along with generally high magnitudes of B_y. The

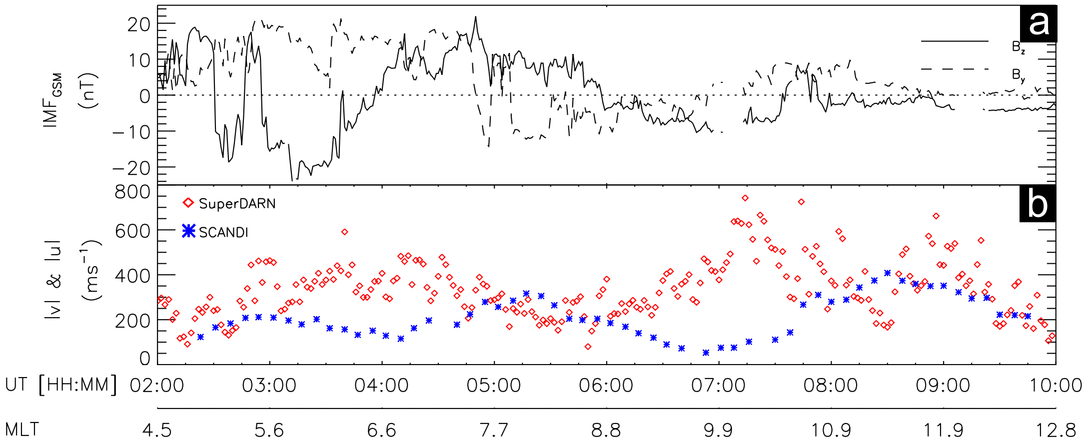

FIGURE 4.2: Ion-drag forcing event that occurred on the 8th December, 2013. [a]: IMF B_z and B_y components, taken from the NASA OMNI dataset. [b]: Spatially averaged plasma and neutral velocity magnitudes within the SCANDI FOV. The time steps of the velocity data are representative of their integration times, i.e. 2 minutes for each SuperDARN convection pattern and approximately 7.5 minutes for each SCANDI wind field. The SuperDARN data was also checked to ensure there was always radar backscatter within the SCANDI FOV.

average velocity magnitudes above Svalbard were highly changing, ranging from ∼100-750 ms^{-1} for the plasma and ∼50-400 ms^{-1} for the neutral wind. The timeseries of neutral velocity magnitudes appears to be roughly offset to the plasma timeseries by approximately 75 minutes. The temporal variability of the plasma was higher than the neutral wind, but its integration period was also shorter (2 minutes compared to ∼7.5 minutes).

During the period containing the first and second southward turnings of B_z, around 02:30 UT and 03:00 UT, the plasma sped up and continued to do so until B_z turned northward at 03:55 UT. The short-lived northward turning just before 03:00 did not appear to have any lasting effect on the plasma velocity. During the period of northward B_z between 03:55 UT and 05:55 UT, the plasma gradually slowed before picking up again just as B_z turned negative at 06:00 UT. Following was a period of rapid acceleration from ∼100-750 ms^{-1} in around 75 minutes. At this point, the magnitude of both B_z and B_y are much lower than earlier. The plasma slowed until 08:30 UT, sped back up till 09:00 UT, then slows again.

In order to compare and attribute changes in the neutral wind to changes in the

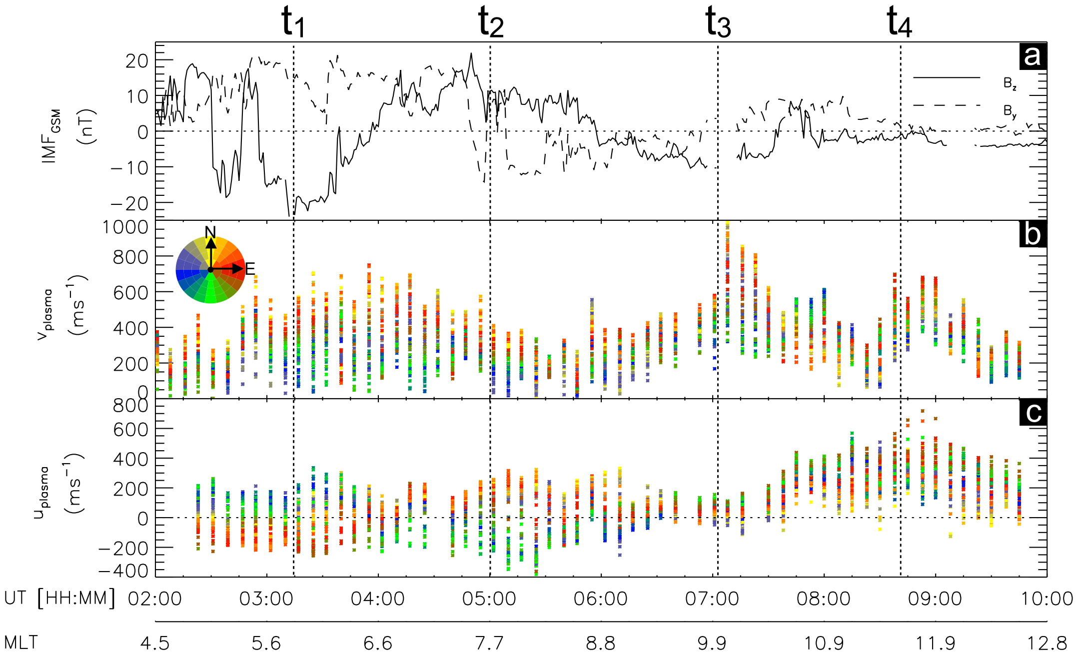

FIGURE 4.3: Same period as Figure 4.2, but velocity information is shown for all 61 SCANDI zones for both the plasma (b) and the neutral wind (c). The plasma velocity is still its magnitude, but the neutral wind has been averaged onto the same time integration and resolved in the direction of the corresponding plasma vector. Colours represent location within the SCANDI FOV, shown by the key in panel b. t_1, t_2, t_3, and t_4 are shown in 2d format in Figure 4.4.

plasma velocity, direction and spatial differences must be considered rather than simply averaged magnitudes. Figure 4.3 shows the same period as Figure 4.2, except the neutral velocities have been averaged onto the same time cadence and resolved into the direction of the plasma (u_{plasma}). Velocity data from each of SCANDIs 61 zones (see section 2.2) is also shown for both the plasma and neutrals, coloured by location within the FOV (the key for this is displayed in panel b). The plasma velocities in each zone were obtained from the respective location in the SuperDARN electric potential solution, described in more detail in section 2.1.3. The colouring of each timeseries bears no significance on the data itself, as its purpose is only to show groupings of similarly positioned zones. As an example, both plasma and neutral velocities in the eastern zones (red) tend to be similar, but the differences apparent. For full context on where SCANDI was located spatially within the plasma convection pattern, Figure 4.4 shows 4 MLAT-MLT format plots for the times marked as t_1, t_2, t_3 and t_4 in Figure 4.3.

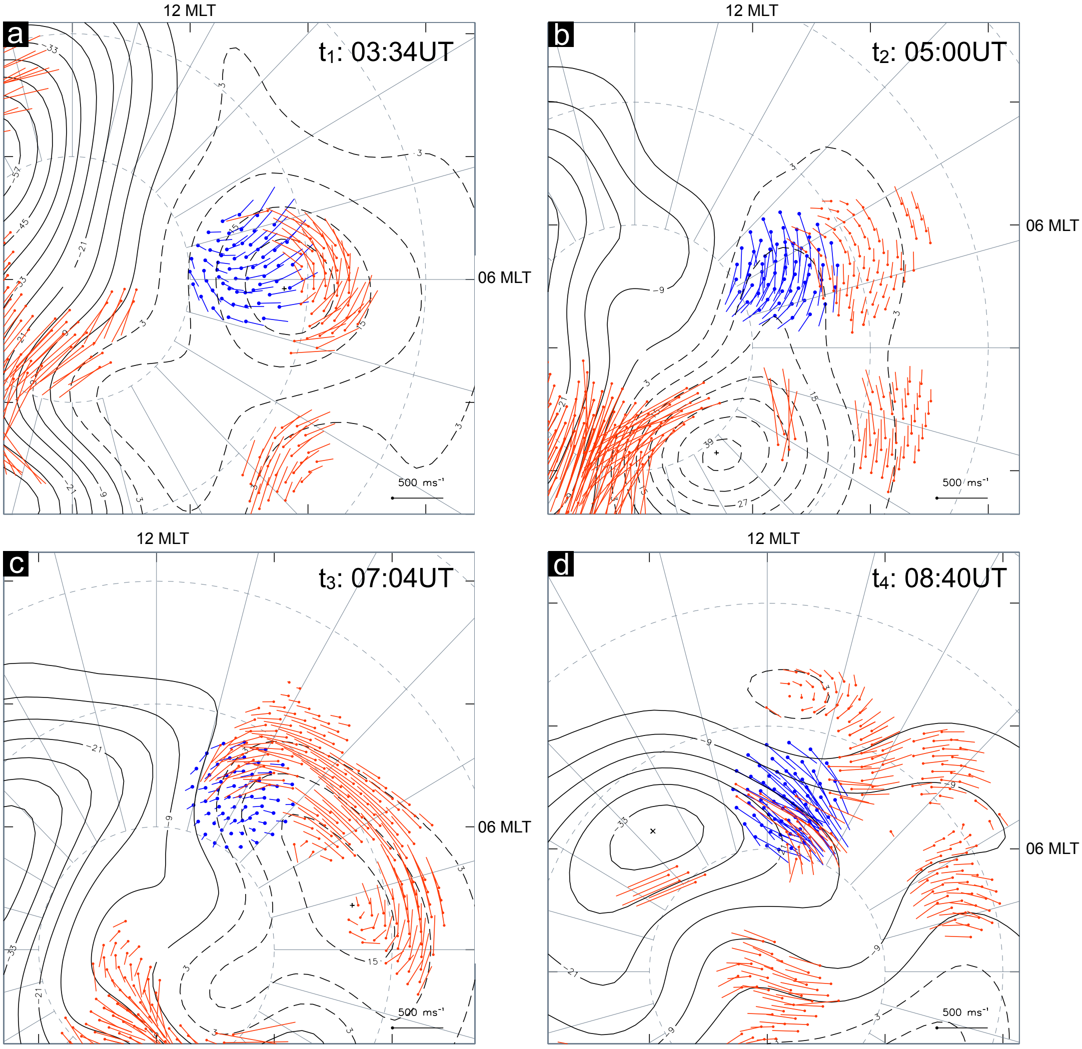

FIGURE 4.4: MLAT-MLT plots showing the neutral wind vectors from SCANDI (blue) on top of plasma convection contours using data from the SuperDARN network. The times shown correspond to t_1, t_2, t_3, and t_4 in Figure 4.3. Red vectors show the locations of SuperDARN radar backscatter for the integration period shown.

The spread of plasma velocities across the FOV was large during the first half of the event, which is where Svalbard (SCANDI) was located underneath the poleward edge of the dawnside convection cell focus (e.g. Figure 4.4a). During the latter half, the thermosphere above Svalbard was consistently located within the dayside convection throat region (e.g. Figure 4.4c and d), where the plasma flow was predominantly anti-sunward and less dispersed.

At the beginning of the event until 05:30 UT, roughly half of the zones flowed with

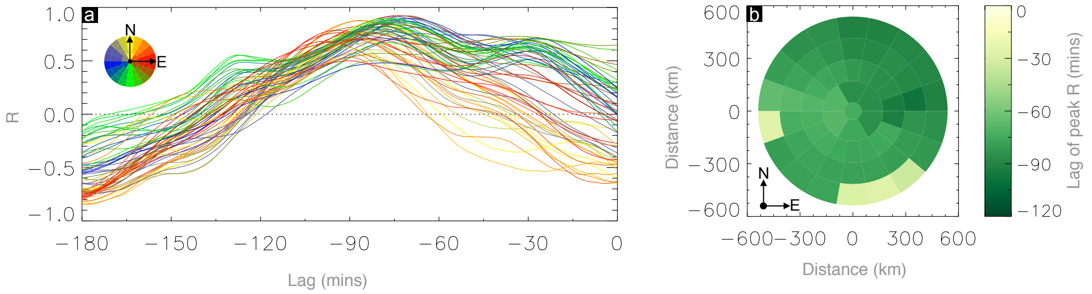

FIGURE 4.5: [a]: Cross-correlation curves of u_{plasma} from Figure 4.3c against the corresponding v_{plasma} (4.3b). Colour is based on location within the SCANDI FOV, a key of which is located in the top left. [b]: Zone configuration of the SCANDI instrument, coloured by the lag where correlation was highest in [a].

and half against the plasma (Figure 4.4a and then 4.4b). Plasma in the northern and eastern zones are the fastest after the B_z transition, whilst the corresponding neutral winds steadily sped up into the plasma direction, from opposing. During this time, the plasma flow speed in the south stayed between 50 and 400 ms^{-1}, and the neutrals remained opposing. From 05:30, where plasma in all zones sped up sharply, the neutral vectors were mostly consistent with each other and flowed slowly in the plasma direction (Figure 4.4c). They then accelerated to a velocity comparable to the plasma, and most zones overtook for approximately 10 minutes before the plasma sped back up (Figure 4.4d). The neutral wind then remained at a high speed until the end of the event, slowing very gradually.

As noted previously, Figure 4.2 indicates that the neutrals and plasma were offset in their velocity periodicity by around 75 minutes. To quantitatively determine that offset, which we use in this study as our defined neutral wind time delay, a cross-correlation analysis was performed using the 61 directionally resolved neutral wind velocity time series (Figure 4.3c) against corresponding plasma velocity magnitudes (Figure 4.3b). The plasma velocity magnitude (u_{plasma}) for the final half of the event was lagged one timestep at a time, backwards, up to a final lag of -180 minutes. It is noted that lagging u_{plasma} backwards only extracts the effects of forcing from the plasma to the neutrals, and not the other way around. The results of the cross-correlation are shown in Figure 4.5a using the same colour coding as in 4.3, whilst 4.5b shows the lag of peak correlation (R-value) in each SCANDI zone.

Each correlation curve is similar in shape, all peaking around the aforementioned value of -75 minutes. Some of the other zones, particularly those in the far south and west of the FOV also have slightly higher correlation peaks at an earlier lag of around -15 minutes. Apart from these zones, peak correlation varies between -67 and -97 minutes depending on location.

4.4 Discussion

As mentioned in section 4.2, the event presented here was the only one of nine that showed clear ion-drag forcing to the neutral wind (which met the IMF criteria stated), and had uninterrupted SuperDARN backscatter and SCANDI data within the FOV. It is also noted that this was the only event with IMF B_z magnitudes exceeding $\pm 5\,\mathrm{nT}$. The others, while technically meeting the IMF criteria, were not particularly disturbed conditions, and did not cause any significant changes to the convection of the plasma. This meant that even though our method of detection for whether or not the ion-drag force affected the neutral wind was by eye, the event presented here was an obvious choice.

By resolving the neutral wind velocity vector into the plasma direction, we effectively assume that the only force acting on the neutrals in that direction will be ion-drag. For the most part, this will be true due to the nature of the Coriolis, centrifugal, advection and viscous forces (Titheridge, 1995). Near the dayside cusp however (e.g. Figure 4.4c and d), plasma motion commonly acts in the same direction as the pressure gradient. But, any changes that could be due to pressure gradient variations have been statistically shown to at a very maximum only account for a $\sim 133\,\mathrm{ms}^{-1}$ change in the neutral wind velocity (Dhadly et al., 2018). Additionally, the event took place during the hemispheric winter, where solar irradiance on the pole does not change much with UT or local time (although, this would be true for much of the SCANDI data, as the instrument may only be operated in darkness). We therefore conclude that solar pressure did not cause the neutral wind enhancements seen during this event.

Factors such as latitude, MLT, as well as the expansion and contraction of the polar cap (Cowley and Lockwood, 1992) are also considerations when concluding which region of convection is under observation. The event took place primarily within the dawn sector and rotated into magnetic local noon, and as shown in Figure 4.4, SCANDI was always located underneath the poleward or sunward edges of the dawn convection cell. Here the flow is broadly anti-sunward, or eastward by the convection reversal boundary. Therefore, because the regime of high latitude convection did not vary too substantially within the thermospheric space observed by SCANDI, we assume in this study that the IMF B_z variability was having a direct control on the velocity magnitude of the plasma. In other words, the enhancements seen were due to a southward B_z, and the slowdowns were due to northward. Although, the high spread of plasma velocities until ~05:30 UT noted earlier was likely due to dawn cell focus proximity (see Figure 4.4a). This assumption also does not hold completely true towards the end of the event, between 08:30 UT and 08:45 UT in Figure 4.3, where there was significant increases of the plasma velocity without high magnitudes of B_z. We propose this is due to reverse forcing from the already disturbed neutrals at that time, otherwise known as the flywheel effect.

The neutral wind flywheel is a known source of induced ionospheric currents during otherwise quiet conditions (Lyons et al., 1985), and has also been shown to cause lingering fast plasma flows after active events such as substorms (Deng et al., 1991, 1993). The latter of these is what we believe occurs between 08:30 UT and 08:45 UT. Figure 4.6 shows three snapshots during this period, in the same format as Figure 4.4 but slightly before panel d. These are consecutive two-minute integration periods for the SuperDARN potential patterns, but they occur during one integration period from SCANDI, so the neutral winds shown are the same in each. Figure 4.3 shows that prior to this, the neutral velocity was increasing in the plasma direction, which we attribute to traditional ion-drag. At 08:30 UT (Figure 4.6a) however, the plasma convection in the observation region became complicated and included sunward flows, opposite to where the previously forced neutrals were heading. As the neutral particles held onto their previous inertia, the plasma was accelerated into the neutral direction without any additional IMF input (Figure 4.6b and c, then 4.4d). This kind of neutral wind feedback to the ionosphere,

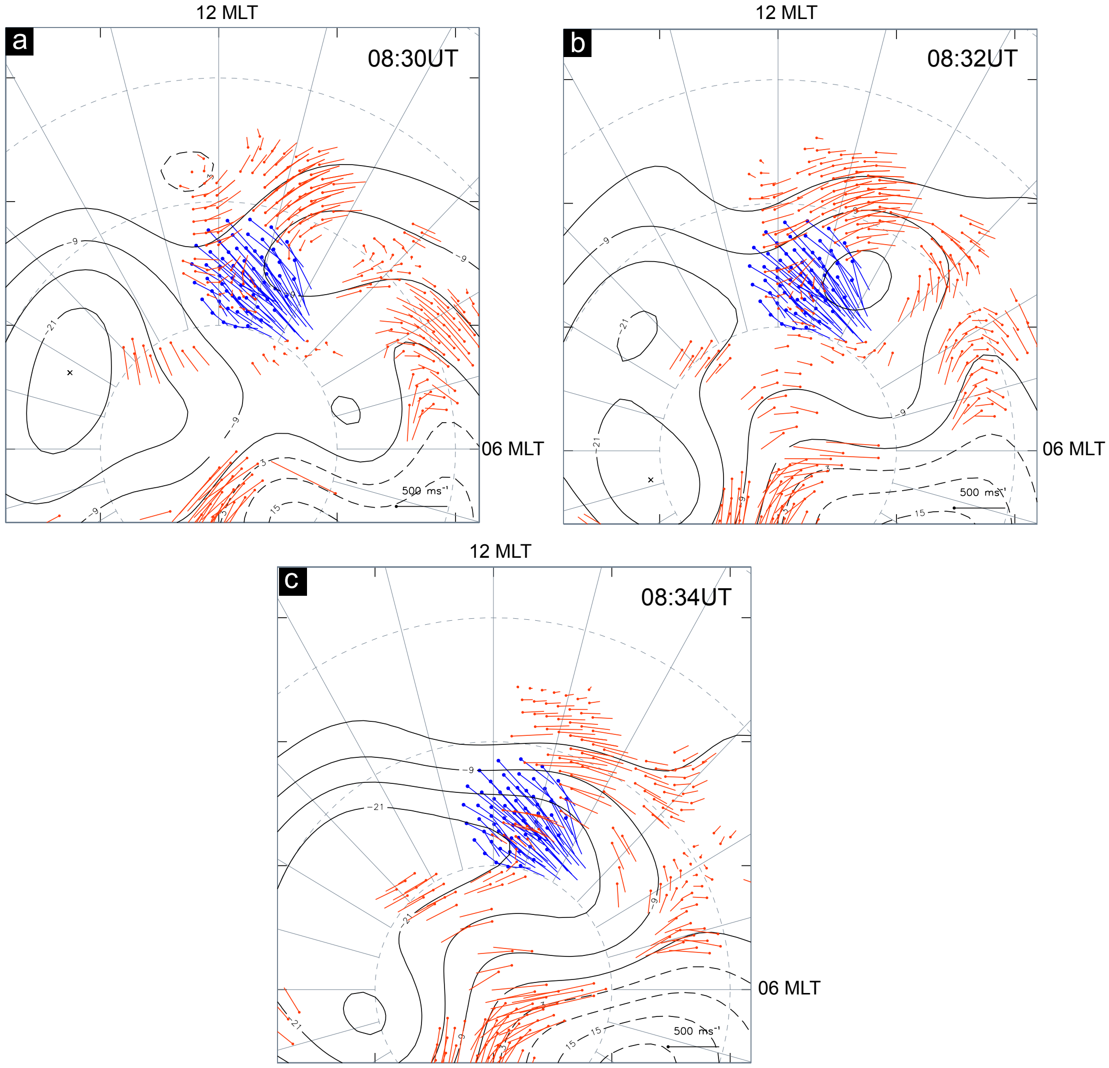

Figure 4.6: Same format as Figure 4.4, except showing three consecutive 2-minute SuperDARN potential patterns which fall within the same SCANDI integration period. The period shown is slightly before Figure 4.4d.

which we have seen here to be incredibly significant, is not usually considered a large source of ionospheric currents. It is however rising to prominance in its importance, for instance a recent study by Ferdousi et al. (2019) estimated that it accounts for an average 20% electric field enhancement after storm time conditions. For the rest of the event prior to the flywheel period, we assume there was little or no neutral wind forcing due to the low magnitude of the neutral winds in comparison to the plasma.

In terms of the response timescale of the neutral wind, an average of around 75 minutes for the entire event was determined within the FOV by the cross-correlation in

Figure 4.5. We now consider how this time varies between the different SCANDI zones, shown by the peaks of the coloured curves in Figure 4.5a and shading of 4.5b.

To begin, we examine why both the south-eastern and westernmost zones had a considerably different lag to that the rest of the FOV. The correlation curves for those zones (green and blue) have only slightly higher peaks at ∼-15 minutes than at -75 minutes, which illustrates a potential caveat of using this technique; the cross-correlation effectively can only give an average lag over the entire event. Thus, the peaks at -15 minutes imply that there was a period during the event of drastically reduced neutral wind response times in those zones which "contaminated" the cross-correlation. This could be due to an enhanced ion-neutral collision frequency, brought about by auroral precipitation ionisation. Indeed, between 07:30 UT and 08:30 UT, a series of poleward moving auroral forms (PMAF) occurred to the south of Svalbard along with bright auroral arcs (via Svalbard all-sky imager - not shown). This short period within the current event is in fact the subject of the preceding chapter, and follows the work of Conde et al. (2018) and Zou et al. (2018) in studying the effects of precipitation on ion-neutral coupling.

Besides the aforementioned zones, the neutral wind lag time varied between 67 and 97 minutes across the FOV. This is consistent with the previous studies mentioned above, i.e. similar results to both Joshi et al. (2015) and Heelis et al. (2002), whilst falling within the wide ranges given by Baron and Wand (1983), Killeen et al. (1984) and Kosch et al. (2001). However, this study offers new insights to how the delay varies over small spatial scales. Namely, that there is no discrete "jump" between neighbouring zones, but gradual transitions between longer and shorter times within the 67 to 97 minute range. Thus, thermoshere-ionosphere coupling strength does not change much over very small spatial scales (∼100 km), but does considerably over mesoscales of around 1000 km. Ultimately, this also implies a high degree of variation in the transfer of energy across mesoscales, which was alluded to in the previous chapter through the UT variation in the neutrals.

4.5 Summary

An event was identified which showed distinctive neutral wind responses to changes in the plasma velocity. A cross-correlation analysis was preformed to determine the time it took for the neutrals to finish accelerating due to the ion-drag force. The wide-view SCANDI FPI was used in accompaniment with SuperDARN to resolve spatial differences in this timescale. To summarise the main findings of this chapter:

- Across the ~1000 km FOV observed, nearly all spatially resolved locations (approximately 100 km apart) showed a neutral wind response time between 67 and 97 minutes.
- Thermospheric inertia (the neutral wind flywheel) after the subsidence of a high geomagnetic activity event can induce large residual ionospheric currents and electric fields.

Although we have averaged over several hours worth of local time, the timescale variations of up to 30 minutes during aurora-free conditions seen in this study are large. Yet, this study considered only a relatively small region of the thermosphere compared to the global extent by which ion-drag is important at high latitudes. Due to the lack of global neutral wind data products available currently, we must look to physics based models which can suitably handle neutral particle inertia and ion-drag contributions, such as TIEGCM, in order to shape our global understanding of thermospheric reconfiguration timescales.

As mentioned earlier, additional ionisation from auroral precipitation events has been shown to considerably reduce the neutral wind response time to plasma changes, and may have caused the few unusually short lag times within the cross-correlation analysis during this study. The following chapter is therefore a closer investigation of the latter part of this event, where a series of poleward moving auroral forms was seen above Svalbard. Along with velocity information from SuperDARN and SCANDI, ground based electron density height profiles and optical F-region auroral intensities were both coincidently available above Svalbard. This allowed the precipitation influence on ion-neutral coupling to be examined for the very first time sunward of the magnetic pole.

Chapter 5

Ion-Neutral Coupling during during an interval of Transient Aurora in the Dayside Cusp Region

The following chapter contains work from the article currently under review:

Billett, D. D., Hosokawa, K., Grocott, A., Wild, J. A., Aruliah, A. L., Ogawa, Y. & Taguchi, S. (2019). Multi-instrument Observations of Ion-Neutral Coupling in the Dayside Cusp.

During this study, KH, AG and JAW acted as academic supervisors. ALA, YO and ST assisted with data acquisition, interpretation and useful discussion.

5.1 Introduction

In the previous chapter, an event was presented that showed the neutral thermosphere responding fully to changes in the ionosphere within 67-97 minutes. During this reconfiguration time, momentum transfer between the neutrals and plasma, and thus Joule heating, will have been enhanced due differences in the motions of the ionosphere and neutral thermosphere (as shown in chapter 3).

From the Joule heating equation (Eq. 1.46) we can see that the Pedersen conductivity is an important scaling factor in each term. So typically, conductivity enhancements (whether that be through EUV ionisation or particle precipitation) would be expected to simply increase Joule heating. However, studies have shown that the large increase of ion-neutral collisions due to precipitation enhanced ionisation drastically decreases the thermospheric response timescale - anomalously decreasing Joule heating. These studies have so far been confined to nightside observations, but due to the high-latitude location of the SCANDI FPI, dayside observations are possible during the polar night. In this chapter, we examine a period of time near magnetic noon where there were observations of poleward moving auroral forms, a phenomenon which only occurs near the dayside cusp region. Here, the plasma also responds the most quickly to changes in solar wind driving through magnetopause reconnection - offering an ideal opportunity to closely examine the nature of magnetosphere-ionosphere-thermosphere coupling using high spatio-temporal resolution data. Together with SuperDARN and SCANDI, the EISCAT Svalbard Radar (ESR) and an all-sky imager (Svalcam) allow the additional calculation of the F-region Joule heating rate using an estimation of the Pedersen conductivity. This includes the contribution to Joule heating directly resulting from changes to ion-neutral coupling.

5.1.1 Particle Precipitation and its Influence on Ionosphere-Thermosphere Coupling

Auroral processes have been thought to be associated with neutral wind disturbances for some time. For instance, Spencer et al. (1982) used DE2 spacecraft data to observe much faster neutral wind flows in the auroral regions (compared to at lower latitudes), whilst Killeen et al. (1988) additionally used DE1 to show that neutral wind shears and boundaries aligned consistently with plasma flow in auroral arcs. In contrast to these global scale observations, Conde et al. (2001) saw similar behaviour using a ground-based scanning Doppler imager (SDI), but with a much more complex mesoscale structure

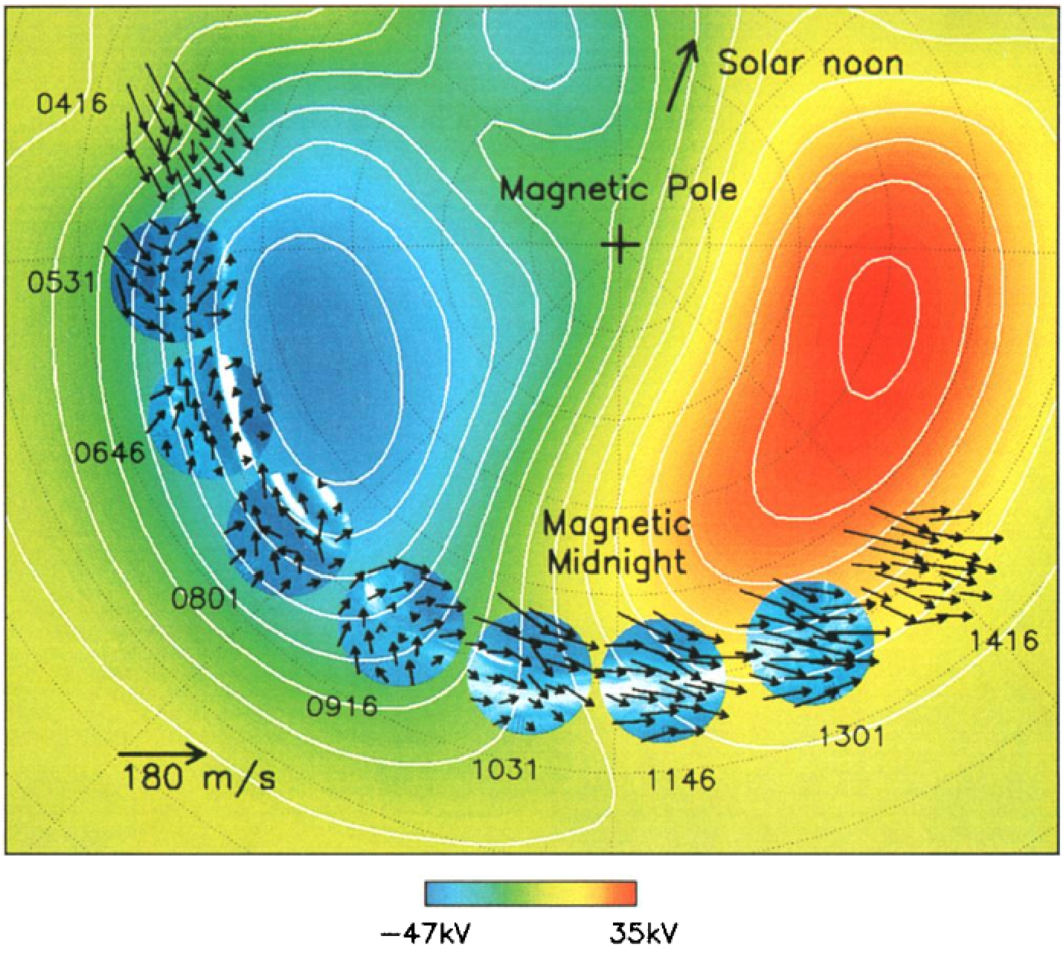

FIGURE 5.1: Summary wind dial plots from Conde et al. (2001), showing the evolution of the F-region neutral winds above Alaska on February 10th, 1997. Underlain on each wind dial is an all-sky auroral image, and a Weimer (1995) statistical plasma convection pattern is shown in white contours/rainbow colour scale for context.

(∼100 of kilometres in the F-region) than previously thought. An overview of that event can be seen in Figure 5.1, which shows the time evolution of the F-region neutral wind with underlain auroral all-sky images and a statistical Weimer (1995) plasma convection pattern. This study, for the first time, revealed observationally a time-lagged response of the neutral wind to changes in ion-drag forcing within auroral arcs, which is particularly evident between 05:31 UT and 08:01 UT, as well as between 09:16 UT and 10:31 UT. Note that the background plasma convection pattern shown was to give statistical context, and not meant to represent the complex mesoscale structure of the plasma.

During periods where the plasma density is low, the coupling time of the thermosphere to changes in the ionosphere is expected to be longer than where it is high. For instance, ion-drag is generally weaker during solar minimum versus solar maximum, nightside versus dayside, and winter versus summer. This is simply due to enhanced collisions as a result of greater ion density, and thus momentum transfer between the neutrals and plasma. In the comprehensive review by Smith et al. (1988), it is noted that this would also apply to regions within the auroral zone where particle precipitation ionisation forms the auroral oval - causing timescales that could be “frequently less than 50 minutes”. In the previous chapter, where the event was mostly devoid of aurora and during the hemispheric winter, timescales of 67-97 minutes were seen. However, it was alluded to that some exceptionally quick times seen in the cross-correlation analysis may have been the result of auroral activity towards the end of the event.

Recently, Zou et al. (2018) and Conde et al. (2018) have both offered multi-instrument observations of this kind of aurorally enhanced ion-neutral coupling on the nightside using SDIs. Both noted exceptionally fast and structured responses, under 20 minutes and on spatial scales down to $\sim$100 km. This has large implications for the way heat is dissipated into the atmosphere, as well as the global scale trajectories of neutral air parcels (e.g. Dhadly and Conde 2017). Namely, if energy propagating down into the ionosphere from the solar wind cannot be released as Joule heating, then it must find another output in auroral heating when the ionosphere and thermosphere are strongly coupled.

5.1.2 Poleward Moving Auroral Forms

Poleward moving auroral forms (PMAF) are the signature of pulsed reconnection in the dayside magnetosphere (approximately 10s of MWb of flux transferred at a time (Fear et al., 2017)), and are a common feature of the ionospheric cusp (Fasel et al., 1994). As their name would suggest, they are characterised by bright bands of aurorae originating in the dayside auroral zone, which then split off and migrate poleward before fading. Under IMF B_z<0 conditions, magnetopause reconnection leads to PMAF near noon

MLT, whilst under IMF B_z>0 and a strong IMF B_y, reconnection in the lobes causes PMAF both pre-noon (B_y>0) and post-noon (B_y<0) (Xing et al., 2012).

As PMAF are effectively just a rapid flow of plasma, it can be observed by HF ionospheric radars such as SuperDARN (e.g. McWilliams et al. 2000). This also means that it will exert ion-drag on the neutrals near the cusp. In this location, ion-drag typically already acts poleward as that is the usual orientation of the plasma convection in that region. But as we know from the auroral influence on the neutrals, and the fact that PMAF are often much faster than the usual convection (Milan et al., 1999), we might expect exceptionally strong ionosphere-thermosphere coupling near the cusp during a PMAF event. This is a particularly interesting region of the ionosphere, because it is the fastest to respond to a change in the IMF orientation. The potential for strong ion-neutral coupling in the cusp might therefore generate a pseudo direct coupling of the thermosphere to the magnetosphere.

5.2 Observations

An overview of the latter part of the event from the previous chapter is shown in Figure 5.2. From top to bottom, the panels show the IMF B_z and B_y components, a 630 nm intensity keogram, the ESR electron density altitude profile along the 42 m field aligned dish, and the average zonal (positive east) and meridional (positive north) neutral and plasma velocities in the SCANDI FOV (below 76° MLAT). Two ESR experiments were in operation during this period, separated by the data gap at around 07:00 UT. From the beginning until 06:57 UT, this was the 30 s integration “Beata” mode, and from 07:11 UT onwards was the 60 s integration “Taro” mode. The emission altitude of the 630 nm data is approximately 250 km, and it was chosen to average the velocity data only below 76° to match the region where the auroral activity was seen in the keogram.

The PMAF were first observed in the 630 nm keogram around 07:30 UT (10.4MLT) under southward B_z and positive B_y. B_z turned northward briefly after PMAF onset for 15 minutes before turning southward again, but there was no discernable impact on the PMAF. Before this activity, the main auroral oval was equatorward of SCANDI.

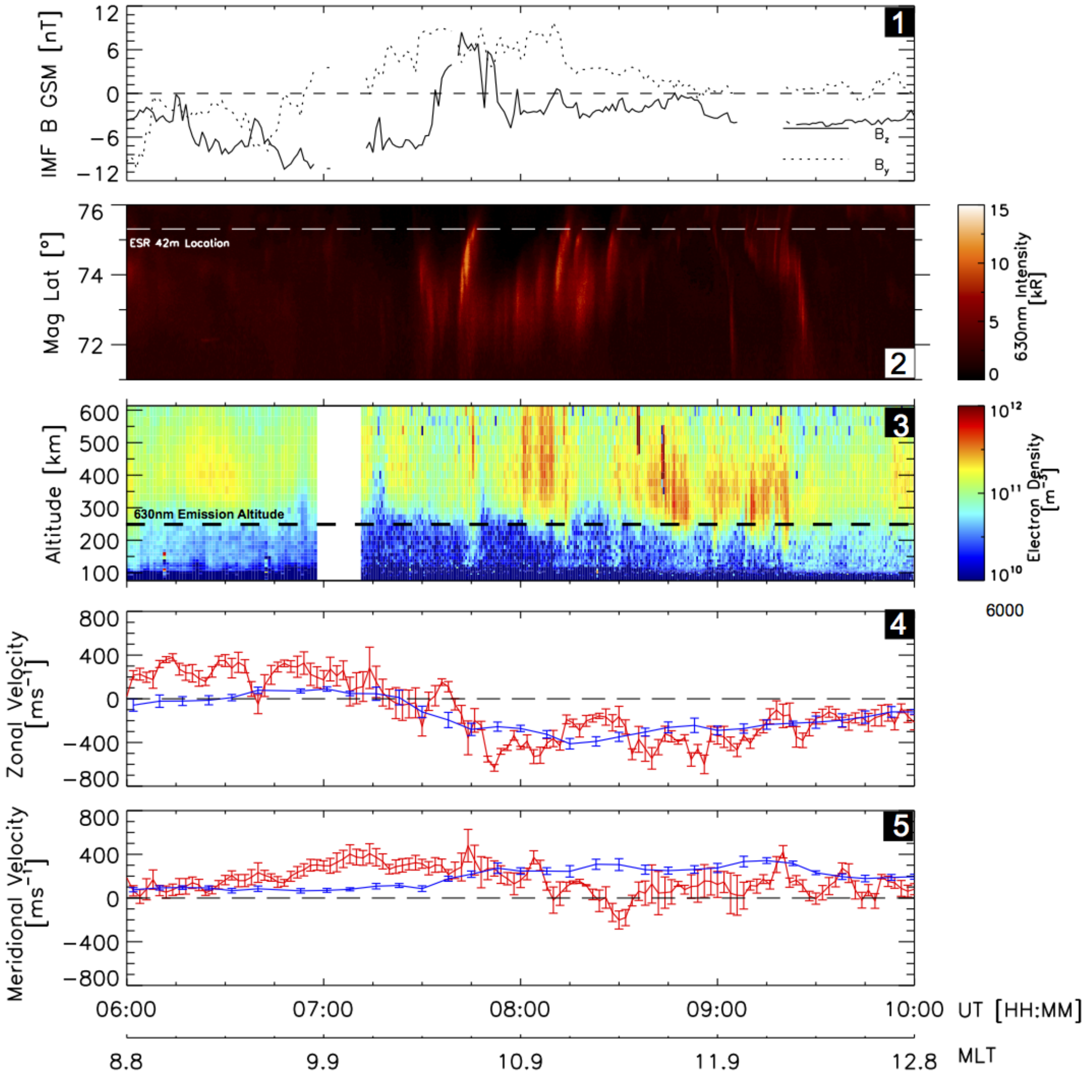

FIGURE 5.2: An overview of the event occurring on the 8th December, 2013. 1: IMF data (taken from the OMNI dataset and lagged to the ionosphere). 2: 630 nm intensity emission keogram (N-S) measured by Svalcam. 3: Electron density altitude profile from the ESR 42 m beam. 4: Average zonal and 5: meridional plasma (red)/neutral (blue) velocity components within the SCANDI FOV below 76°MLAT, measured by SuperDARN and SCANDI respectively. The dashed line on panel 2 indicates the latitude where the ESR 42 m beam lies, mapped to 250 km in altitude (approximate red line emission altitude). This altitude is also shown for context in panel 3 by the black dashed line. Error bars on 4 and 5 are standard deviations. Note that the integration time of the SuperDARN data was two minutes, whilst it was approximately 7.5 minutes for SCANDI.

Characterising the PMAF were bright and short lived poleward travelling enhancements of the emission between 71° and 76° MLAT, separated by slightly dimmer aurorae which migrated poleward much more gradually (e.g. between 07:45 and 08:15 UT). After the

PMAF end, the magnitudes of both B_z and B_y are reduced, and the main auroral oval sat at approximately 75° MLAT. There was a further bright auroral enhancement at 09:00 UT, and then again at 09:30 UT.

The ESR electron density (n_e) height profiles show the ionising effect of the particle precipitation that led to the PMAF and other aurorae. Initially when the sky was dark (06:00-07:30 UT), n_e did not vary much with time above 300 km, and most of the ionised atmosphere was above 200 km. Then, after the PMAF began, there were very large enhancements of n_e between 100 and 600 km whenever the aurora passed the ESR FOV. Increased ionisation was maintained after the PMAF until 09:20 UT, whilst the main auroral oval was directly in the ESR beam FOV.

At the start of this event, the plasma flow was eastward with a slight poleward component. Upon the B_y transition from negative to positive just before 07:00 UT, the plasma began to rotate in the westward direction (zonal velocity transition from positive to negative) and gained a large amount of poleward momentum, accelerating from $\sim$100 to $\sim$300 ms^{-1}. The neutrals comparatively started very slow in both components. Zonally, they began westward and accelerated eastward into the plasma direction, peaking around 07:00 UT at $\sim$100 ms^{-1}, before starting to turn westward with the plasma. Meridionally, the neutrals initially maintained a slow poleward velocity before starting to accelerate further poleward in the plasma direction just after 07:00 UT.

After the PMAF began, the plasma was still accelerating westward. From about 07:50 UT onwards, it stopped accelerating and remained consistently westward for the rest of the event. The meridional component of the plasma however was much more variable, as shown by the spread of standard deviations increasing. On average, the plasma slowed in the poleward direction from 07:45 UT until the end of the event. Within minutes of the aurora onset the neutrals accelerated meridionally from $\sim$100 to $\sim$300 ms^{-1} to match the plasma velocity, whilst staying at a very close velocity to the zonal plasma velocity. Both components of the neutral wind remained fast for the duration of the aurora; continuing to stay close in speed to the plasma zonally, and remaining at a constant 300 ms^{-1} meridionally as the plasma slowed.

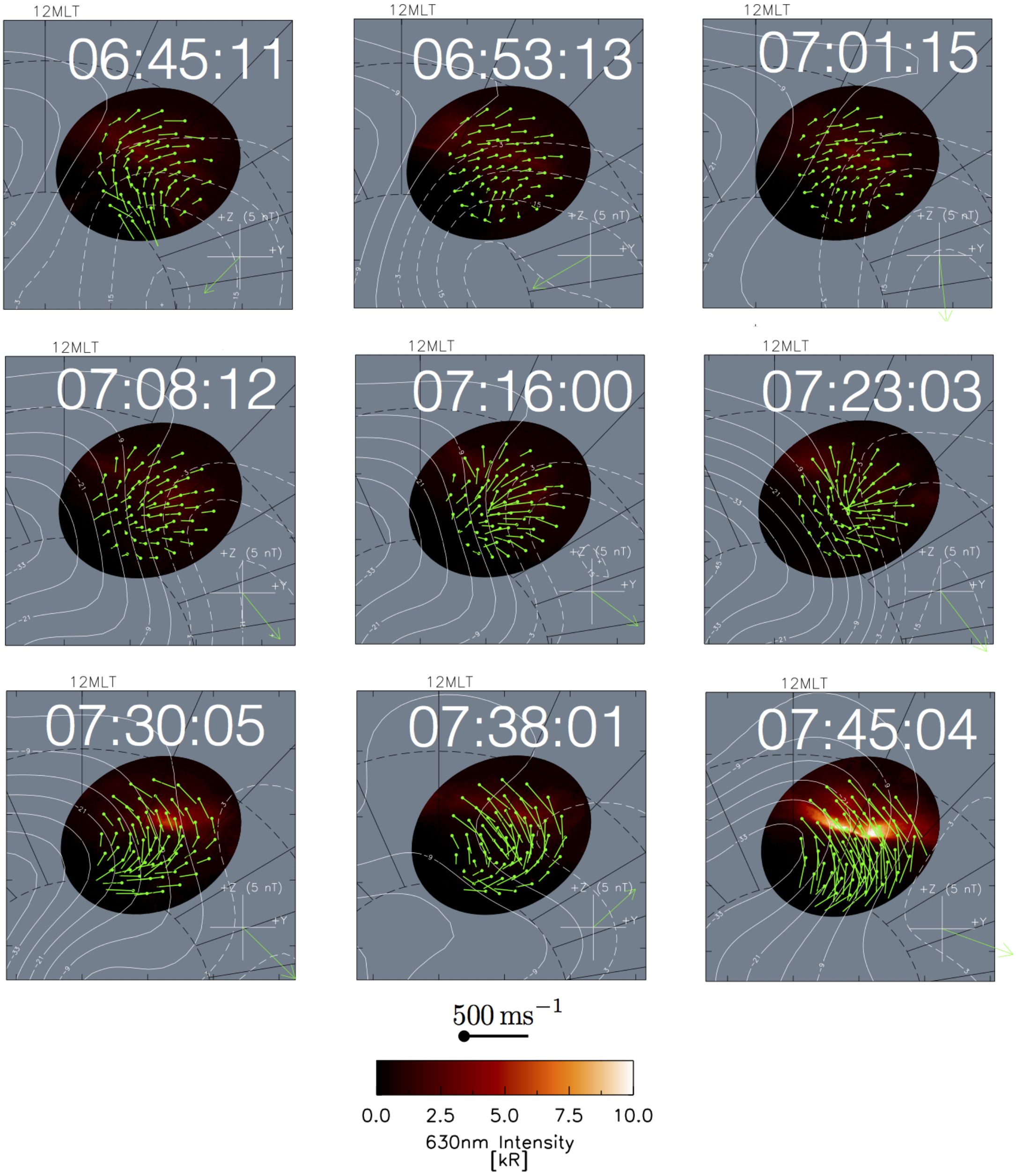

Figure 5.3: MLAT-MLT format plots of neutral winds, 630 nm intensities and plasma convection contours above Svalbard before and during the PMAF shown in Figure 5.2. The vectors and intensities have been mapped to an altitude of 250 km, and the IMF clock angle is shown in the bottom right of each for convenience.

Nine successive 2D MLAT-MLT snapshots, covering one SCANDI integration time each, are shown in Figure 5.3 for the period between 06:45 UT and 07:45 UT. This covers the time slightly before the IMF B_y transition, a period of no aurora, followed by the onset of the PMAF. Green vectors are the neutral wind velocities measured by SCANDI, whilst underlain is the 630 nm emission and SuperDARN plasma convection contours for that exact time.

As seen by the averaged velocity data in Figure 5.2, the plasma convection in the SCANDI FOV turned from eastward to westward flow quickly after the IMF B_y transition from negative to positive (between 06:53:13 UT and 07:08:12 UT). Following this, the neutral wind over the entire FOV broadly maintained an eastward velocity, but the most equatorward vectors showed signs of turning into the convection as early as 07:16:00 UT. During the integration period starting at 07:23:03 UT, a few more of the neutral vectors had turned, although most were still in disagreement with the plasma flow direction. As the first burst of PMAF starts in the 07:30:05 panel, neutrals over the entire FOV then re-orientated and gained a large poleward velocity within the subsequent ∼8 minutes. In this region the plasma convection was mostly oriented as before. For the last two panels, the region observed by SCANDI moved further into the dusk convection cell, where plasma on the equatorward side was significantly eastward (07:45:04 UT). The neutrals continued to follow the plasma convection contours closely, maintaining a fast poleward velocity.

5.3 Discussion

An event has been presented here which shows two very different states of ionosphere-thermosphere coupling. The first, before the PMAF began at 07:30 UT, is a weak state of coupling where the neutrals take several tens of minutes or longer to be accelerated fully by the plasma. The second state, during the course of the PMAF as well as the subsequent aurorae, is where ion-drag is exceptionally strong. Within minutes of the auroral activity starting, the neutrals accelerate quickly into the direction of the plasma, where before they were far more sluggish. The onset local time of the PMAF is consistent with lobe reconnection for IMF B_y>0 (Xing et al., 2012), and the auroral features around 09:05 UT and 09:25 UT are signatures of “throat aurora” (which has recently been the subject of numerous studies; e.g. Han et al. (2017)).

During the weak coupling period, the ion-drag response of the neutrals is still evident. At the approximate emission altitude of the 630 nm intensities and SCANDI red line emission ($\sim$250 km), the ESR measured electron density (Figure 5.2, panel 3) is low compared to when aurora crosses the FOV later on. It is a reasonable assumption that this relationship extends to the entire SCANDI FOV, as the spatial extent is small. The ionospheric plasma density above Svalbard during this period, and thus the ion-neutral collision frequency, was therefore low. This is evidenced by the fact that the meridional component of the neutrals (Figure 5.2, panel 5) did not significantly speed up in the plasma direction until there was a large velocity gap around 07:00 UT. This can also be seen in Figure 5.3, as the neutrals start to turn poleward from 07:01:15 UT onwards. There was already a considerable velocity difference zonally (Figure 5.2, panel 4) as the event started, hence the gradual but consistent neutral wind response (between 07:08:12 UT and 07:23:03 UT in Figure 5.3). The neutral wind response time during this period is expected to be as calculated in the previous chapter, between 67 and 97 minutes.

Because of the rapid response of the neutral wind after the PMAF onset at 07:30 UT, it is also a reasonable assumption that the cause was enhanced ion-neutral collisions due to increased plasma density. As this period of high momentum exchange began, a $\sim$300% increase in meridional neutral velocity to roughly match that of the plasma occurred within 15 minutes (07:30:05 UT-07:45:04 UT in Figure 5.3). In the zonal direction, the plasma was transitioning from eastward to westward (which is the expected behaviour in the convection throat region; e.g. Rash et al. (1999)) and closely pulled along the neutrals with it with very little apparent lag (07:23:03 UT-07:30:05 UT). The lack of a delay here is possibly because the neutrals and plasma already had a similar zonal velocity when the PMAF started, meaning very little force was required to bring the neutrals in line with the plasma. Although the B_y dependence on the high-latitude convection is well understood (e.g. Ruohoniemi and Greenwald 1996), the neutral wind dependence is less so. McCormac et al. (1991) for example first observed a dawn-dusk asymmetry in successive passes of the DE2 spacecraft, and a dependence was seen statistically by Forster et al. (2008). This is however the first time an IMF B_y transition has been seen to occur in the neutral wind during a single observation period, which is in part due to proximity to the cusp and the occurence of PMAF.

As their name would suggest, poleward moving auroral forms enhance the plasma velocity in the poleward direction, but this is not completely captured when averaging all the plasma vectors in Figure 5.2, panel 5 from 07:30 UT onwards. This is likely an artifact of averaging many vectors travelling in different directions, and indeed, both the widening standard errors on the mean and the 07:38:01 UT panel in Figure 5.3 confirm this was probably the case. The convection where the PMAF occured, at both 07:30:05 UT and 07:45:04 UT in Figure 5.3, was strongly anti-sunward as expected.

Whilst the PMAF carried on, and afterwards when they ceased but other auroral activity is within the FOV, the neutrals remained at around the plasma velocity zonally and remained fast in the poleward direction. Even though ESR data show there was indeed ionisation after the PMAF, it would have been confined to a relatively thin parallel of constant latitude. Therefore, ion-drag might not necessarily have been strong throughout the entire SCANDI FOV. Due to the inertia of the neutral wind however, and the fact that it was already enhanced westward, very little ion-drag forcing would have been required to keep the neutral wind flowing with the plasma zonally. The meridional component of the neutrals however remained consistent during the brief period of northward IMF B_z where the convection pattern distorted (Figure 5.3, 07:38:01 UT), which again is due to the inertial properties of the thermosphere (or neutral wind flywheel; Lyons et al. (1985)).

5.3.1 Joule Heating

As we have seen in chapter 3, neutral winds can play a significant role in modulating Joule heating in the Earth's upper atmosphere. As before, the height integrated Joule heating rate for a specific altitude range can be calculated as:

$$\Sigma Q_j = \underbrace{\Sigma_P E^2}_{Q_c} + \underbrace{2\Sigma_P \mathbf{E}\cdot(\mathbf{u}\times\mathbf{B}) + \Sigma_P\left(\mathbf{u}\times\mathbf{B}\right)^2}_{Q_w} \tag{5.1}$$

where **E** is the convection electric field, **u** is the neutral wind velocity, **B** is the magnetic field, Σ_P is the height integrated Pedersen conductivity, and Q_c and Q_w are the convection heating and wind correction terms, respectively, described in more detail in section 1.4. In this study, velocity data for both the neutrals and plasma (and hence, electric field) are available, whilst **B** is modelled well by the IGRF (Thébault et al., 2015). The only thing directly unavailable is the Pedersen conductivity. Contrary to chapter 3, statistical models would not be suitable to use here as they do not capture the auroral variability of PMAF in any way, and so can't represent its effect on the Joule heating rate accurately. In this subsection of the chapter, we will describe how this limitation was overcome using the 630 nm all-sky intensity images, as well as present estimates for the F-region integrated Joule heating.

5.3.1.1 Determination of the F-region Integrated Pedersen Conductivity

Alternatively to the derivation shown in section 1.1.2.1, the Pedersen conductivity can be given by:

$$\sigma_p = \frac{en_e}{B}\left(\frac{w_{gi}\nu_{in}}{w_{gi}^2 + \nu_{in}^2}\right) \tag{5.2}$$

where e is the elementary charge, n_e is the electron density, w_{gi} is the ion gyrofrequency and ν_{in} is the ion-neutral collision frequency. The height dependent n_e and B can be determined from the ESR data and IGRF respectively, whilst ν_{in} is calculated using the relation from Brekke (2012):

$$\nu_{in} = 4.34 \times 10^{-16} n\left(N_2\right) + 4.28 \times 10^{-16} n\left(O_2\right) + 2.44 \times 10^{-16} n\left(O\right) \tag{5.3}$$

where $n\left(N_2\right)$, $n\left(O_2\right)$ and $n\left(O\right)$ are the densities of molecular Nitrogen, Oxygen and atomic Oxygen respectively, which are obtained from the NRLMSISE-00 model (Picone et al., 2002). Finally, the value of the ion gyrofrequency is taken as that calculated by Hosokawa and Ogawa (2010).

Using this process allows us to determine height profiles only along the FOV of the ESR beam, which can then be integrated over the altitudes in the F-region where it is assumed the neutral winds do not vary significantly (200-300 km; Aruliah et al.

(1999)) to get a value for Σ_P. These are however only point measurements for a certain ESR integration period, but a process can be used in order to extrapolate out to a 2D conductivity field, based on the auroral intensity. This is because in the F-region, the 630 nm auroral emission is roughly proportional to the rate of ion production (Kosch et al., 1998), which is then also proportional to the conductivity (Brekke and Moen, 1993) and electron density (Oyama et al., 2013). Thus, we may then assume the electron density measured by ESR is directly proportional to the 630 nm intensity measured by Svalcam. Recently, Lam et al. (2019) has shown this to be a reasonable approximation.

Using this assumption for the event presented in this study, the 630 nm images were initially averaged to match the integration lengths of the ESR data (30 s and then 60 s for the two modes used). Then the value of Σ_P (calculated using the aforementioned process) was matched with a corresponding 630 nm intensity at the ESR location for each timestep, and a linear fit to all the data preformed. The results of this are shown in Figure 5.4, and the equation of the fit with a reduced chi squared of $\chi^2_\nu = 1.6948$ is:

$$\Sigma_P = 0.0504 + \left(I \cdot 2.5276x10^{-5}\right) \tag{5.4}$$

where I is the 630 nm intensity. It is this fit that we use in this study to get Σ_P at all locations where the Svalcam and SCANDI FOV's overlap. It should be noted that the purpose of this is not to precisely calculate the F-region integrated Pedersen conductivity, as it is clear there is a non-trivial amount of spread in the intensity-conductivity relationship (as well as a high value of χ^2_ν). Most importantly, it is needed to capture the precipitation-enhanced conductivity both spatially and temporally within the correct order of magnitude, which we argue is more important for this study.

5.3.1.2 2D Joule Heating Maps

Figure 5.5 shows the calculated F-region integrated Joule heating rate using the above process and Eq. 5.1, in the same format as Figure 5.3. Because the Pedersen conductivity is much smaller in the F-region than the E-region, so is the amount of Joule heating

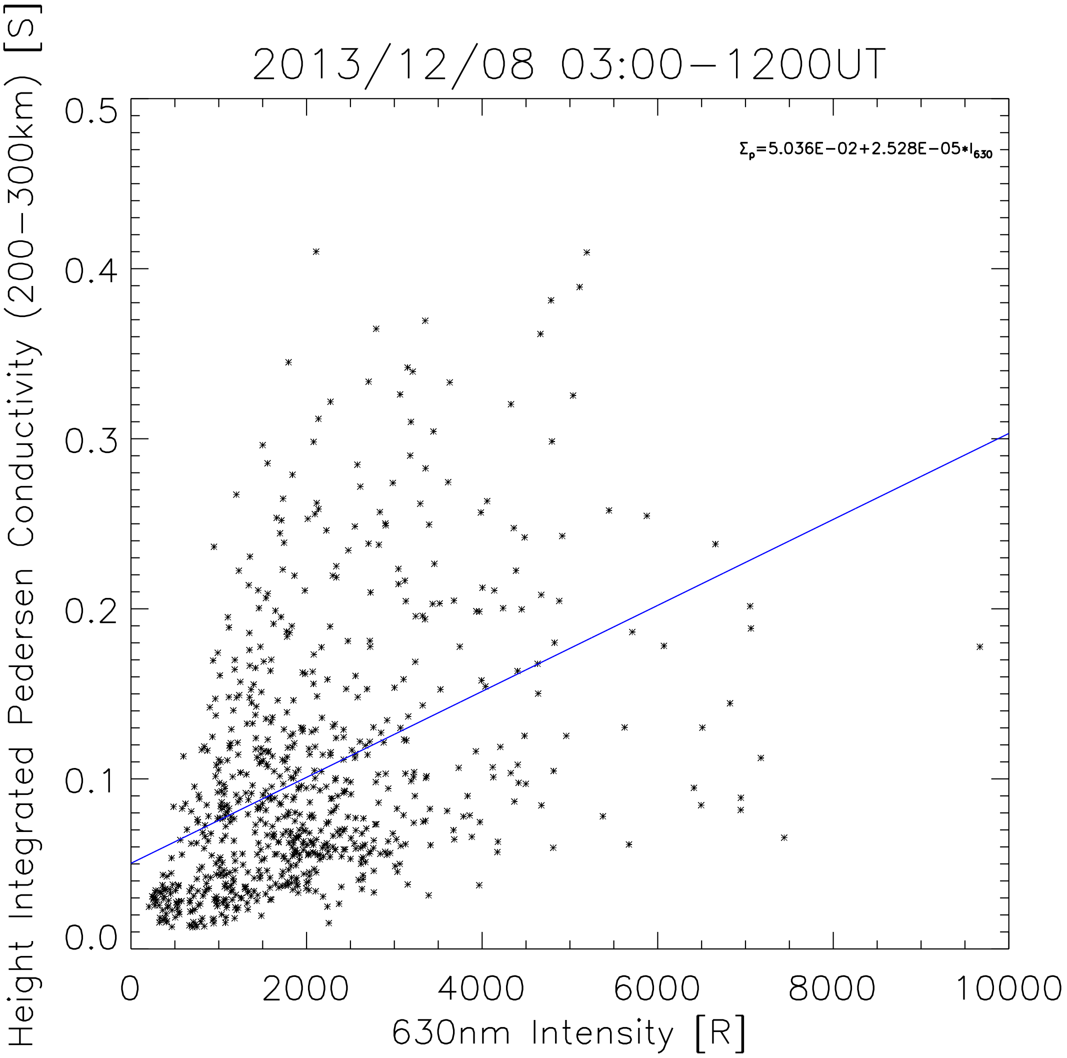

FIGURE 5.4: F-region integrated Pedersen conductivity (between 200-300 km, calculated using ESR data) vs 630 nm auroral intensity (measured by Svalcam) for the event occurring between 06:00 UT and 10:00 UT on the 8th December, 2013. The blue line is the linear fit to the data, which has a reduced chi squared of $\chi^2_\nu = 1.6948$.

in general. The variability of the F-region Joule heating rate is however still analogous to the E-region rate, although owing to greater ion-neutral collision frequencies, precipitation ionisation probably has a greater influence in the latter (Zou et al., 2018).

Certain Joule heating enhancements in Figure 5.3 can be easily attributed to strong electric fields, for example, at 07:08:12 UT, 07:16:00 UT and 07:23:03 UT where the contours of electric potential were close together in the convection throat. Other enhancements coincide with PMAF bursts, such as those at 07:30:05 UT and 07:45:04 UT, which

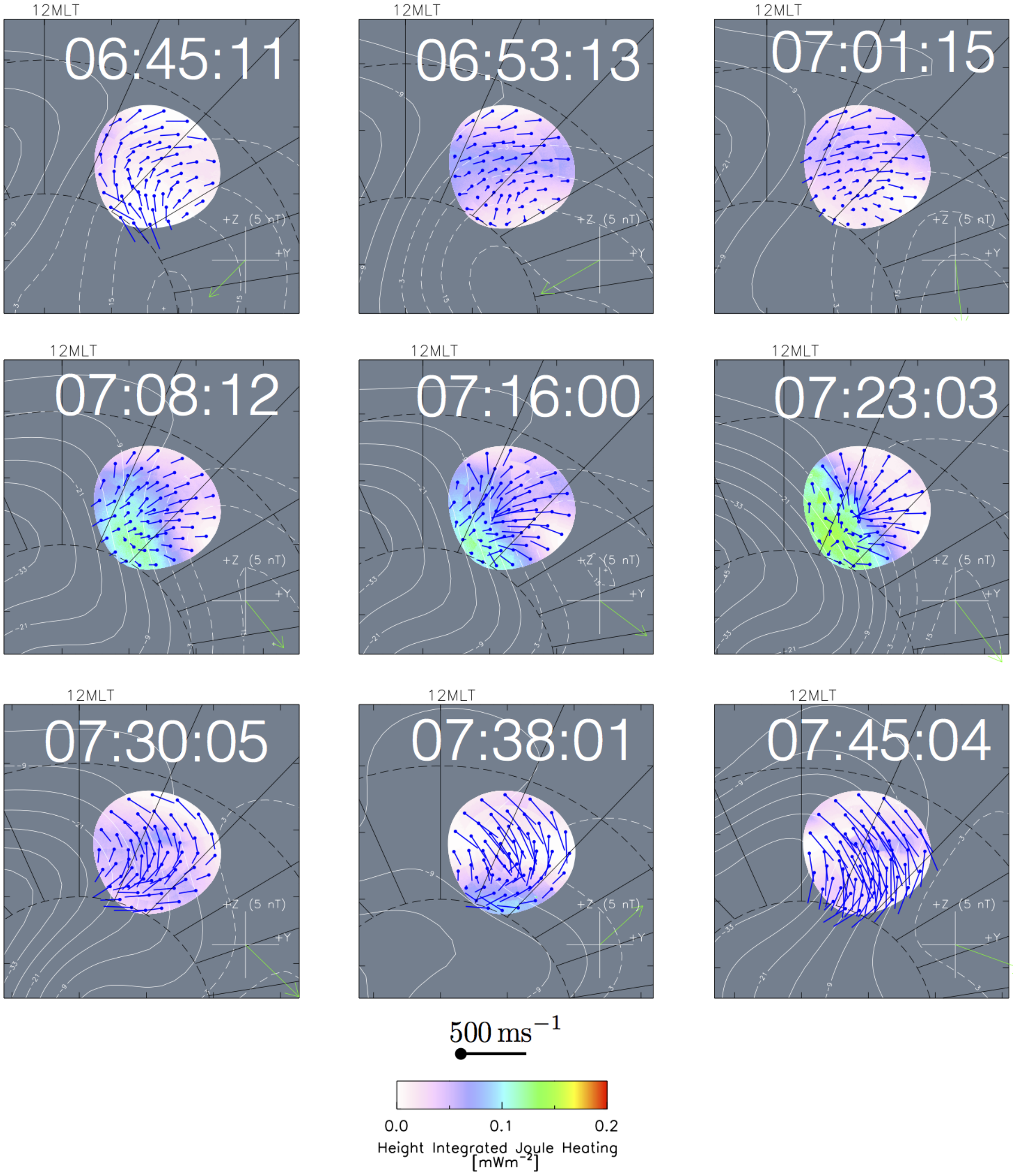

FIGURE 5.5: Same format and times as Figure 5.3, but showing the F-region integrated Joule heating rate.

lie roughly in the centre of the FOV. What is particularly interesting however is the contributions of the neutral winds, which in this case is a direct measure of how coupled the ions and neutrals are at any given time.

At 07:30:05 UT and 07:45:04 UT, Joule heating was surprisingly small considering that the Pedersen conductance (enhanced from the PMAF; see Figure 5.3), and to an

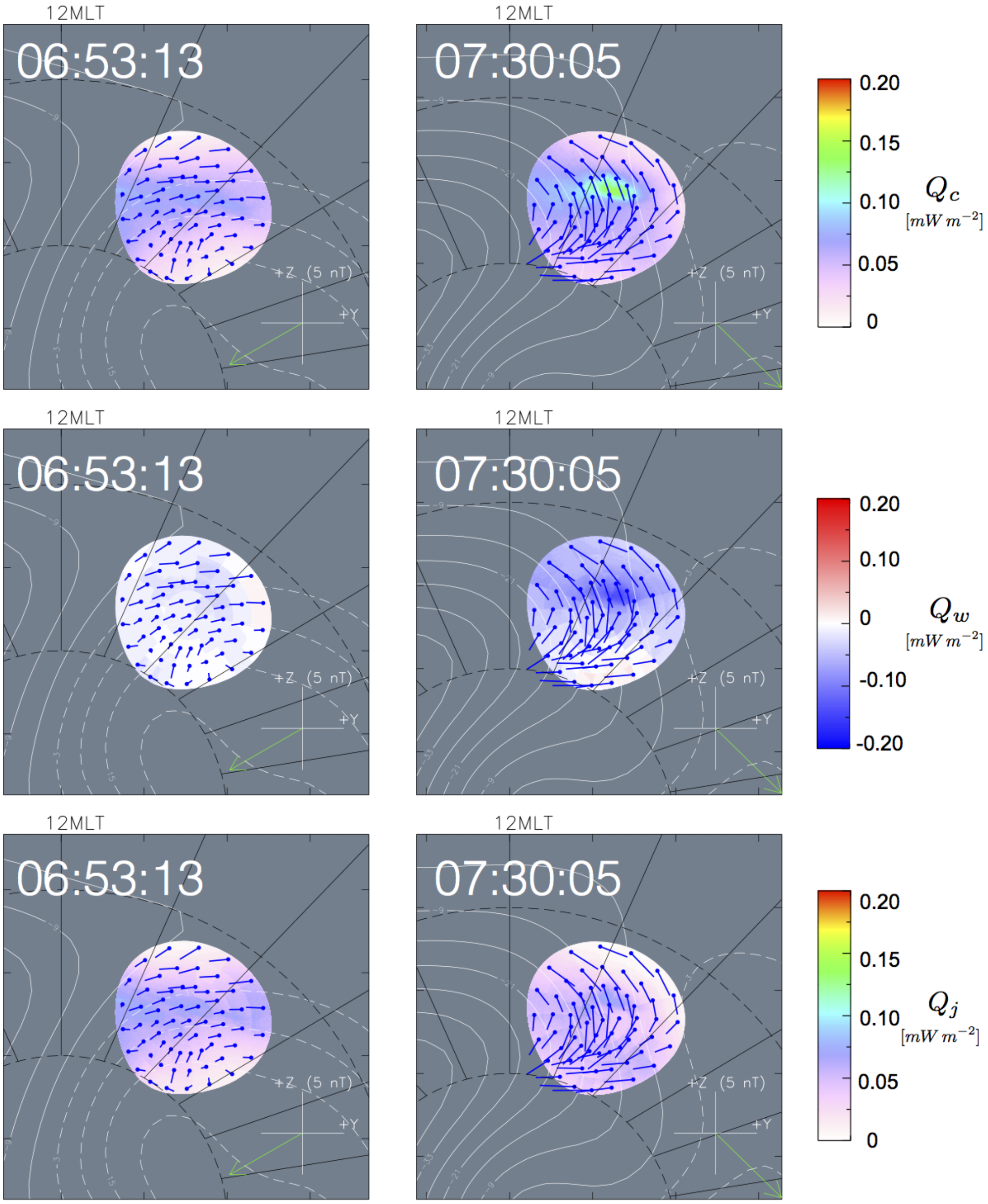

FIGURE 5.6: Same format as Figure 5.5, except showing only two times as well as the Q_c and Q_w components.

extent, the electric field, was high. To show what is occurring here, in Figure 5.6 we present the Q_c, Q_w and Q_j terms from Eq. 5.1 for two times, before and after the PMAF begin. At 06:53:13 UT, which is before the B_y transition, there was no aurora and so Q_c was controlled by the electric field. Q_w at that time was only very slightly negative because the neutrals flowed slowly in the plasma direction, thus the total Joule heating (Q_j) was essentially the same as Q_c. At 07:30:05 UT, right as the first PMAF burst occurred, Q_c was strongly enhanced due to the high auroral conductivity. Due to ion-neutral alignment however, the strong Q_c heating is nearly entirely negated by Q_w. This presents a very unique consequence of precipitation enhanced ion-neutral coupling; because it is strengthened so significantly following auroral onset, the Joule heating rate that would be assumed based on the high conductivity ends up being a large overestimation. We have illustrated here that at least in the F-region, the neutral wind can be a critical factor in Joule heating estimations.

5.4 Summary

Ion-neutral coupling and its consequences for Joule heating during an event of poleward moving auroral forms has been presented. It was found that before and after the precipitation began, the level of interaction between the ionospheric convection and thermospheric neutral winds was very different. To summarise:

- Neutral wind response times to changes in the plasma motion are drastically reduced to the order of minutes during auroral activity compared to a prior quiet-time interval. This is in agreement with recent studies by Zou et al. (2018) and Conde et al. (2018).
- The rapid neutral wind response appears to be a result of enhanced plasma density from the precipitation ionisation, as seen in conjunct ESR measurements.
- Because these observations were made near the dayside cusp and during a transition of the IMF B_y component, we observe for the first time a rapid response of the neutral wind directly relating to changes in solar wind driving during a single observation period.
- Neutral winds can act to severely moderate Joule heating in this scenario, nearly eliminating the heating that would otherwise be expected in high electric field or high conductivity regions.

It should be noted that the integration time of the FPI used in this study, SCANDI, is comparable to or indeed longer than the length of a single PMAF burst. Therefore, the shortest time we can confidently say the neutrals fully responded after the PMAF started is approximately 7.5 minutes, but it could be even faster than that. We have also shown that a lot less energy can be imparted to the neutral atmosphere through Joule heating than might be expected, as the thermosphere acts as a momentum dampener in aurorally active regions.

Chapter 6

Conclusions

In this thesis, several aspects of ion-neutral coupling in the high latitude thermosphere, and its influence on the rate of Joule heating being deposited into the atmosphere, have been studied.

In Chapter 3, plasma data from the Super Dual Auroral Radar Network (SuperDARN) was used with the Horizontal Wind Model 14 (HWM14) to statistically calculate Joule heating for the entire northern hemisphere, and categorise the patterns by season, geomagnetic activity level, and UT. Although plasma convection is not strongly controlled by UT, neutral winds exhibit a UT dependence due to varying degrees of solar irradiance on the magnetic polar cap, and it was found that Joule heating too varied with UT as a result.

This variation can be quite significant, accounting for as much as a 20% difference between minimum and maximum hemispheric integrated Joule heating rates during a single day. In terms of how the morphology of Joule heating changes, the most drastic changes occur on the duskside for all seasons and activity levels; that being, a switch from the neutral winds reducing Joule heating to increasing it for a few hours in the middle of each day. This is because statistically, the diurnal tidal motion of the thermosphere pushes a neutral wind dusk cell (a product of ion-drag) through the space of the dusk plasma convection cell, creating regions and times where the neutral winds do not align with the plasma and generate more friction.

During the summer months when the solar ionisation induced conductivity is high, and during high geomagnetic activity when plasma convection is fast, the neutral winds most often act to decrease Joule heating because they are more aligned with the flow of the plasma than in the winter. This is probably due to a stronger ion-drag force under those conditions, which is moderated by thermospheric ionisation rates (i.e. the ion-neutral collision frequency) and the plasma-neutral velocity difference. During winter months on the other hand, the conductivity is much lower and does not overwhelm the contribution from the neutral winds as much as in the summer, meaning they matter more in deciding Joule heating rates.

In Chapter 4, a closer look was taken at plasma and neutral interactions in a ∼1000 km diameter FOV above Svalbard. SuperDARN data were used again in this study, with the addition of spatially resolved neutral wind measurements from an all-sky Fabry-Perot Interferometer known as SCANDI. For an event with excellent data coverage of both instruments, a cross-correlation analysis of plasma and neutral velocities was carried out to extract the lag of the neutral wind to velocity changes in the plasma. Because the event in question had very large, sustained changes of the IMF direction, distinct lags were able to be determined for 61 separate locations within the FOV.

On average, the neutral wind took around 75 minutes to reconfigure after a plasma velocity change. Across the whole FOV however, this varied by up to 30 minutes for the event shown. This shows the importance of mesoscale variability in both the thermosphere and ionosphere, and ultimately is why it is often not useful to strictly define a coupling timescale between the two. As neutral and plasma flows can vary substantially with local time and geomagnetic activity, and are not necessarily well-modelled for non-climatological cases, it is important to take very carefully into account the current states of both when determining any thermospheric reconfiguration time. As shown in Chapter 5, this is because Joule heating rates can drastically change when the strength of ion-neutral coupling varies.

Increased ionisation rates strengthening ion-drag was already alluded to in Chapter 3 when comparing winter and summer time neutral wind contributions to Joule heating. At any time of the year however, sudden and large enhancements of the ion-neutral collision frequency can be induced by ionisation from particle precipitation. Whilst it might be naturally assumed that the increased conductivity this brings will increase Joule heating, the opposite is in fact true when it couples the neutrals tightly to the plasma. Climatological models do not capture this coupling outside of common statistical neutral wind features (such as the dusk cell mentioned earlier), which makes case studies of ion-neutral coupling within short-lived and common auroral features very important. For the event shown in Chapter 5 for instance, Joule heating was almost entirely eliminated upon the onset of poleward moving auroral forms. EISCAT electron density data above Svalbard showed there was indeed enhanced electron densities associated with them, and SCANDI observed neutral winds suddenly accelerating in the direction of the plasma as soon as they began. A novel finding of this study was also the first observations of an IMF B_y transition propagating into the neutral wind during a single observation period, which was only made possible due to a drastically-reduced thermospheric reconfiguration time.

6.1 Future Work

Ion-neutral coupling has been examined on mesoscales, and the reconfiguration time of the thermosphere to ionospheric changes has been shown to be somewhat variable. What has yet to be examined however is thermospheric response times on a global scale. The main barrier to solving this problem however is that there currently is no global coverage of thermospheric neutral wind data available. Several wide-field FPIs similar to SCANDI have been deployed across Alaska (e.g. Conde et al. (2018)) and Antarctica (Greet et al., 1999), whilst more are planned for Scandinavia. Although these do well do expand our understand of thermospheric dynamics by making multipoint observations, the overall coverage is still not much more than a few thousands of square kilometers at F-region altitudes.

A possible solution is to utilise global circulation models (GCMs), such as TIEGCM (Qian et al., 2014). These model the neutral winds physically by inserting parameters into the neutral momentum equation (Eq. 1.30), and then iterating from the previous particle state. The issue here is that the default plasma convection used to determine ion-drag acceleration is typically a statistical climatology, for ease of computation. However, studies have shown that replacing this component of the model with data driven convection patterns from SuperDARN (e.g. Wu et al. (2015)) improves the accuracy of derived winds. Additionally, factors including plasma variability and small scale structure that can't be captured by statistical convection models, but can be measured by SuperDARN, would be represented in the neutral winds this way. By supplementing SuperDARN convection patterns with excellent data coverage into a GCM, thermospheric response times can be potentially be probed for all local times and latitudes that the convection extends to, for many different and varying solar wind driving conditions. As we have seen from the Chapters in this thesis, this could have large consequences for how Joule heating is calculated not only on the small scale, but global scale.

Appendices

A.1 List of SuperDARN Radar Sites

Table A1: Radar sites of the SuperDARN network, along with site codes, geographic and geomagnetic (AACGM) position.

Radar Name/PI Country	Site Code	Geographic Position (GLAT, GLON)	AACGM Position (MLAT, MLON; 2019)
Northern Hemisphere			
Adak Island East, USA	ADE	(51.9,-176.6)	(47.3,-111.1)
Adak Island West, USA	ADW	(51.9,-176.6)	(47.3,-111.1)
Blackstone, USA	BKS	(37.1,-78.0)	(46.4,-0.7)
Christmas Valley East, USA	CVE	(43.3,-120.4)	(48.7,-56.2)
Christmas Valley West, USA	CVW	(43.3,-120.4)	(48.7,-56.2)
Clyde River, Canada	CLY	(70.5,-68.5)	(77.4,18.4)
Fort Hays East, USA	FHE	(38.9,-99.4)	(47.9,-30.1)
Fort Hays West, USA	FHW	(38.9,-99.4)	(47.9,-30.1)
Goose Bay, USA	GBR	(53.3,-60.5)	(59.4,23.8)
Hankasalmi, UK	HAN	(62.3,26.6)	(58.9,103.8)
Hokkaido East, Japan	HOK	(43.5,143.6)	(36.9,-143.2)
Hokkaido West, Japan	HKW	(43.5,143.6)	(36.9,-143.2)
Inuvic, Canada	INV	(68.4,-133.8)	(71.1,-81.1)
Kapuskasing, USA	KAP	(49.4,-82.3)	(58.6,-6.2)
King Salmon, Japan	KSP	(58.7,-156.7)	(57.1,-96.6)
Kodiak, USA	KOD	(57.6,-152.2)	(56.8,-92.3)
Longyearbyen, Norway	LYR	(78.2,16.1)	(75.5,108.5)
Prince George, Canada	PGR	(54.0,-122.6)	(59.0,-61.6)
Pykkvibaer, UK	PYK	(63.8,-20.5)	(63.5,66.0)
Rankin Inlet, Canada	RKN	(62.8,-92.1)	(71.5,-21.7)
Saskatoon, Canada	SAS	(52.2,-106.5)	(60.0,-41.2)
Stokkseyri, UK	STO	(63.9,-21.0)	(63.7,65.7)
Wallops Island, USA	WAL	(37.9,-75.5)	(46.9,2.7)
Southern Hemisphere			
Buckland Park, Australia	BPK	(-34.6,138.5)	(-45.3,-145.2)
Dome C East, Italy	DCE	(-75.1,123.4)	(-89.0,56.9)
Falkland Islands, UK	FIR	(-51.8,-59)	(-39.3,10.2)
Halley, UK	HAL	(-75.5,-26.6)	(-62.2,30.3)
Kerguelen, France	KER	(-49.4,70.3)	(-58.5,124.5)
McMurdo, USA	MCM	(-77.9,166.7)	(-79.9,-32.8)
SANAE, South Africa	SAN	(-71.7,-2.9)	(-61.9,45.1)
South Pole, USA	SPS	(-90.0,118.3)	(-74.3,19.2)
Syowa East, Japan	SYE	(-69.0,39.6)	(-66.5,73.6)
Syowa South, Japan	SYS	(-69.0,39.6)	(-66.5,73.6)
TIGER Bruny Island, Australia	TIG	(-43.4,147.2)	(-54.0,-132.3)
TIGER Unwin, Australia	UNW	(-46.5,168.4)	(-53.8,-105.2)
Zhongshan, China	ZHO	(-69.4,76.4)	(-74.9,99)

Bibliography

Ahn, B.-H., Akasofu, S.-I. and Kamide, Y. (1983), 'The joule heat production rate and the particle energy injection rate as a function of the geomagnetic indices ae and al', *Journal of Geophysical Research: Space Physics* **88**(A8), 6275–6287.

Alfvén, H. (1942), 'Existence of electromagnetic-hydrodynamic waves', *Nature* **150**(3805), 405.

Anderson, C., Davies, T., Conde, M., Dyson, P. and Kosch, M. J. (2011), 'Spatial sampling of the thermospheric vertical wind field at auroral latitudes', *Journal of Geophysical Research: Space Physics* **116**(A6).

Aruliah, A. L., Griffin, E. M., Yiu, H.-C., McWhirter, I. and Charalambous, A. (2010), 'Scandi–an all-sky doppler imager for studies of thermospheric spatial structure.', *Annales Geophysicae (09927689)* **28**(2).

Aruliah, A. L., Müller-Wodarg, I. C. F. and Schoendorf, J. (1999), 'Consequences of geomagnetic history on the high-latitude thermosphere and ionosphere: Averages', *Journal of Geophysical Research: Space Physics* **104**(A12), 28073–28088.

Aruliah, A. L., Rees, D. and Fuller-Rowell, T. J. (1991), 'The combined effect of solar and geomagnetic activity on high latitude thermospheric neutral winds. part i. observations', *Journal of atmospheric and terrestrial physics* **53**(6-7), 467–483.

Atkinson, G. and Hutchison, D. (1978), 'Effect of the day night ionospheric conductivity gradient on polar cap convective flow', *Journal of Geophysical Research: Space Physics* **83**(A2), 725–729.

Babcock, H. D. (1923), 'A study of the green auroral line by the interference method', *The Astrophysical Journal* **57**, 209.

Baker, J. B. H., Zhang, Y., Greenwald, R. A., Paxton, L. J. and Morrison, D. (2004), 'Height-integrated joule and auroral particle heating in the night side high latitude thermosphere', *Geophysical research letters* **31**(9).

Baron, M. J. and Wand, R. H. (1983), 'F region ion temperature enhancements resulting from Joule heating', *Journal of Geophysical Research: Space Physics* **88**(A5), 4114–4118.

Bartels, J., Heck, N. H., and Johnston, H. F. (1939), 'The three-hour-range index measuring geomagnetic activity', *Terrestrial Magnetism and Atmospheric Electricity* **44**(4), 411–454.

Bartels, J. and Veldkamp, J. (1949), 'International data on magnetic disturbances, first quarter, 1949', *Journal of Geophysical Research* **54**(3), 295–299.

Baumjohann, W. and Treumann, R. A. (2012), *Basic space plasma physics*, World Scientific Publishing Company.

Bhardwaj, A. and Raghuram, S. (2012), 'A coupled chemistry-emission model for atomic oxygen green and red-doublet emissions in the comet c/1996 b2 hyakutake', *The Astrophysical Journal* **748**(1), 13.

Bowles, K. L. (1958), 'Observation of vertical-incidence scatter from the ionosphere at 41 mc/sec', *Physical Review Letters* **1**(12), 454.

Brekke, A. (2012), *Physics of the upper polar atmosphere*, Springer Science & Business Media.

Brekke, A. and Moen, J. (1993), 'Observations of high latitude ionospheric conductances', *Journal of Atmospheric and Terrestrial Physics* **55**(11-12), 1493–1512.

Cerisier, J. and Senior, C. (1994), 'Merge: A FORTRAN program (40 pp.)', *Cent. d'Etude des Environ. Terr. et Planet., Cent. Nat. de la Rech Si., StMaur, France.* .

Chapman, S. (1956), 'The electrical conductivity of the ionosphere: A review', *Il Nuovo Cimento (1955-1965)* **4**, 1385–1412.

Chisham, G., Lester, M., Milan, S. E., Freeman, M. P., Bristow, W. A., Grocott, A., McWilliams, K. A., Ruohoniemi, J. M., Yeoman, T. K., Dyson, P. L. et al. (2007), 'A decade of the super dual auroral radar network (SuperDARN): Scientific achievements, new techniques and future directions', *Surveys in geophysics* **28**(1), 33–109.

Chisham, G. and Pinnock, M. (2002), 'Assessing the contamination of superdarn global convection maps by non-f-region backscatter'.

Chisham, G., Yeoman, T. K. and Sofko, G. J. (2008), Mapping ionospheric backscatter measured by the superdarn hf radars–part 1: A new empirical virtual height model, *in* 'Annales Geophysicae', Vol. 26, Copernicus GmbH, pp. 823–841.

Cnossen, I., Wiltberger, M. and Ouellette, J. E. (2012), 'The effects of seasonal and diurnal variations in the earth's magnetic dipole orientation on solar wind–magnetosphere-ionosphere coupling', *Journal of Geophysical Research: Space Physics* **117**(A11).

Cole, K. D. (1962), 'Joule heating of the upper atmosphere', *Australian Journal of Physics* **15**, 223.

Coleman, C. J. (1998), 'A ray tracing formulation and its application to some problems in over-the-horizon radar', *Radio Science* **33**(4), 1187–1197.

Conde, M., Bristow, W., Hampton, D. and Elliott, J. (2018), 'Multi-instrument studies of thermospheric weather above Alaska', *Journal of Geophysical Research: Space Physics* .

Conde, M., Craven, J., Immel, T., Hoch, E., Stenbaek-Nielsen, H., Hallinan, T., Smith, R., Olson, J., Sun, W., Frank, L. A. et al. (2001), 'Assimilated observations of thermospheric winds, the aurora, and ionospheric currents over Alaska', *Journal of Geophysical Research: Space Physics* **106**(A6), 10493–10508.

Conde, M. and Smith, R. W. (1997), 'Phase compensation of a separation scanned, all-sky imaging Fabry–Perot spectrometer for auroral studies', *Applied optics* **36**(22), 5441–5450.

Conde, M. and Smith, R. W. (1998), ‘Spatial structure in the thermospheric horizontal wind above Poker Flat, Alaska, during solar minimum’, *Journal of Geophysical Research: Space Physics* **103**(A5), 9449–9471.

Cousins, E. D. P. and Shepherd, S. G. (2010), ‘A dynamical model of high-latitude convection derived from superdarn plasma drift measurements’, *Journal of Geophysical Research: Space Physics* **115**(A12).

Cowley, S. W. H. and Lockwood, M. (1992), Excitation and decay of solar wind-driven flows in the magnetosphere-ionosphere system, *in* ‘Annales geophysicae’, Vol. 10, pp. 103–115.

de Larquier, S., Ponomarenko, P., Ribeiro, A. J., Ruohoniemi, J. M., Baker, J. B. H., Sterne, K. T. and Lester, M. (2013), ‘On the spatial distribution of decameter–scale subauroral ionospheric irregularities observed by superdarn radars’, *Journal of Geophysical Research: Space Physics* **118**(8), 5244–5254.

Deng, W., Killeen, T. L., Burns, A. G. and Roble, R. G. (1991), ‘The flywheel effect: Ionospheric currents after a geomagnetic storm’, *Geophysical research letters* **18**(10), 1845–1848.

Deng, W., Killeen, T. L., Burns, A. G., Roble, R. G., Slavin, J. A. and Wharton, L. E. (1993), ‘The effects of neutral inertia on ionospheric currents in the high-latitude thermosphere following a geomagnetic storm’, *Journal of Geophysical Research: Space Physics* **98**(A5), 7775–7790.

Deng, Y. and Ridley, A. J. (2007), ‘Possible reasons for underestimating joule heating in global models: E field variability, spatial resolution, and vertical velocity’, *Journal of Geophysical Research: Space Physics* **112**(A9).

Dessler, A. J. and Fejer, J. A. (1963), ‘Interpretation of Kp index and M-region geomagnetic storms’, *Planetary and Space Science* **11**(5), 505–511.

Dhadly, M. and Conde, M. (2017), ‘Trajectories of thermospheric air parcels flowing over alaska, reconstructed from ground-based wind measurements’, *Journal of Geophysical Research: Space Physics* **122**(6), 6635–6651.

Dhadly, M. S., Emmert, J. T., Drob, D. P., Conde, M. G., Doornbos, E., Shepherd, G. G., Makela, J. J., Wu, Q., Nieciejewski, R. J. and Ridley, A. J. (2018), 'Seasonal dependence of geomagnetic active-time northern high-latitude upper thermospheric winds', *Journal of Geophysical Research: Space Physics* **123**(1), 739–754.

Drob, D. P., Emmert, J. T., Meriwether, J. W., Makela, J. J., Doornbos, E., Conde, M., Hernandez, G., Noto, J., Zawdie, K. A., McDonald, S. E. et al. (2015), 'An update to the horizontal wind model (HWM): The quiet time thermosphere', *Earth and Space Science* **2**(7), 301–319.

Dungey, J. W. (1961), 'Interplanetary magnetic field and the auroral zones', *Physical Review Letters* **6**(2), 47.

Emmert, J. T., Drob, D. P., Shepherd, G. G., Hernandez, G., Jarvis, M. J., Meriwether, J. W., Niciejewski, R. J., Sipler, D. P. and Tepley, C. A. (2008), 'Dwm07 global empirical model of upper thermospheric storm-induced disturbance winds', *Journal of Geophysical Research: Space Physics* **113**(A11).

Fasel, G. J., Minow, J. I., Lee, L. C., Smith, R. W. and Deehr, C. S. (1994), Poleward-moving auroral forms: What do we really know about them?, *in* 'Physical signatures of magnetospheric boundary layer processes', Springer, pp. 211–226.

Fear, R. C., Trenchi, L., Coxon, J. C. and Milan, S. E. (2017), 'How much flux does a flux transfer event transfer?', *Journal of Geophysical Research: Space Physics* **122**(12), 12–310.

Ferdousi, B., Nishimura, Y., Maruyama, N. and Lyons, L. R. (2019), 'Subauroral neutral wind driving and its feedback to saps during the 17 march 2013 geomagnetic storm', *Journal of Geophysical Research: Space Physics* **124**(3), 2323–2337.

Forster, M., Rentz, S., Kohler, W., Liu, H. and Haaland, S. E. (2008), Imf dependence of high-latitude thermospheric wind pattern derived from CHAMP crass-track measurements, *in* 'Annales geophysicae: atmospheres, hydrospheres and space sciences', Vol. 26, p. 1581.

Foster, J. C., St-Maurice, J.-P. and Abreu, V. J. (1983), 'Joule heating at high latitudes', *Journal of Geophysical Research: Space Physics* **88**(A6), 4885–4897.

Fuller-Rowell, T. J. and Rees, D. (1980), 'A three-dimensional time-dependent global model of the thermosphere', *Journal of the Atmospheric Sciences* **37**(11), 2545–2567.

Fuselier, S. A., Mende, S. B., Moore, T. E., Frey, H. U., Petrinec, S. M., Claflin, E. S. and Collier, M. R. (2003), Cusp dynamics and ionospheric outflow, *in* 'Magnetospheric ImagingThe Image Prime Mission', Springer, pp. 285–312.

Gordon, W. E. (1958), 'Incoherent scattering of radio waves by free electrons with applications to space exploration by radar', *Proceedings of the IRE* **46**(11), 1824–1829.

Greenwald, R. A., Baker, K. B., Dudeney, J. R., Pinnock, M., Jones, T. B., Thomas, E. C., Villain, J.-P., Cerisier, J.-C., Senior, C., Hanuise, C. et al. (1995a), 'Darn/superdarn', *Space Science Reviews* **71**(1-4), 761–796.

Greenwald, R. A., Bristow, W. A., Sofko, G. J., Senior, C., Cerisier, J.-C. and Szabo, A. (1995b), 'Super dual auroral radar network radar imaging of dayside high-latitude convection under northward interplanetary magnetic field: Toward resolving the distorted two-cell versus multicell controversy', *Journal of Geophysical Research: Space Physics* **100**(A10), 19661–19674.

Greet, P. A., Conde, M. G., Dyson, P. L., Innis, J. L., Breed, A. M. and Murphy, D. J. (1999), 'Thermospheric wind field over mawson and davis, antarctica; simultaneous observations by two fabry–perot spectrometers of λ630 nm emission', *Journal of Atmospheric and Solar-Terrestrial Physics* **61**(14), 1025–1045.

Grocott, A., Milan, S. E., Imber, S. M., Lester, M. and Yeoman, T. K. (2012), 'A quantitative deconstruction of the morphology of high-latitude ionospheric convection', *Journal of Geophysical Research: Space Physics* **117**(A5).

Grydeland, T., Strømme, A., van Eyken, T. and La Hoz, C. (2004), 'The capabilities of the EISCAT svalbard radar for inter-hemispheric coordinated studies', *arXiv preprint physics/0404098* .

Hagfors, T. and Evans, J. V. (1968), *Radar Astronomy*, Mcgraw-Hill.

Han, D.-S., Hietala, H., Chen, X.-C., Nishimura, Y., Lyons, L. R., Liu, J.-J., Hu, H.-Q. and Yang, H.-G. (2017), 'Observational properties of dayside throat aurora and implications on the possible generation mechanisms', *Journal of Geophysical Research: Space Physics* **122**(2), 1853–1870.

Hanuise, C., Villain, J. P., Gresillon, D., Cabrit, B., Greenwald, R. A. and Baker, K. B. (1993), Interpretation of hf radar ionospheric Doppler spectra by collective wave scattering theory, *in* 'Annales Geophysicae', Vol. 11, pp. 29–39.

Hardy, D. A., Gussenhoven, M. S., Raistrick, R. and McNeil, W. J. (1987), 'Statistical and functional representations of the pattern of auroral energy flux, number flux, and conductivity', *Journal of Geophysical Research: Space Physics* **92**(A11), 12275–12294.

Hays, P. B. and Roble, R. G. (1971), 'Direct observations of thermospheric winds during geomagnetic storms', *Journal of Geophysical Research* **76**(22), 5316–5321.

Heelis, R. A. and Coley, W. R. (1988), 'Global and local Joule heating effects seen by DE 2', *Journal of Geophysical Research: Space Physics* **93**(A7), 7551–7557.

Heelis, R. A., Lowell, J. K. and Spiro, R. W. (1982), 'A model of the high-latitude ionospheric convection pattern', *Journal of Geophysical Research: Space Physics* **87**(A8), 6339–6345.

Heelis, R. A., McEwen, D. and Guo, W. (2002), 'Ion and neutral motions observed in the winter polar upper atmosphere', *Journal of Geophysical Research: Space Physics* **107**(A12).

Heppner, J. P. and Maynard, N. C. (1987), 'Empirical high-latitude electric field models', *Journal of Geophysical Research: Space Physics* **92**(A5), 4467–4489.

Hinteregger, H. E., Hall, L. A. and Schmidtke, G. (1965), Solar XUV radiation and neutral particle distribution in july 1963 themosphere, *in* 'Space Research Conference', p. 1175.

Hosokawa, K. and Ogawa, Y. (2010), 'Pedersen current carried by electrons in auroral d-region', *Geophysical Research Letters* **37**(18).

Huang, Y., Richmond, A. D., Deng, Y. and Roble, R. (2012), 'Height distribution of joule heating and its influence on the thermosphere', *Journal of Geophysical Research: Space Physics* **117**(A8).

Jacchia, L. G. (1965), 'New static models of the thermosphere and exosphere with empirical temperature profiles', *SAO special report* **313**.

Joshi, P. P., H. Baker, J. B., Ruohoniemi, J. M., Makela, J. J., Fisher, D. J., Harding, B. J., Frissell, N. A. and Thomas, E. G. (2015), 'Observations of storm time midlatitude ion-neutral coupling using SuperDARN radars and nation Fabry-Perot interferometers', *Journal of Geophysical Research: Space Physics* **120**(10), 8989–9003.

Juvells, I., Carnicer, A., Ferré-Borrull, J., Martín-Badosa, E. and Montes-Usategui, M. (2006), 'Understanding the concept of resolving power in the Fabry–Perot interferometer using a digital simulation', *European journal of physics* **27**(5), 1111.

Killeen, T. L., Craven, J. D., Frank, L. A., Ponthieu, J.-J., Spencer, N. W., Heelis, R. A., Brace, L. H., Roble, R. G., Hays, P. B. and Carignan, G. R. (1988), 'On the relationship between dynamics of the polar thermosphere and morphology of the aurora: Global-scale observations from dynamics explorers 1 and 2', *Journal of Geophysical Research: Space Physics* **93**(A4), 2675–2692.

Killeen, T. L., Hays, P. B., Carignan, G. R., Heelis, R. A., Hanson, W. B., Spencer, N. W. and Brace, L. H. (1984), 'Ion-neutral coupling in the high-latitude f region: Evaluation of ion heating terms from dynamics explorer 2', *Journal of Geophysical Research: Space Physics* **89**(A9), 7495–7508.

Killeen, T. L., Won, Y.-I., Niciejewski, R. J. and Burns, A. G. (1995), 'Upper thermosphere winds and temperatures in the geomagnetic polar cap: Solar cycle, geomagnetic activity, and interplanetary magnetic field dependencies', *Journal of Geophysical Research: Space Physics* **100**(A11), 21327–21342.

Kohl, H. and King, J. W. (1967), 'Atmospheric winds between 100 and 700 km and their effects on the ionosphere', *Journal of Atmospheric and Terrestrial Physics* **29**(9), 1045–1062.

Kosch, M. J., Cierpka, K., Rietveld, M. T., Hagfors, T. and Schlegel, K. (2001), 'High-latitude ground-based observations of the thermospheric ion-drag time constant', *Geophysical research letters* **28**(7), 1395–1398.

Kosch, M. J., Hagfors, T. and Schlegel, K. (1998), Extrapolating EISCAT Pedersen conductances to other parts of the sky using ground-based TV auroral images, *in* 'Annales Geophysicae', Vol. 16, Springer, pp. 583–588.

Kubota, M., Fukunishi, H. and Okano, S. (2001), 'Characteristics of medium-and large-scale TIDs over japan derived from oi 630-nm nightglow observation', *Earth, planets and space* **53**(7), 741–751.

Lam, M. M., Freeman, M. P., Jackman, C. M., Rae, I. J., Kalmoni, N. M. E., Sandhu, J. K. and Forsyth, C. (2019), 'How well can we estimate pedersen conductance from the themis white-light all-sky cameras?', *Journal of Geophysical Research: Space Physics* **124**(4), 2920–2934.

Landau, L. D. (1946), 'On the vibrations of the electronic plasma', *Zh. Eksp. Teor. Fiz.* **10**, 25.

Lu, G., Richmond, A. D., Emery, B. A. and Roble, R. G. (1995), 'Magnetosphere-ionosphere-thermosphere coupling: Effect of neutral winds on energy transfer and field-aligned current', *Journal of Geophysical Research: Space Physics* **100**(A10), 19643–19659.

Lyons, L. R., Killeen, T. L. and Walterscheid, R. L. (1985), 'The neutral wind flywheel as a source of quiet-time, polar-cap currents', *Geophysical research letters* **12**(2), 101–104.

Maslin, N. M. (2017), *HF communications: a systems approach*, CRC Press.

Matsuo, T., Richmond, A. D. and Hensel, K. (2003), 'High-latitude ionospheric electric field variability and electric potential derived from de-2 plasma drift measurements: Dependence on imf and dipole tilt', *Journal of Geophysical Research: Space Physics* **108**(A1).

McCormac, F. G., Killeen, T. L. and Thayer, J. P. (1991), 'The influence of imf by on the high-latitude thermospheric circulation during northward imf', *Journal of Geophysical Research: Space Physics* **96**(A1), 115–128.

McHarg, M., Chun, F., Knipp, D., Lu, G., Emery, B. and Ridley, A. (2005), 'High-latitude joule heating response to imf inputs', *Journal of Geophysical Research: Space Physics* **110**(A8).

McWilliams, K. A., Yeoman, T. K. and Provan, G. (2000), A statistical survey of dayside pulsed ionospheric flows as seen by the CUTLASS Finland HF radar, *in* 'Annales Geophysicae', Vol. 18, Springer, pp. 445–453.

Milan, S. E., Lester, M., Cowley, S. W. H., Oksavik, K., Brittnacher, M., Greenwald, R. A., Sofko, G. and Villain, J.-P. (2003), Variations in the polar cap area during two substorm cycles, *in* 'Annales Geophysicae', Vol. 21, pp. 1121–1140.

Milan, S. E., Lester, M., Greenwald, R. A. and Sofko, G. (1999), The ionospheric signature of transient dayside reconnection and the associated pulsed convection return flow, *in* 'Annales Geophysicae', Vol. 17, Springer, pp. 1166–1171.

Milan, S. E., Yeoman, T. K., Lester, M., Thomas, E. C. and Jones, T. B. (1997), Initial backscatter occurrence statistics from the cutlass hf radars, *in* 'Annales Geophysicae', Vol. 15, Springer, pp. 703–718.

Murr, D. L. and Hughes, W. J. (2001), 'Reconfiguration timescales of ionospheric convection', *Geophysical research letters* **28**(11), 2145–2148.

Nishitani, N., Ruohoniemi, J. M., Lester, M., Baker, J. B. H., Koustov, A. V., Shepherd, S. G., Chisham, G., Hori, T., Thomas, E. G., Makarevich, R. A. et al. (2019), 'Review of the accomplishments of mid-latitude super dual auroral radar network (SuperDARN) hf radars', *Progress in Earth and Planetary Science* **6**(1), 27.

Nozawa, S. and Brekke, A. (1995), 'Studies of the E region neutral wind in the disturbed auroral ionosphere', *Journal of Geophysical Research: Space Physics* **100**(A8), 14717–14734.

Ossakow, S. L. and Chaturvedi, P. K. (1979), 'Current convective instability in the diffuse aurora', *Geophysical Research Letters* **6**(4), 332–334.

Oyama, S.-i., Watanabe, T., Fujii, R., Nozawa, S., Tsuda, T. T. et al. (2013), 'Layered conductance in the ionosphere estimated using data from a multiwavelength photometer at the European Incoherent Scatter radar site', *Antarctic Record* **57**(3), 339–356.

Pettigrew, E. D., Shepherd, S. G. and Ruohoniemi, J. M. (2010), 'Climatological patterns of high-latitude convection in the northern and southern hemispheres: Dipole tilt dependencies and interhemispheric comparisons', *Journal of Geophysical Research: Space Physics* **115**(A7).

Picone, J. M., Hedin, A. E., Drob, D. P. and Aikin, A. C. (2002), 'Nrlmsise-00 empirical model of the atmosphere: Statistical comparisons and scientific issues', *Journal of Geophysical Research: Space Physics* **107**(A12), SIA–15.

Ponomarenko, P. V., St-Maurice, J. P., Waters, C. L., Gillies, R. G. and Koustov, A. V. (2009), Refractive index effects on the scatter volume location and doppler velocity estimates of ionospheric hf backscatter echoes, *in* 'Annales geophysicae: atmospheres, hydrospheres and space sciences', Vol. 27, p. 4207.

Provan, G., Yeoman, T. K., Lester, M. and Milan, S. E. (2002b), A multi-instrument approach to mapping the global dayside merging rate, *in* 'Annales Geophysicae', Vol. 20, pp. 1905–1920.

Provan, G., Yeoman, T. K., Milan, S. E., Ruohoniemi, J. M. and Barnes, R. (2002), An assessment of the" map-potential" and" beam-swinging" techniques for measuring the ionospheric convection pattern using data from the SuperDARN radars, *in* 'Annales Geophysicae', Vol. 20, pp. 191–202.

Qian, L., Burns, A. G., Emery, B. A., Foster, B., Lu, G., Maute, A., Richmond, A. D., Roble, R. G., Solomon, S. C. and Wang, W. (2014), 'The ncar tie-gcm: A community model of the coupled thermosphere/ionosphere system', *Modeling the ionosphere-thermosphere system* **201**, 73–83.

Rash, J. P. S., Rodger, A. S. and Pinnock, M. (1999), 'HF radar observations of the high-latitude ionospheric convection pattern in the morning sector for northward IMF and motion of the convection reversal boundary', *Journal of Geophysical Research: Space Physics* **104**(A7), 14847–14866.

Ribeiro, A. J., Ruohoniemi, J. M., Ponomarenko, P. V., N. Clausen, L. B., H. Baker, J. B., Greenwald, R., Oksavik, K. and de Larquier, S. (2013), ‘A comparison of superdarn acf fitting methods’, *Radio Science* **48**(3), 274–282.

Rich, F. J., Gussenhoven, M. S. and Greenspan, M. E. (1987), Using simultaneous particle and field observations on a low altitude satellite to estimate Joule heat energy flow into the high latitude ionosphere, *in* ‘Annales Geophysicae’, Vol. 5, pp. 527–534.

Rishbeth, H. and Williams, P. J. S. (1985), ‘The eiscat ionospheric radar-the system and its early results’, *Quarterly Journal of the Royal Astronomical Society* **26**, 478–512.

Roble, R. G. and Matsushita, S. (1975), ‘An estimate of the global-scale joule heating rates in the thermosphere due to time mean currents’, *Radio Science* **10**(3), 389–399.

Ronksley, A. (2016), Optical remote sensing of mesoscale thermospheric dynamics above Svalbard and Kiruna, PhD thesis, UCL (University College London).

Ruohoniemi, J. M. and Baker, K. B. (1998), ‘Large-scale imaging of high-latitude convection with super dual auroral radar network HF radar observations’, *Journal of Geophysical Research: Space Physics* **103**(A9), 20797–20811.

Ruohoniemi, J. M. and Greenwald, R. A. (1996), ‘Statistical patterns of high-latitude convection obtained from goose bay HF radar observations’, *Journal of Geophysical Research: Space Physics* **101**(A10), 21743–21763.

Ruohoniemi, J. M. and Greenwald, R. A. (2005), ‘Dependencies of high-latitude plasma convection: Consideration of interplanetary magnetic field, seasonal, and universal time factors in statistical patterns’, *Journal of Geophysical Research: Space Physics* **110**(A9).

Shepherd, S. G. (2014), ‘Altitude-adjusted corrected geomagnetic coordinates: Definition and functional approximations’, *Journal of Geophysical Research: Space Physics* **119**(9), 7501–7521.

Shepherd, S. G. (2017), ‘Elevation angle determination for superdarn hf radar layouts’, *Radio Science* **52**(8), 938–950.

Shepherd, S. G. and Ruohoniemi, J. M. (2000), ‘Electrostatic potential patterns in the high-latitude ionosphere constrained by SuperDARN measurements’, *Journal of Geophysical Research: Space Physics* **105**(A10), 23005–23014.

Smith, R. W., Rees, D. and Stewart, R. D. (1988), ‘Southern hemisphere thermospheric dynamics: A review’, *Reviews of Geophysics* **26**(3), 591–622.

Spencer, N. W., Wharton, L. E., Carignan, G. R. and Maurer, J. C. (1982), ‘Thermosphere zonal winds, vertical motions and temperature as measured from Dynamics Explorer’, *Geophysical Research Letters* **9**(9), 953–956.

SuperDARN Data Analysis Working Group. Thomas, E. G., Ponomarenko, P. V., Billett, D. D., Bland, E. C., Burrell, A. G., Kotyk, K., Reimer, A. S., Schmidt, M., Shepherd, S. G., Sterne, K. T. and Walach, M.-T. (2018), ‘Superdarn radar software toolkit (rst) 4.2’.
URL: *https://doi.org/10.5281/zenodo.1403226*

Taguchi, S., Hosokawa, K., Ogawa, Y., Aoki, T. and Taguchi, M. (2012), ‘Double bursts inside a poleward-moving auroral form in the cusp’, *Journal of Geophysical Research: Space Physics* **117**(A12).

Thayer, J. P., Vickrey, J. F., Heelis, R. A. and Gary, J. B. (1995), ‘Interpretation and modeling of the high-latitude electromagnetic energy flux’, *Journal of Geophysical Research: Space Physics* **100**(A10), 19715–19728.

Thébault, E., Finlay, C. C., Beggan, C. D., Alken, P., Aubert, J., Barrois, O., Bertrand, F., Bondar, T., Boness, A., Brocco, L. et al. (2015), ‘International geomagnetic reference field: the 12th generation’, *Earth, Planets and Space* **67**(1), 79.

Thomas, E. G. and Shepherd, S. G. (2018), ‘Statistical patterns of ionospheric convection derived from mid-latitude, high-latitude, and polar superdarn hf radar observations’, *Journal of Geophysical Research: Space Physics* **123**(4), 3196–3216.

Titheridge, J. E. (1995), ‘Winds in the ionospherea review’, *Journal of Atmospheric and Terrestrial Physics* **57**(14), 1681–1714.

Tsuda, T., Nozawa, S., Oyama, S., Motoba, T., Ogawa, Y., Shinagawa, H., Nishitani, N., Hosokawa, K., Sato, N., Lester, M. et al. (2009), 'Acceleration mechanism of high-speed neutral wind observed in the polar lower thermosphere', *Journal of Geophysical Research: Space Physics* **114**(A4).

Vickrey, J. F., Vondrak, R. R. and Matthews, S. J. (1981), 'The diurnal and latitudinal variation of auroral zone ionospheric conductivity', *Journal of Geophysical Research: Space Physics* **86**(A1), 65–75.

Wallis, D. D. and Budzinski, E. E. (1981), 'Empirical models of height integrated conductivities', *Journal of Geophysical Research: Space Physics* **86**(A1), 125–137.

Wannberg, G., Wolf, I., Vanhainen, L.-G., Koskenniemi, K., Röttger, J., Postila, M., Markkanen, J., Jacobsen, R., Stenberg, A., Larsen, R. et al. (1997), 'The eiscat svalbard radar: A case study in modern incoherent scatter radar system design', *Radio Science* **32**(6), 2283–2307.

Weimer, D. R. (1995), 'Models of high-latitude electric potentials derived with a least error fit of spherical harmonic coefficients', *Journal of Geophysical Research: Space Physics* **100**(A10), 19595–19607.

Wu, Q., Emery, B. A., Shepherd, S. G., Ruohoniemi, J. M., Frissell, N. A. and Semeter, J. (2015), 'High-latitude thermospheric wind observations and simulations with superdarn data driven ncar tiegcm during the december 2006 magnetic storm', *Journal of Geophysical Research: Space Physics* **120**(7), 6021–6028.

Xing, Z. Y., Yang, H. G., Han, D. S., Wu, Z. S., Hu, Z. J., Zhang, Q. H., Kamide, Y., Hu, H. Q., Zhang, B. C., Liu, J. M. et al. (2012), 'Poleward moving auroral forms (pmafs) observed at the yellow river station: A statistical study of its dependence on the solar wind conditions', *Journal of Atmospheric and Solar-Terrestrial Physics* **86**, 25–33.

Zhang, X. X., Wang, C., Chen, T., Wang, Y. L., Tan, A., Wu, T. S., Germany, G. A. and Wang, W. (2005), 'Global patterns of Joule heating in the high-latitude ionosphere', *Journal of Geophysical Research: Space Physics* **110**(A12).

Zou, Y., Nishimura, Y., Lyons, L., Conde, M., Varney, R., Angelopoulos, V. and Mende, S. (2018), 'Mesoscale F region neutral winds associated with quasi-steady and transient nightside auroral forms', *Journal of Geophysical Research: Space Physics* .